5-1-2012

A Statistical phonon transport model for thermal transport in cyrstalline materials from the diffuse to ballistic regime

Thomas III Brown

A STATISTICAL PHONON TRANSPORT MODEL FOR THERMAL TRANSPORT IN CRYSTALLINE MATERIALS FROM THE DIFFUSE TO BALLISTIC REGIME

by

Thomas W. Brown III

B.S. Mechanical Engineering, Rochester Institute of Technology, 2002

M.S. Mechanical Engineering, Rochester Institute of Technology, 2002

A DISSERTATION

Submitted in partial fulfillment of the requirements

For the degree of Doctor of Philosophy

in

Microsystems Engineering

at the

Rochester Institute of Technology

May 2012

Author: _____

Microsystems Engineering Program

Certified by: _____

Edward C. Hensel, Ph.D.
Professor and Department Head of Mechanical Engineering Program

Approved by: _____

Bruce W. Smith, Ph.D.
Director of Microsystems Engineering Program

Certified by: _____

Harvey J. Palmer, Ph.D.
Dean, Kate Gleason College of Engineering

ROCHESTER INSTITUTE OF TECHNOLOGY
ROCHESTER, NEW YORK

CERTIFICATE OF APPROVAL

Ph.D. DEGREE DISSERTATION

The Ph.D. Degree Dissertation of Thomas W. Brown III
has been examined and approved by the
dissertation committee as satisfactory for the
dissertation required for the
Ph.D. degree in Microsystems Engineering

_____
Dr. Edward C. Hensel, Dissertation Advisor

_____
Dr. Satish G. Kandlikar

_____
Dr. Santosh K. Kurinec

_____
Dr. Robert J. Stevens

_____
Date

DISSERTATION RELEASE PERMISSION
ROCHESTER INSTITUTE OF TECHNOLOGY

Title of Dissertation:

A STATISTICAL PHONON TRANSPORT MODEL FOR THERMAL TRANSPORT IN CRYSTALLINE MATERIALS FROM THE DIFFUSE TO BALLISTIC REGIME

I, Thomas W. Brown III, hereby grant permission to Wallace Memorial Library of R.I.T. to reproduce my thesis in whole or in part. Any reproduction will not be for commercial use or profit.

Signature _____

Date

A STATISTICAL PHONON TRANSPORT MODEL FOR THERMAL TRANSPORT IN CRYSTALLINE MATERIALS FROM THE DIFFUSE TO BALLISTIC REGIME

by

Thomas W. Brown III

Submitted to the
Kate Gleason College of Engineering
in partial fulfillment of the requirements
for the Doctor of Philosophy Degree
at the Rochester Institute of Technology

Abstract

Phonon transport in micro- nanoscale crystalline materials can be well modeled by the Boltzmann transport equation (BTE). The complexities associated with solving the BTE have led to the development of various numerical models to simulate phonon transport. These models have been applied to predict thermal transport from the diffuse to ballistic regime. While some success using techniques such as the Monte Carlo method has been achieved, there are still a significant number of approximations related to the intricacies of phonon transport that must be more accurately modeled for better predictions of thermal transport at reduced length scales.

The objective of the present work is to introduce a Statistical Phonon Transport (SPT) model for simulating thermal transport in crystalline materials from the diffuse to ballistic regime. The SPT model provides a theoretically more realistic treatment of phonon transport physics by eliminating some of the common approximations utilized by other numerical modeling techniques. The SPT model employs full anisotropic dispersion. Phonon populations are modeled without the use of scaling factors or pseudo-random number generation. Three-phonon scattering is rigorously enforced following the selection rules of energy and pseudo-momentum. The SPT model provides a flexible framework for incorporating various phonon scattering mechanisms and models.

Results related to the determination of allowable three-phonon interactions are presented along with several three-phonon scattering models. Steady-state and transient thermal transport results for silicon from the diffuse to ballistic regimes are presented and compared to analytical and experimental results. Recommendations for future work related to increasing the robustness of the SPT model as well as utilizing the SPT model to predict thermal transport in practical applications are given.

To Ma, Dad, Nun, and Papa

Acknowledgements

I would like to express my sincere gratitude to my Ph.D. advisor Dr. Edward C. Hensel for his guidance and support throughout my Ph.D. studies. His creative ideas and advice played an integral role in my academic achievement. I have very much enjoyed the experience of working with him over the years.

I would also like to thank my research committee members, Dr. Stevens, Dr. Kandlikar, Dr. Kurinec. They have provided valuable suggestions pertaining to my research.

I would like to thank Dr. Abushagur and Dr. Smith for their guidance during my time in the Microsystems Engineering program.

Special thanks to Dr. Ghoneim for being a mentor and sharing his knowledge on teaching engineering students.

I would like to thank Sean Strout for the helpful conversations in C++ programming.

I would like to thank my colleague Brian Moses for the many conversations discussing solid state physics and the help on my research.

Many thanks to the Mechanical Engineering staff: Diane Selleck, Diedra Livingston, and Bill Finch for helping me over the years. Also, thanks to Emilio Del Plato for helping with various computer issues.

Thank you very much to Yu-Chin Allen and Dr. Ahmet Becene for their support over the years.

Special thanks to Dr. Beatriz Bezerra for her sincere help and support during this endeavor.

Thanks to my family and friends for supporting me over the years.

Finally, I would like to thank my parents and grandparents for instilling in me the importance of education and giving me the loving support to achieve this great accomplishment.

Table of Contents

Page

List of Figures

Figure Page

Nomenclature

$\bar{t}$	mean lifetime	s
$\hbar$	reduced Planck's constant, $h/2\pi$	$1.05459\text{x}10^{-34}$J s
$\mathbf{a}$	primitive translation vector	m
$\mathbf{b}$	reciprocal lattice vector	m^{-1}
$\mathbf{F}$	force vector	N
$\mathbf{G}$	reciprocal lattice vector	m^{-1}
$\mathbf{K}$	phonon wave vector	m^{-1}
$\mathbf{p}$	momentum	J s/m
$\mathbf{r}$	position vector	m
$\mathbf{u}$	atomic position vector	m
$\widetilde{T}$	kinetic energy	J
$\widetilde{U}$	energy	J
$\widetilde{V}$	potential energy	J
a	lattice constant	m
C	total number of spatial cells	

c	spatial cell	
D	Dynamical matrix	
D	density of state	s/rad m^3
f	distribution function	
h	Planck's constant	$6.626x10^{-34}$J s
k	thermal conductivity	W/m K
k_B	Boltzmann constant	$1.38062x10^{-23}$J/K
M	mass	kg
M	total number of pseudo-states	
m	pseudo-state	
N	number of phonons	
n	phonon excitation number	
P	probability	
p	polarization	
q	heat flux	W/m^2
T	temperature	K
t	time	s
V	Volume	m^3

Acronyms

BTE	Boltzmann transport equation
BZ	Brillouin zone
CDF	cumulative distribution function
DSV	drift state vector
FCC	face-centered cubic

LA	longitudinal acoustic	
LO	longitudinal optic	
LSV	Local State Vector	
MC	Monte Carlo	
MD	Molecular Dynamics	
SPT	Statistical Phonon Transport	
TA	transverse acoustic	
TO	transverse optic	

Greek Symbols

α	force constant	
Δt	time step	s
δ	Kronecker-delta function	
Ω	volume of Wigner-Seitz cell	m^3
ω	angular frequency	rad/s
ℓ	minimum cell length	m
τ	time step index	
$\boldsymbol{v}$	velocity	m/s

Subscripts

A	atomic
a	angular
c	central
$\mathbf{K}$	phonon wave vector
α	cartesian direction
β	cartesian direction

p	polarization
ε	error acceptance criteria

CHAPTER 1

Introduction to Multiscale Thermal Transport

The objective of this work is to provide a numerical model for the simulation of thermal transport in crystalline materials from the diffuse to ballistic regime. The work will begin with an introduction to each of these topics.

1.1 Thermal Energy Carriers in Solid Crystals

Before a discussion related to thermal transport in crystalline materials at micro- and nanoscales can occur it is first necessary to define the dominant thermal energy carriers. In semiconductors heat is conducted through the motion of atoms about their equilibrium positions. The motion of each atom is influenced by neighboring atoms through the interatomic potential. Figure 1.1 shows a typical interatomic potential profile where the interaction force is equivalent to the derivative of the potential.

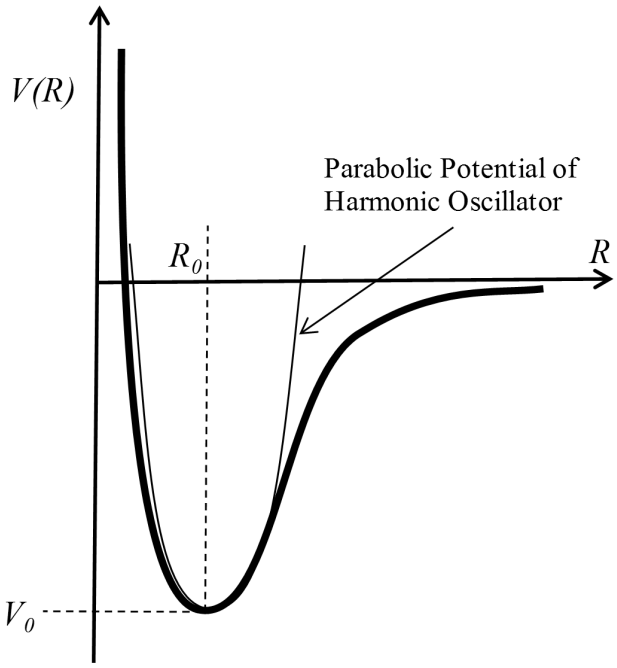

Figure 1.1 A typical interatomic potential profile (thick line) along with a parabolic potential of an harmonic oscillator (thin line).

An ideal crystal is an infinite periodic array of atoms arranged in a lattice. Consider the atoms and interatomic interactions to be represented by masses connected with springs, as depicted in Fig. 1.2.

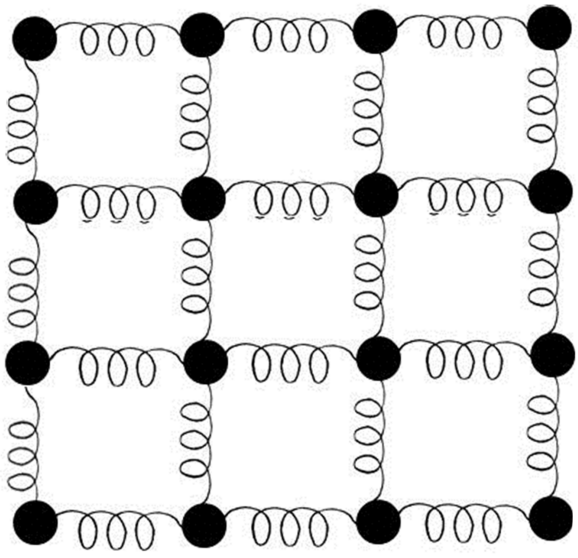

Figure 1.2 A mass-spring system representing interconnected atoms in a crystal.

In the harmonic approximation the interatomic forces are proportional to the atomic displacements, thus the springs depicted in Fig. 1.2 are linear. Although, in real crystals, as shown in Fig. 1.1, the interatomic forces are nonlinear. This nonlinearity (anharmonicity) leads to interactions between lattice waves as will be discussed in Chapter 3 § 3.15. If a mass from Fig. 1.2 was oscillating at a particular frequency, ω, it would be possible for the vibration to propagate throughout the entire mass-spring system in the form of a wave. Similarly, in a crystal the motion of atoms about their equilibrium positions can be represented by a superposition of the various lattice waves. These lattice vibrations have energy equivalent to $\hbar\omega$, where $\hbar$ is Planck's constant divided by 2π. The energy quanta of lattice vibrations are known as a phonon.

Phonons have both wave and particle characteristics. If coherence effects can be ignored, phonons can be considered as individual particles without considering phase information [1]. Therefore, the mass-spring system shown in Fig. 1.2 can be replaced by phonon particles in a box. Analogous to waves travelling and interacting with one another, each phonon particle in the box can drift and interact with other particles.

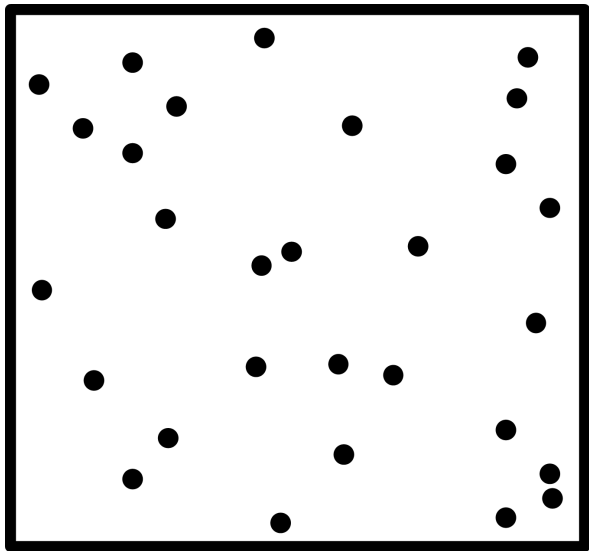

Figure 1.3 A phonon gas model replacing the mass-spring system in Fig. 1.2.

These phonon particles can interact with impurities, grain boundaries, and geometric boundaries. Additionally, they can interact with other phonon particles. It is these phonon particle interactions that govern thermal conduction in semiconductors.

1.2 Macroscale Thermal Conduction

It is well known that Fourier's law

$$q = -k\nabla T \quad , \tag{1.1}$$

accurately models heat conduction at the macroscale, where q is the heat flux, k is the thermal conductivity, and ∇T is the temperature gradient. Thermal conduction can be defined as the energy transfer process through a medium, caused by a temperature difference due to the random motion of heat carriers [1]. These heat carriers include electrons, phonons, photons, and molecules. Fourier's law assumes the material to be in local thermodynamic equilibrium. When material characteristic length scales become comparable to the mean free path of the heat carriers or when time scales are comparable to the relaxation times of the heat carriers Fourier's law becomes invalid since local thermodynamic equilibrium is not guaranteed [2]. Therefore, when considering thermal transport at micro- and nanoscales it becomes necessary to consider the individual heat carriers and their various scattering mechanisms.

1.3 Micro- Nanoscale Thermal Transport Modeling Techniques

1.3.1 Boltzmann Transport Equation. The general form of the Boltzmann transport equation (BTE)is

$$\frac{\partial f}{\partial t} + \boldsymbol{\upsilon} \cdot \nabla f + \mathbf{F}\frac{\partial f}{\partial \mathbf{p}} = \left(\frac{\partial f}{\partial t}\right)_{scattering} \quad , \tag{1.2}$$

where $\mathbf{F}$ is the force applied to the particles and $\boldsymbol{\upsilon}$ is the velocity. The statistical distribution function, f, represents an ensemble of particles that varies with time t, particle position vector $\mathbf{r}$, and momomentum vector $\mathbf{p}$ [2, 3]. The BTE can be applied

to problems involving gas molecules, electrons, phonons, and photons. It can be used to simulate heat conduction processes from nanoscale to macroscale in the classical size effect regime. The BTE can describe both equilibrium and non-equilibrium phenomena which makes it well suited for describing phonon transport. The left hand side of Eq. (1.2) represents the drift term of the particle ensemble away from equilibrium. The right hand side of Eq. (1.2) is the scattering term that restores the particle ensemble to equilibrium. The distribution function f is a function of several variables, making it difficult to solve deterministically. Typically, a relaxation time approximation is invoked to simplify the scattering term which allows the BTE to be solved. This form of the BTE is given as

$$\frac{df}{dt} + \upsilon \cdot \nabla f + \mathbf{F}\frac{\partial f}{\partial \mathbf{p}} = \frac{f_0 - f}{\tau(\mathbf{r}, \mathbf{p})} \quad , \tag{1.3}$$

where f_0 is the equilibrium distribution at the local temperature and τ is the relaxation time which is a function of position and momentum.

For phonon transport, because no external force exists, Eq. (1.2) takes on the following form

$$\frac{\partial n_{\mathbf{K},p}}{\partial t} + \boldsymbol{\nu}_{\mathbf{K},p} \cdot \nabla n_{\mathbf{K},p} = \left(\frac{\partial n_{\mathbf{K},p}}{\partial t}\right)_{scattering} \quad , \tag{1.4}$$

where n is the phonon excitation number for a phonon of wave vector $\mathbf{K}$ and polarization p, which at equilibrium is given by the Bose-Einstein distribution function, and $\boldsymbol{\nu}$ is the phonon group velocity. The collision term on the right hand side of Eq. (1.4) consists of various forms of phonon scattering such as three-phonon scattering, geometric boundary scattering, and isotope scattering.

In the past, analytical models were used to solve the BTE for phonons in the relaxation time approximation to predict thermal conductivities in semiconductor materials [4–6]. Approximations to phonon dispersion and the use of relaxation time expressions for three-phonon interactions that contained approximations within themselves were commonly used. Further detail on these limiting assumptions have

been discussed in literature [7, 8]. The usage of these models has been limited to simplified cases.

Numerical solutions of the BTE have been obtained for modeling thermal transport in semiconductor materials [9–15]. The relative merits of the techniques such as the finite volume method [9, 11] and the Monte Carlo (MC) method [10, 12–15] used to numerically solve the BTE have been reviewed previously [16, 17]. Due to the expensive computational costs associated with these numerical solutions, most work in solving thermal transport has been limited to problems with simplified geometries. Using a Monte Carlo (MC) technique to stoichastically solve the BTE offers the potential of modeling thermal transport in complex geometries.

1.3.2 Molecular Dynamics Technique. In the molecular dynamics (MD) simulation technique the motion of atoms interacting with a prescribed interatomic potential, as shown in Fig. 1.1, are predicted using Newton's laws of motion. There are two distinct approaches used in MD simulations: equilibrium and non-equilibrium. In non-equilibrium MD, a non-equilibrium condition is typically initialized by imposing a temperature gradient to the boundary regions of the simulation domain. Thermal conductivity can be determined by computing the ratio of the imposed heat flux to the temperature gradient. In general, nonequilibrium techniques suffer from three major drawbacks:

1. the simulation domain must contain enough atoms in the boundary regions to stabilize the boundary temperatures, which increases the overall cost of the simulation;
2. the systems that can be simulated with current computing technologies are smaller than the phonon mean free path and their small size also restricts the maximum phonon wavelength;

3. an unphysically large temperature gradient is required to converge temperature statistics, making it difficult to determine the thermal conductivity at a particular temperature [18].

Nonequilibrium MD simulation techniques have been applied to various nanoscale and nanostructured materials including nanowires [19], superlattice nanowires [20], and thin films [21]. In equilibrium MD, small statistical temperature fluctuations cause instantaneous heat fluxes. Using the heat flux autocorrelation function and the Green-Kubo relationship, thermal conductivity can be determined [22]. Convergence is slow, but the equilibrium approach is free from the drawbacks associated with the nonequilibrium technique [18]. Equilibrium methods have been used recently to predict thermal conductivities in nanofilms, nanowires, and nanoparticles [22].

In addition to using MD techniques to determine thermal conductivities of various materials [23, 24], MD simulations have been used to study interfacial thermal transport [25, 26]. Also, from the time histories of individual atoms in a MD simulation, phonon spectral properties can be analyzed by discrete Fourier methods. Thus, relaxation times and other important properties such as group velocities and density of states can be determined [27, 28]. These properties could be incorporated into a BTE or Monte Carlo (MC) model to improve the accuracy of thermal transport calculations. Unfortunately, using MD techniques it is not possible to distinguish between phonon-phonon scattering processes. Therefore a full understanding of the complex nature of intrinsic scattering is not possible. The major limitations of MD simulations of thermal transport are the determination of accurate potentials and the size of systems that can be studied with reasonable computational time.

1.3.3 Monte Carlo Technique. The use of the MC method stems from work done in the 1940's where the method was utilized to solve neutron diffusion problems [29]. The MC method is a numerical method of approximately solving mathematical and physical problems by random sampling. MC methods are used in a wide range of applications such as computational physics, structural mechanics,

reliability theory, IC design, and stock market forecasting [30]. A crucial task in the application of the MC method is the generation of appropriate random samples [30]. Thus, the generation of random or pseudo-random numbers are essential to the MC method. The success of a MC calculation often is decided by how well the random samples reflect true randomness [30].

1.3.4 Monte Carlo Technique in Thermal Transport. The MC technique in thermal transport involves modeling phonons as individual particles as described by Fig. 1.3, tracking them as they drift and interact in various forms of scattering over a period of time. In the MC technique many phenomena associated with phonon transport are approximated utilizing pseudo-random number generation in a probabilistic manner. To assist in understanding the MC model overview, consider a rectangular geometry with isothermal boundary conditions at each end along the x-axis illustrated in Fig. 1.4.

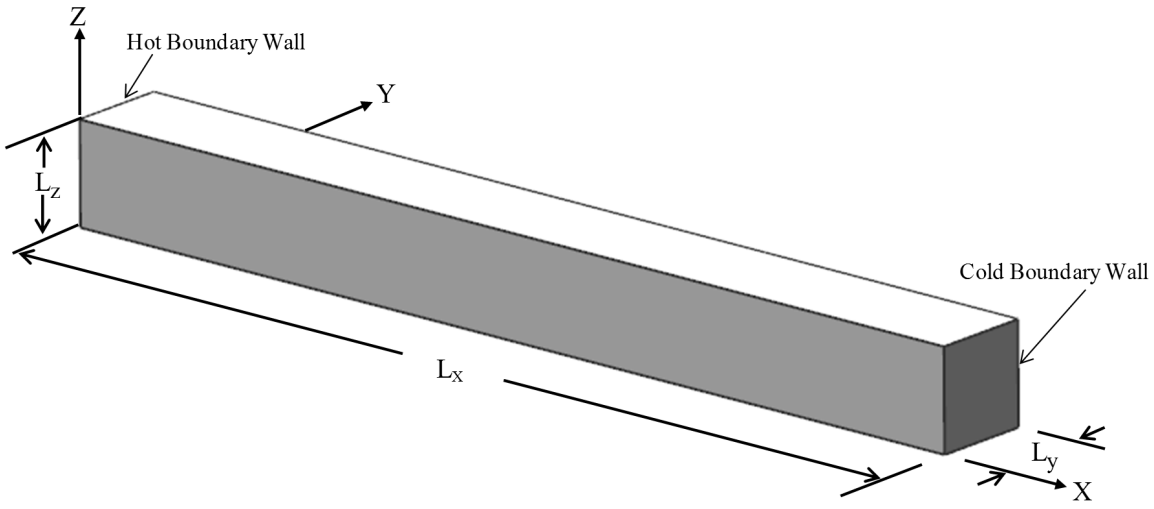

Figure 1.4 A rectangular parallelepiped geometry with isothermal boundary conditions at the x-axis minimum and maximum walls.

In the MC technique, the geometric domain is divided into cells or spatial bins. An initialization step occurs in which phonons are randomly positioned in the cells that make up the geometric domain. The equilibrium number of phonons introduced is

determined from the Bose-Einstein distribution. Typically, this number is quite large even for relatively small domains, therefore scaling factors are employed to reduce the actual population of phonons down to something that is computationally manageable. Once all cells within the domain are populated, for each phonon the properties of frequency, polarization, and direction are randomly assigned. The group velocity of each phonon is then determined using the frequency and polarization along with the isotropic dispersion curves. At the isothermal walls, the emitted phonon flux required to represent the isothermal wall temperature is determined. Following initialization, a drift step occurs in which each individual phonon moves in straight line at its individual group velocity and direction for a given time step. The positions of each phonon are individually tracked. If a geometric boundary is encountered, phonons will either specularly or diffusely reflect. Next, a scattering step occurs in which phonons are allowed to engage in scattering events such as three-phonon scattering and phonon-impurity scattering. The scattering step results in modifying individual phonon properties. The combination of the drift and scattering steps mimics the particle picture of phonon transport. At this point in the model one time step is complete and an effective temperature distribution can be determined based on the individual cell energies. Also, the effective thermal conductivity can be determined. This is done by computing the total heat flux based on the total energy emitted from the emitting walls and the total energy incident on the emitting walls during this time step. Energy and momentum conservation rules are not directly imposed for each scattering interaction in such a MC model. Energy conservation is imposed in an approximate way. Before the scattering step of phonon transport, a target energy is computed in each cell. Upon completion of the scattering step, phonons are added or removed from each cell to ensure that the target energy remains unchanged. The MC technique can be computationally intensive since it requires tracking a large number of energy carriers. Being able to treat complex problems with nontrivial geometries makes MC advantageous.

1.3.5 Previous Studies Utilizing the Monte Carlo Solution Technique . The MC solution technique solves the BTE in a statistical framework. It has been used extensively for thermal radiation computations [31] as well as in the simulation of electron transport in microelectronic devices [32]. Its usage for simulating phonon transport is relatively recent. [12–15, 33–39]

Early studies using the MC technique focused on being able to demonstrate both the diffusive and ballistic thermal transport regimes. Also, thermal conductivities of bulk materials as well as thin films were determined. Klitsner et al. [35] applied the MC technique to study radiative phonon transport in a crystal. Phonons were assumed to travel ballistically between the crystal surfaces. Scattering in this model only occured at the interfaces. Peterson [33] used a MC technique based on the Debye model, in which all phonons were assumed to have the same velocity. The interactions between phonons were accounted for by assuming an average phonon lifetime. More recently, Mazumder and Majumdar [12] developed a comprehensive MC model based on Peterson's work [33] that included both polarization and isotropic non-linear phonon dispersion. The various phonon scattering processes were considered independently. The model was used to investigate thermal transport in three-dimensional geometries and predict thermal conductivities in silicon. This model captured both the diffusive and ballistic transport regimes. Results showed that by fitting one parameter using experimental thermal conductivity data at one temperature, predictions of silicon thermal conductivity agreed well with experimental data over a wide temperature range. Lacroix *et al.* [13] utilized a model very similar to Mazumder and Majumdar's [12] to study phonon transport in silicon and germanium in both the diffusive and ballistic regimes. Their model incorporated a new distribution function in order to respect energy conservation during phonon scattering processes.

Knowing that the classical regime of thermal transport would not hold in all cases and quantum effects would become necessary to consider, Chen [14] used the MC technique to study phonon transport in single crystalline silicon nanowires. Sim-

ilarly, this model was based on the work of Mazumder and Majumdar [12]. A genetic algorithm which met both momentum and energy conservation requirements was used to model three-phonon normal and Umklapp processes. The results from this model showed that for high temperatures it is necessary to include momentum conservation for normal processes to accurately model thermal conductivity. Chen [14] also compared silicon nanowire thermal conductivity using both a dispersion relation solved from elastic wave theory and one from experimental data of bulk silicon. The results suggested that the confinement effect was significant when the nanowire diameter appoached tens of nanometers.

In order to decrease computational time, Song [34] used a slightly different approach to study microporous silicon thin films. His work used a gray-media approach and a unit cell concept. The thermal conductivity values of simulated solid and porous silicon films were generally higher than corresponding experimental results. This was attributed to usage of the gray-media approximation since long wavelength phonons that have a long mean free path are more sensitive to the presence of closely spaced boundaries. Song mentioned that pore orientation did not significantly affect the thermal conductivity. This model was limited by the size of the computational domain and the usage of the gray-media approximation. With a larger computational domain, a better study of randomly oriented micropore sizes and orientations could be done.

As a first attempt to determine thermal conductivities of nanocomposite materials with the MC technique, Yang [36] used an approach very similar to Song [34] to model silicon/germanium nanocomposites. The model incorporated both the gray-media approximation and the unit cell concept. The size effects of phonon transport in nanocomposites were studied. Results showed that the thermal conductivity of nanoparticle composites could be lower than the alloy value. Size and position of the silicon nanoparticles within the germanium host were studied. It was found that randomly distributed nanoparticles in nanocomposites resulted in thermal conduc-

tivities similar to that of periodically aligned mono-size nanoparticles. This model seemed to suffer from the same issues as Song's model.

These MC models all utilize approximations related to the polarization and dispersion behavior of phonons as well as the representation of three-phonon scattering. In order to obtain accurate thermal transport results, these approximations need to be more robust.

1.4 Motivation for Modeling Thermal Transport

1.4.1 Thermoelectrics. The field of thermoelectrics provides motivation for modeling thermal transport in nanostructures. The simplest thermoelectric generator consists of a thermocouple, shown in Fig. 1.5. The thermocouple has two legs, one of which is an N-type semiconductor and contains negatively charged mobile carriers in the form of electrons, while the other leg is a P-type semiconductor and contains positively charged mobile carriers called holes. These two legs are connected electrically in series and thermally in parallel. In the presence of an externally applied temperature gradient, the carriers conduct heat from the hot junction to the cold junction. This causes a voltage drop to occur between the two electrodes. The generation of voltage across a material for an applied temperature gradient is known as the Seebeck effect.

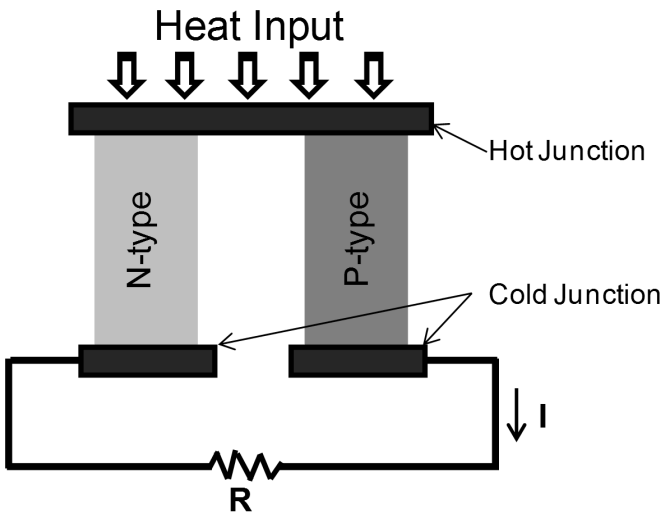

Figure 1.5 Illustration of thermoelectric generation.

In a thermoelectric cooler, current is passed through the legs of the thermocouple as shown in Fig. 1.6.

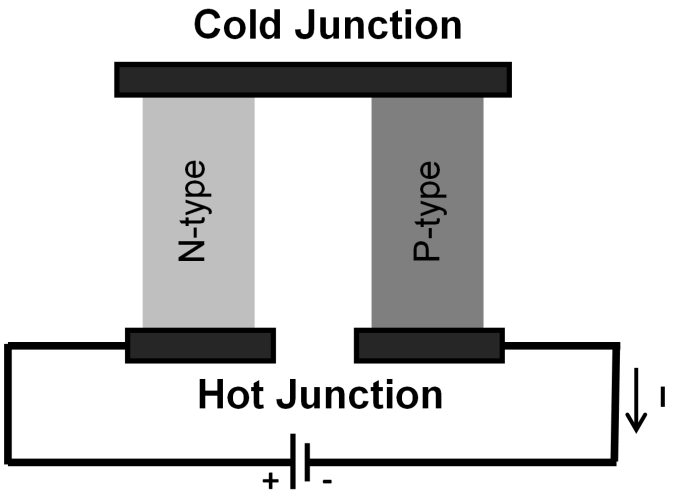

Figure 1.6 Illustration of thermoelectric cooling.

Both the electrons and holes carry heat away from the cold junction. The temperature gradient between the hot and cold junction varies with the amount of applied current. In addition to cooling, when current is applied, heat generation due to Joule heating occurs within each leg. The magnitude of Joule heating is equal to the product of the

square of the current and the electrical resistance of the leg. Therefore, thermoelectric materials with low resistivity are necessary. Additionally, in order to prevent the back-flow of heat from the hot to cold junctions, materials with a low thermal conductivity are also required.

In a typical thermoelectric device, N-type and P-type thermoelectric elements are sandwiched between two high thermal conductivity substrates. State of the art thermoelectric elements are based on Bi_2Te_3 and its alloys. Thermoelectric devices follow the same principles as previously discussed. Most thermoelectric modules are square with a range in length and width from approximately 2.5 - 50 mm and in height from approximately 2.5 - 5mm [40].

Thermoelectric performance is measured in terms of the figure of merit (ZT) defined as follows:

$$ZT = \frac{S^2\sigma}{k} \quad , \tag{1.5}$$

where S is the Seebeck coefficient, σ is the electrical conductivity, and k is the thermal conductivity. A material with high thermoelectric performance needs to have a large Seebeck coefficient (low carrier concentration semiconductors and insulators), a large electrical conductivity (high carrier concentration metals), and a low thermal conductivity. The ideal thermoelectric material is an electron crystal - phonon glass where high mobility electrons are free to transport charge and heat, but the phonons are disrupted at the atomic scale from transporting heat [41]. Heavily doped semiconductor materials allow the thermal conductivity to be reduced without degrading the electrical conductivity. In nanoengineered materials, thermal conductivity can be reduced by size, surface, and interfacial effects. This reduction in thermal conductivity is directly related to the performance increase in thermoelectric devices. Therefore, an accurate model for determining thermal conductivity of nanoengineered materials would be beneficial.

1.4.2 Nanostructured Materials. Alloying results in a reduction in thermal conductivity compared to that of the bulk constituents without a significant reduction

in electrical conductivity. This is due to mass difference scattering. Experimental and theoretical results show that the thermal conductivity of nanstructures, such as superlattices, can be less than that achieved through alloying. Size effects discussed are mainly responsible for this. Additionally, it has been demonstrated that dispersion relations change when length scales are on the order of 10 nm [14, 42].

Superlattices are periodic semiconductor structures as shown in Fig. 1.7.

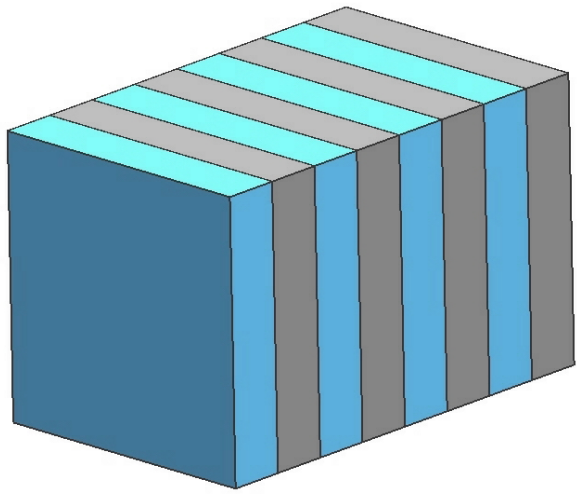

Figure 1.7 Depiction of a superlattice structure where the two different colors represent two different materials.

Recently it has been reported that Bi_2Te_3/Sb_2Se_3 superlattices [43] and PbTe/PbTeSe based quantum dot superlattices [44] result in a ZT>1. There have been numerous studies, both experimental and theoretical, on the thermal conductivity of superlattices. Even though superlattices are promising low thermal conductivity materials, thin film deposition fabrication techniques are not suitable for large scale applications [36]. Thus, nanoporous and nanocomposite materials have been proposed as alternatives to superlattices.

Nanocomposite materials consist of nanowires, nanotubes, or nanoparticles embedded in a host semiconductor material as shown in Fig. 1.8.

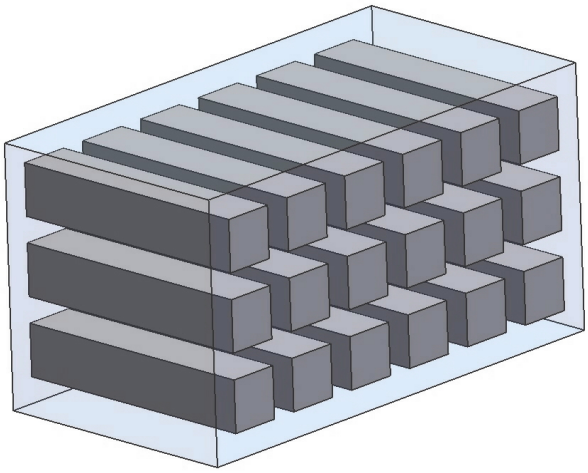

Figure 1.8 Depiction of a nanocomposite structure with nanowires embedded in a host material.

Recently Zhao et al. [45] reported promising results of a reduction in effective thermal conductivity of a Bi_2Te_3 nanocomposite with tubular Bi_2Te_3 nanowire inclusions. It is believed that nanocomposites may provide a way to enhance the nanoscale effects observed in superlattices [46, 47]. If nanocomposites are to be used to increase ZT it is important to consider constituent materials that have significant differences in lattice properties, but negligible differences in electrical properties.

1.5 Statement of Work

The potential to engineer nanostructured materials to have desired thermal properties for various applications is rapidly gaining attention. To effectively engineer materials, it is necessary to have robust numerical models that can accurately predict thermal transport. When a structure has a characteristic length on the order of tens of nanometers, phonon scattering at material interfaces and domain boundaries dominate heat transfer, making macroscale theory (diffuse regime) ineffective in predicting thermal transport.

The goal of the Statistical Phonon Transport (SPT) model presented herein is to provide a probabilistic simulation that can model thermal transport in crystalline

materials from nanoscale (ballistic regime) to the macroscale (diffuse regime). The SPT model aims to

1. approximate the BTE while rigorously enforcing the conservation of energy and pseudo-momentum selection rules,
2. employ a fully anisotropic model for the dispersion characteristics of silicon in stochastic modeling of phonon transport,
3. extend the accuracy of phonon transport by eliminating the need to use scaling factors common to MC techniques, thus truly modeling actual phonon populations across various length scales,
4. provide a framework to permit side-by-side comparisons of alternative scattering algorithms,
5. provide a framework to permit side-by-side comparison of alternative scattering interaction selection rules,
6. provide a foundation to study the phenomena of ballistic jump at isothermal boundaries evident in many MC models,
7. provide a foundation for modeling thermal conductivity of nanomaterials
8. allow modeling of acoustic or acoustic + optical phonon branches,
9. be extendable to complex three-dimensional geometries necessary for engineering device design,
10. incorporate a probabilistic treatment of phonon transport that does not require the use of pseudo-random number generation.

CHAPTER 2

Introduction to Crystal Structure and Phonon Theory

Knowledge of the structure of solids is fundamental in the study of solid state physics. Most physical properties of solids are dependent on how atoms or molecules that make up the solid are arranged. In this work, we aim to understand the energy quanta that are related to lattice vibrations of a crystal, called phonons. Here an introduction to crystal structure and phonon theory related to bulk silicon is given as a foundation for further discussions concerning the intricate mechanisms of phonon transport.

2.1 Crystalline Solids

An ideal crystal is an infinite three-dimensional periodic array of groups of atoms in space. The group of atoms, known as the basis, may consist of one or more atoms. The three-dimensional configuration of points to which the basis is attached is called the lattice. The crystal is defined by the addition of the basis to every point in the lattice. Silicon is a group IV element having a diamond crystal structure as depicted in Fig. 2.1.

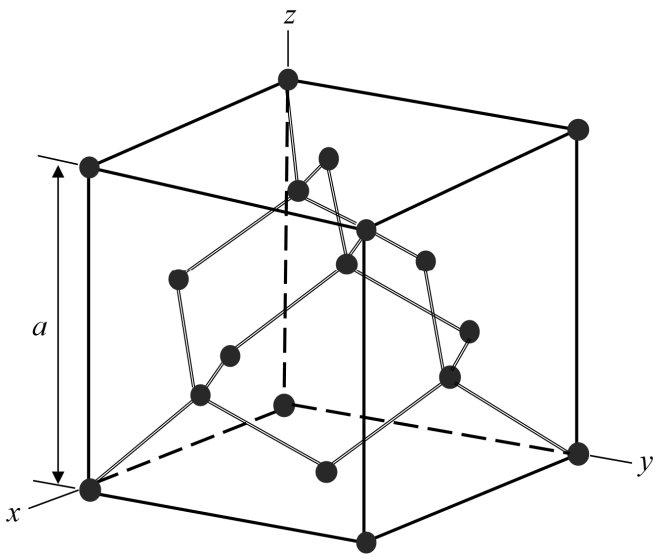

Figure 2.1 Diamond crystal structure.

The diamond crystal structure consists of a face-centered cubic (FCC) lattice, shown in Fig. 2.2, with a diatomic basis at coordinates $(0, 0, 0)$ and $(\frac{1}{4}, \frac{1}{4}, \frac{1}{4})$ associated with each point of the FCC lattice.

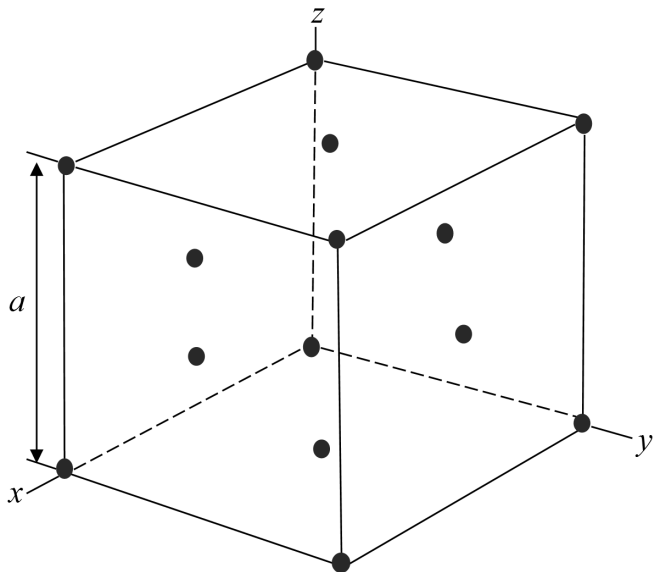

Figure 2.2 A unit cell for the face-centered cubic lattice.

The lattice can be described by three translational vectors $\mathbf{a}_1$, $\mathbf{a}_2$, and $\mathbf{a}_3$ such that the arrangement of atoms in the crystal appear the same when viewed from point $\mathbf{r}$ as when viewed from any other point $\mathbf{r}'$ translated by an integral multiple of three translational vectors

$$\mathbf{r}' = \mathbf{r} + \ell_1\mathbf{a}_1 + \ell_2\mathbf{a}_2 + \ell_3\mathbf{a}_3 \quad , \tag{2.1}$$

where ℓ_1, ℓ_2, and ℓ_3 are integers which will be referred to collectively as ℓ [48]. If every point equivalent to $\mathbf{r}$ is included in the set $\mathbf{r}'$, the lattice points and translation vectors are primitive. The parallelpiped defined by the primitive axes $\mathbf{a}_1$, $\mathbf{a}_2$, and $\mathbf{a}_3$ is called the primitive cell. A primitive cell consists of one lattice point. The primitive cell for an FCC lattice is shown in Fig. 2.3.

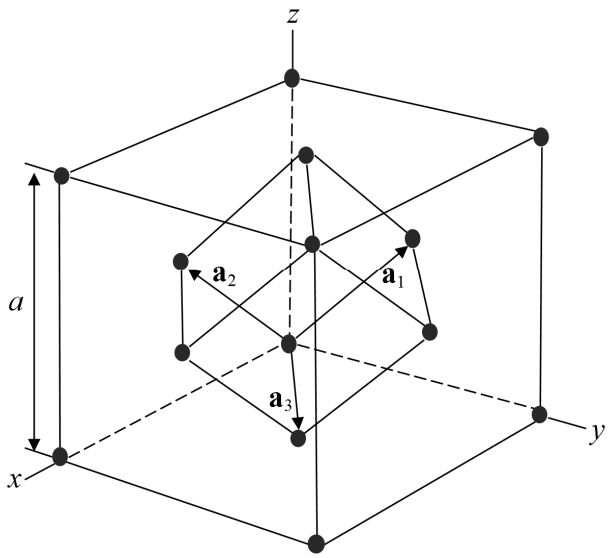

Figure 2.3 The primitive cell of the face-centered cubic crystal. The primitive translation vectors connect the lattice point at the origin with lattice points at the face centers.

By drawing perpendicular bisector planes of the line segments connecting a single lattice point to all the nearby lattice points, a Wigner-Seitz primitive cell is created. The Wigner-Seitz cell for an FCC lattice is shown in Fig. 2.4.

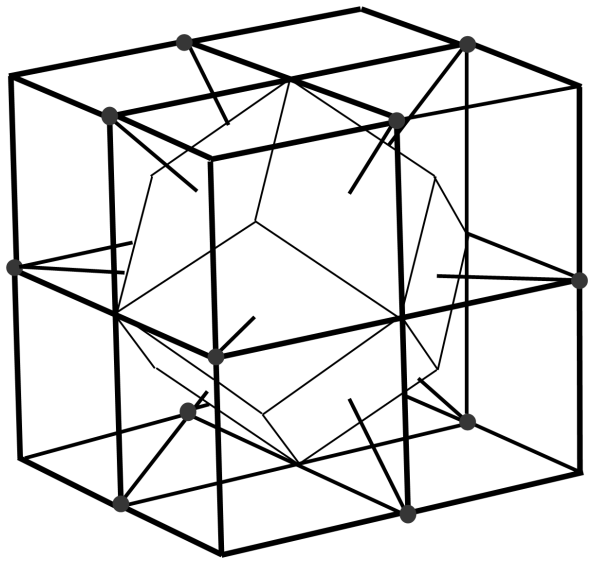

Figure 2.4 The Wigner-Seitz cell for a face-centered cubic lattice.

The Wigner-Seitz cell is the region for which locations in the cell are nearer to the central lattice point than any other lattice point. The volume of the Wigner-Seitz cell is given as

$$\mathbf{\Omega} = \mathbf{a}_1 \cdot (\mathbf{a}_2 \times \mathbf{a}_3) \quad . \tag{2.2}$$

2.2 Reciprocal Lattice and First Brillouin Zone

Lattices are periodic structures and position-dependent physical properties that depend on the structural arrangement of the atoms are also periodic. As any quantity which varies with time can be described as a sum of Fourier components in the frequency domain, the spatial properties of a crystal can be described as the sum of components, in Fourier space, or reciprocal space [49]. For a given real space lattice, a reciprocal space lattice can be defined in terms of three primitive reciprocal lattice vectors $\mathbf{b}_1$, $\mathbf{b}_2$, and $\mathbf{b}_3$, which are related to the real space lattice vectors by

$$\mathbf{b}_i = 2\pi \frac{(\mathbf{a}_j \times \mathbf{a}_k)}{(\mathbf{a}_1 \times \mathbf{a}_2) \cdot \mathbf{a}_3} \quad , \tag{2.3}$$

where i, j, and k represent a cyclic permutation of the indices 1, 2, and 3. The Wigner-Seitz primitive cell of an FCC real space lattice in reciprocal space is known

as the first Brillouin zone (BZ). The BZ can be defined as the smallest polyhedron confined by planes perpendicularly bisecting the reciprocal lattice vectors, as depicted in Fig. 2.5 for an FCC real space lattice [50].

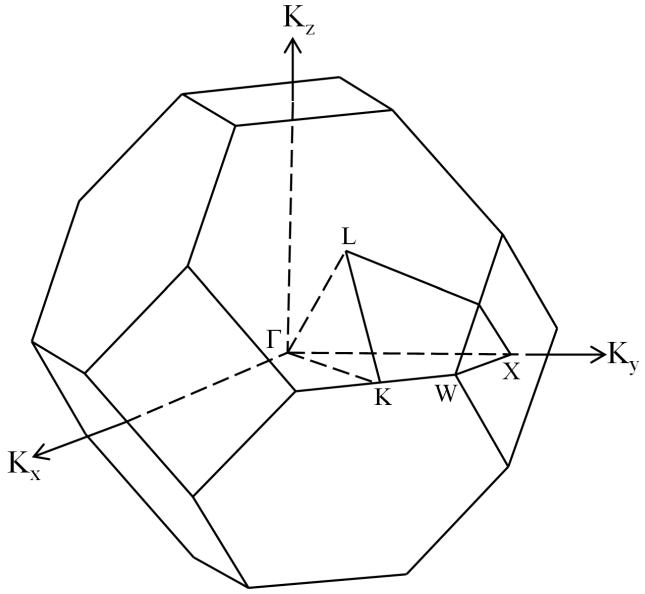

Figure 2.5 Brillouin zone of a face-centered cubic real space lattice in reciprocal space with the irreducible wedge depicted.

The volume of the BZ, V_{BZ}, is given as

$$V_{BZ} = \mathbf{b}_1 \cdot (\mathbf{b}_2 \times \mathbf{b}_3) = \frac{(2\pi)^3}{\Omega} \quad . \tag{2.4}$$

The BZ contains 14 reciprocal lattice vectors, eight vectors in $\langle 111 \rangle$ directions with a length of $\sqrt{3} \cdot 2\pi/a$ and six vectors in the $\langle 100 \rangle$ directions with a length of $2 \cdot 2\pi/a$. The anisotropy and shape of the BZ is of special importance when considering lattice vibrations and how they affect thermal transport.

2.3 Excitation Level

Phonons follow the Bose-Einstein statistical distribution, therefore at thermal equilibrium the excitation number of a phonon having wave vector, $\mathbf{K}$, and polariza-

tion, p, is given by [51] as

$$n_{\mathbf{K},p} = \frac{1}{exp\left(\frac{\hbar\omega_{\mathbf{K},p}}{k_B T}\right) - 1} \quad , \tag{2.5}$$

where ω is the phonon frequency, $\hbar$ is Plank's constant divided by 2π, T is the temperature, and k_B is Boltzmann's constant. Excitation numbers are properties of the crystal and completely independent from the spatial domain volume. During thermal transport excitation numbers will transition while maintaining the energy of the spatial domain constant [42].

The total energy of a crystal can be written according to [51] as

$$\widetilde{U} = \sum_{p} \sum_{\mathbf{K}} \hbar\omega_{\mathbf{K},p} n_{\mathbf{K},p} \quad . \tag{2.6}$$

The summation in Eq. (2.6) is performed over all polarizations (longitudinal optical (LO), transverse optical (TO1, TO2), longitudinal acoustic (LA), and transverse acoustic (TA1, TA2)) and over wave vector space. In considering a spatial domain of volume V_{domain}, the number of phonon wave packets having polarization p and having a wave vector in the neighborhood $\delta\mathbf{K}$ about $\mathbf{K}$ is given by [42] as

$$N_{\mathbf{K},p} = \frac{V_{domain}}{\Omega}\left(\frac{\delta\mathbf{K}}{V_{BZ}}\right) n_{\mathbf{K},p} = \frac{V_{domain}}{\Omega}\frac{\delta\mathbf{K}}{(2\pi)^3/\Omega} n_{\mathbf{K},p} = \frac{V_{domain}\delta\mathbf{K}}{(2\pi)^3} n_{\mathbf{K},p} \quad , \tag{2.7}$$

where Ω is the volume of the Wigner-Seitz cell of the Bravais lattice and V_{BZ} is the volume of the BZ. It is important to emphasize that the number of wave packets is dependent on the spatial domain volume, V_{domain}.

2.4 Phonon Dispersion

In order to account for the anisotropy associated with the BZ as well as the polarization and frequency dependence that distinguish phonon wave packets from one another, it is necessary to compute dispersion curves for arbitrary wave vectors.

Many models [12–15, 33–39] use an isotropic assumption for dispersion. In order to accurately model the complex nature of phonon transport an isotropic assumption is insufficient. Therefore, it is necessary to develop a robust method for computing dispersion curves. In this chapter a lattice dynamics (LD) approach to compute phonon dispersion is introduced. Dispersion curves of bulk silicon are calculated and group velocity data is extracted. The LD model presented in this chapter is incorporated into a preprocessing step in the SPT model.

2.4.1 Lattice Dynamics. The lattice dynamics model used to determine the frequency given an arbitrary wave vector and polarization was adopted from Ghatak and Kothari [48]. Their model is a semi-classical LD model that assumes the harmonic approximation to find the normal modes of a crystal. Therefore, the force acting on an atom is linearly proportional to the displacement of that atom from its equilibrium position. Their model also assumes that nearest neighbor atoms interact with angular forces and next-nearest neighbor atoms interact with central forces. While other approaches such as the adiabatic bond charge models [52] have better agreement with experimental data [9], the LD method was incorporatated into the SPT model for convenience of computation.

2.4.2 Equation of Motion. As previously described in § 2.1, the equilibrium position of any point in a perfect lattice of infinite extent in all directions is given as

$$\mathbf{r}\left(\ell\right) = \ell_1\mathbf{a}_1 + \ell_2\mathbf{a}_2 + \ell_3\mathbf{a}_3 \quad , \tag{2.8}$$

where ℓ_1, ℓ_2, and ℓ_3 are integers which will be referred to collectively as ℓ. The vectors $\mathbf{a}_1$, $\mathbf{a}_2$, and $\mathbf{a}_3$ are the primitive translation vectors of the lattice. As a result of thermal fluctuations, an atom can get displaced from its equilibrium position by an amount $\mathbf{u}(\ell)$. Its components can be written as $u_\alpha(\ell)$, where $\alpha = 1, 2,$and 3 corresponding to

the x, y, and z directions, respectively. The total kinetic energy of the lattice is then

$$\widetilde{T} = \frac{1}{2} M_A \sum_{\ell} \sum_{\alpha} \dot{u}_{\alpha}^2 (\ell) \quad , \tag{2.9}$$

where M_A is the atomic mass. The potential energy of the lattice, $\widetilde{V}$, can be expanded in a Taylor series in powers of atomic displacement $\mathbf{u}(\ell)$ as

$$\widetilde{V} = \widetilde{V}_0 + \sum_{\ell} \sum_{\alpha} \widetilde{V}_{\alpha} u_{\alpha} (\ell) + \sum_{\ell} \sum_{\ell^+} \sum_{\alpha} \sum_{\beta} \widetilde{V}_{\alpha\beta} (\ell\ell^+) u_{\alpha} (\ell) \, u_{\beta} \left(\ell^+\right) + \ldots \quad , \tag{2.10}$$

where $\widetilde{V}_0$ is the potential energy of the lattice corresponding to the equilibrium configuration of the atoms [48]. The negative of the gradient of the potential given as

$$\widetilde{V}_{\alpha} (\ell) = \left. \frac{\partial \widetilde{V}}{\partial u_{\alpha} (\ell)} \right|_0 \quad , \tag{2.11}$$

represents the force acting on an atom at $\mathbf{r}(\ell)$. At equilibrium the net force on each atom must be zero. Thus, under the harmonic approximation higher order terms of the potential energy in the Taylor series expansion shown in Eq. (2.10) are neglected, therefore the potential energy of the lattice simplifies to

$$\widetilde{V} = \sum_{\ell} \sum_{\ell^+} \sum_{\alpha} \sum_{\beta} \widetilde{V}_{\alpha\beta} (\ell\ell^+) u_{\alpha} (\ell) \, u_{\beta} \left(\ell^+\right) \quad , \tag{2.12}$$

where

$$\widetilde{V}_{\alpha\beta} \left(\ell\ell^+\right) = \left. \frac{\partial^2 \widetilde{V}}{\partial u_{\alpha} (\ell) \, \partial u_{\beta} \left(\ell^+\right)} \right|_0 \quad . \tag{2.13}$$

From Eqs.(2.9) and (2.12) using the Lagrangian procedure of classical mechanics, the equation of motion of the lattice is

$$M_A \ddot{u}_{\alpha} (\ell) = \sum_{\ell^+} \mathbf{F}_{\alpha} \left(\ell^+\right) \quad , \tag{2.14}$$

where

$$\mathbf{F}_\alpha\left(\ell^+\right) = -\sum_\beta \widetilde{V}_{\alpha\beta}(\ell\ell^+)u_\beta\left(\ell^+\right) \quad . \tag{2.15}$$

$\mathbf{F}_\alpha\left(\ell^+\right)$ represents the α-component of forces acting on the ℓ^{th} atom when the ℓ^{+th} atom is displaced from its equilibrium position. Following the assumption that nearest neighbor atoms interact with angular forces and next-nearest neighbor atoms interact with central forces, the non-central forces acting on the ℓ^{th} atom from the ℓ^{+th} atom due to their displacements is

$$\begin{aligned}&\mathbf{F}\left(\ell^+\right) = \mathbf{F}_c\left(\ell^+\right) + \mathbf{F}_a\left(\ell^+\right)\\ &= \alpha_a\left[\mathbf{u}\left(\ell^+\right) - \mathbf{u}\left(\ell\right)\right] + \left(\alpha_c - \alpha_a\right)\left[\boldsymbol{\varepsilon}\left(\ell^+\right)\cdot\left(\mathbf{u}\left(\ell^+\right) - \mathbf{u}\left(\ell\right)\right)\right]\boldsymbol{\varepsilon}\left(\ell^+\right) \quad .\end{aligned} \tag{2.16}$$

The parameters α_c and α_a in Eq. (2.16), can be determined by fitting experimentally measured dispersion curves or from elastic constant data.

2.4.3 Dynamical Matrix and Secular Determinant. The equations of motion given by Eq.(2.14) form an infinite set of simultaneous differential equations. Due to the periodicity of the lattice, a solution of the following form can be assumed

$$u_\alpha\left(\ell\right) = A_\alpha exp[-i(\omega t - \mathbf{K}\cdot\mathbf{r}\left(\ell\right))] \quad , \tag{2.17}$$

where A_α represents the amplitude of the wave. Substituting Eq. (2.17) into Eq. (2.14) yields

$$\omega^2 A_\alpha = \sum_\beta D_{\alpha\beta}(\mathbf{K})A_\beta \quad , \tag{2.18}$$

where $D_{\alpha\beta}$ is the dynamical matrix given by

$$D_{\alpha\beta}(\mathbf{K}) = \frac{1}{M}\sum_{\ell^\star} \widetilde{V}_{\alpha\beta}(\ell\ell^+)exp[-i\mathbf{K}\cdot\left(\mathbf{r}\left(\ell^+\right) - \mathbf{r}\left(\ell\right)\right)] \; . \tag{2.19}$$

Equation (2.18) requires solving three linear homogeneous equations in three unknowns A_α. For confined structures the assumption of an infinite periodic lattice

is not valid therefore the dynamical matrix will be larger. Equation (2.18) can be rewritten as

$$\sum_{\beta}[D_{\alpha\beta}(\mathbf{K}) - \omega^2\delta_{\alpha\beta}]A_{\beta} = 0 \quad , \tag{2.20}$$

where $\delta_{\alpha\beta}$ is the Kronecker-delta function defined as $\delta_{\alpha\beta}$=1 if and only if α=β. For non-trivial solutions the determinant of the coefficients must equal zero

$$\left|D_{\alpha\beta}(\mathbf{K}) - \omega^2\delta_{\alpha\beta}\right| = 0 \quad , \tag{2.21}$$

Equation (2.21) is known as the secular determinant and is of the order $3s$, where s is the number of atoms in a unit cell. Thus, for diatomic crystals such as silicon, for a given value of $\mathbf{K}$ there will be $3s$ roots corresponding to 3 acoustic branches and ($3s$-3) optical branches.

2.4.4 Bulk Silicon Dispersion. For the diamond crystal structure of silicon the dynamical matrix is given as

$$D_{\alpha\beta}\left(\mathbf{K}\right) = \begin{bmatrix} A & 0 & 0 & B & C & D \\ 0 & A & 0 & C & B & E \\ 0 & 0 & A & D & E & B \\ B^* & C^* & D^* & A & 0 & 0 \\ C^* & B^* & E^* & 0 & A & 0 \\ D^* & E^* & B^* & 0 & 0 & A \end{bmatrix} \quad , \tag{2.22}$$

where

$$\begin{aligned} A &= 4(\tfrac{\alpha_c+2\alpha_a}{3}) \\ B &= -(\tfrac{\alpha_c+2\alpha_a}{3})(1 + e^{i\frac{(K_x+K_y)}{2}a} + e^{i\frac{(K_y+K_z)}{2}a} + e^{i\frac{(K_z+K_x)}{2}a}) \\ C &= -(\tfrac{\alpha_c-\alpha_a}{3})(1 + e^{i\frac{(K_x+K_y)}{2}a} - e^{i\frac{(K_y+K_z)}{2}a} - e^{i\frac{(K_z+K_x)}{2}a}) \\ D &= -(\tfrac{\alpha_c-\alpha_a}{3})(1 - e^{i\frac{(K_x+K_y)}{2}a} - e^{i\frac{(K_y+K_z)}{2}a} + e^{i\frac{(K_z+K_x)}{2}a}) \\ E &= -(\tfrac{\alpha_c-\alpha_a}{3})(1 - e^{i\frac{(K_x+K_y)}{2}a} + e^{i\frac{(K_y+K_z)}{2}a} - e^{i\frac{(K_z+K_x)}{2}a}) \end{aligned} \quad , \tag{2.23}$$

K_x, K_y, and K_z are the three components of an arbitrary wave vector $\mathbf{K}$, a is the lattice constant, α_c and α_a are the central and angular force constants, and B^*, C^*, D^*, and E^* are conjugate to B, C, D, and E, respectively [48]. In the present work, the central and angular force constants were determined by fitting to experimentally measured dispersion curves in the high symmetry directions. The values of the central and angular force constants used herein are 2.75 and 0.65, respectively.

Figure 2.6 shows dispersion curves for silicon obtained using the model previously described for high symmetry directions within the first BZ.

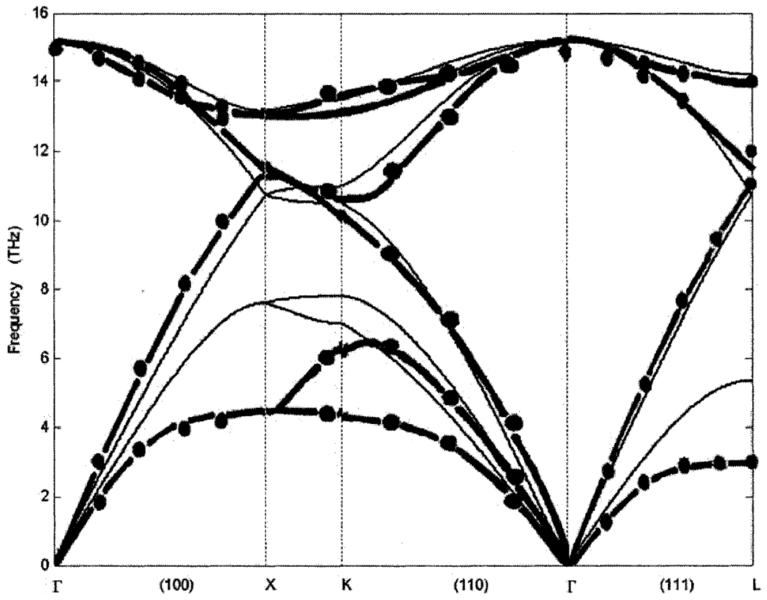

Figure 2.6 Dispersion curves for bulk silicon in high symmetry directions. The fine lines are from lattice dynamics, the thick lines are from the bond charge model and the solid circles are from experiment [9].

2.4.5 Thin Film Dispersion. The lattice dynamics model described throughout § 2.4.1 can also be utilized for the computation of dispersion relations in confined structures such as thin films and nanowires. In confined structures, physical boundaries influence the continuous spectrum of wave vectors in the BZ. It has been shown [42] by comparing the DOS, group velocities, and specific heat in silicon films and nanowires at various film thicknesses and wire diameters that confinement are

absent until film thicknesses are less than 10 nm and wire diameters are less than approximately 5 nm. Additionally, from comparisons of specific heat, confinement effects were observed only at temperatures below 100 K where the predominant phonon wavelengths are comparable with the physical dimensions of the structure [42].

2.5 Phonon Density of States

The density of states is defined as the number of energy levels between frequencies ω and $\omega + \delta\omega$, or, equivalently, between wave vectors $\mathbf{K}$ and $\mathbf{K} + \delta\mathbf{K}$ [53]. The density of phonon states $D(\omega)$ per unit volume is given by

$$D\left(\omega\right) = \frac{1}{V} \sum_{p} \sum_{\mathbf{K}} \delta(\omega - \omega_{\mathbf{K},p}) \quad , \tag{2.24}$$

where the summation is performed over all wave vectors in the BZ and all polarizations. A histogram technique can be used to compute the density of states following Eq. (2.24). A histogram is generated with equally spaced frequency bins that span the frequency band being considered for the given material. Then, using the lattice dynamics model described in § 2.4.1, frequencies for a large number of uniformly spaced wave vectors can be determined. Counting the number of frequencies within particular frequency intervals associated with the bins in the histogram results in the generation of a phonon density of states. A normalized density of states plot for bulk silicon is shown in Fig. 2.7.

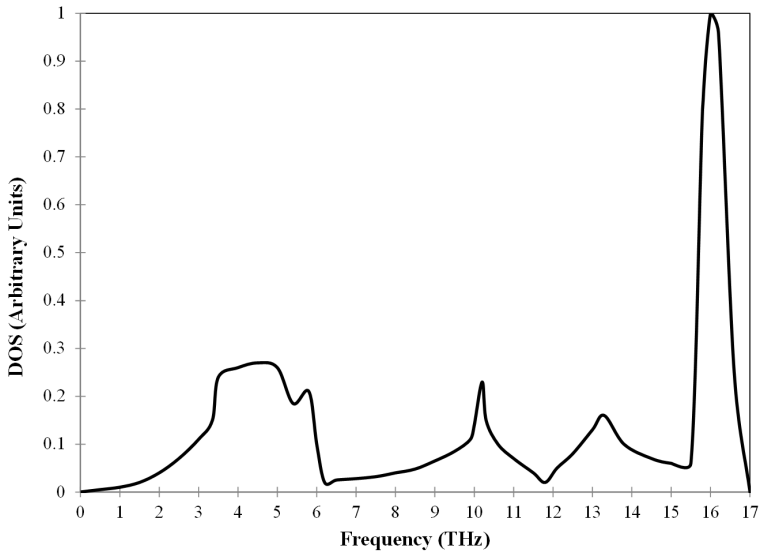

Figure 2.7 Density of states for bulk silicon adapted from [42].

It was mentioned in § 2.4.5 that confined structures result in dispersion relations that differ from that of bulk. It is noted that the DOS of confined structures will also differ from bulk.

2.6 Specific heat

The specific heat of a crystal is defined as a change in lattice energy density with respect to a change in temperature. Therefore, using Eq.(2.6) the lattice specific heat is given as

$$\begin{aligned} C_{lattice} &= \frac{1}{V}\sum_{p}\sum_{\mathbf{K}}\hbar\omega_{\mathbf{K},p}\frac{\partial n_{\mathbf{K},p}}{\partial T} = \frac{1}{V}\sum_{p}\sum_{\mathbf{K}}\hbar\omega_{\mathbf{K},p}\frac{\partial}{\partial T}\left(\frac{1}{exp\left(\frac{\hbar\omega_{\mathbf{K},p}}{k_BT}\right)-1}\right) \\ &= \frac{1}{V}\sum_{p}\sum_{\mathbf{K}}k_B\left(\frac{\hbar\omega_{\mathbf{K},p}}{k_BT}\right)^2\frac{exp\left(\frac{\hbar\omega_{\mathbf{K},p}}{k_BT}\right)}{\left(exp\left(\frac{\hbar\omega_{\mathbf{K},p}}{k_BT}\right)-1\right)^2} \quad . \end{aligned} \tag{2.25}$$

2.7 Phonon Group Velocity

In addition to having an accurate picture of the energy distribution within a crystal it is also important to understand how that energy propagates. The group

velocity is defined as the gradient in reciprocal space of the angular frequency. For a wave packet of wave vector $\mathbf{K}$ and polarization p, the group velocity is given as

$$\boldsymbol{\nu}_{\mathbf{K},p} = \nabla_{\mathbf{K}} \omega_{\mathbf{K},p} \quad . \tag{2.26}$$

The group velocities for acoustic and optical polarizations along the [100] direction of the BZ are shown in Fig. 2.8. These group velocities are computed using dispersion curves based on quadratic fits to experimental data in the [100] direction [10].

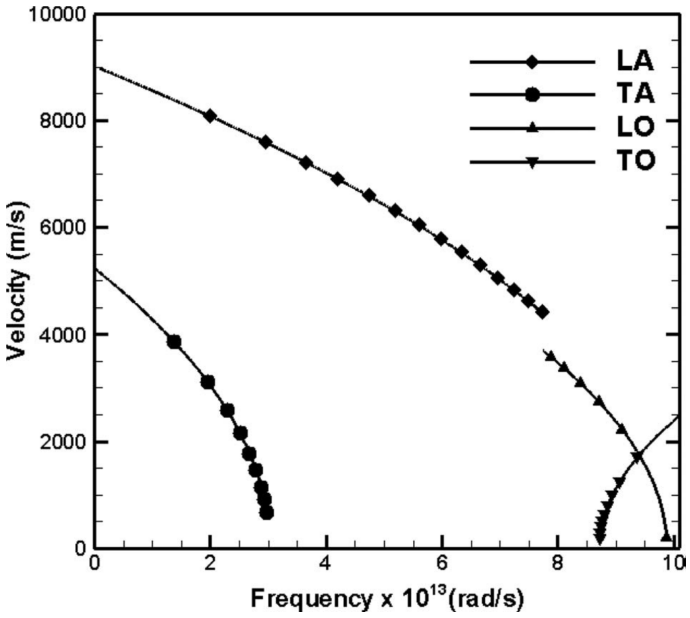

Figure 2.8 Group velocities for acoustic and optical phonon modes along the [100] direction in bulk silicon from [10].

CHAPTER 3

Introduction to The Statistical Phonon Transport Model

Micro- and nano-scale thermal transport modeling is of interest for a variety of applications ranging from modeling hot spots in semiconductor materials to developing novel materials having desired thermal properties. Increasingly accurate physics-based models of phonon transport are needed to support such applications. The semi-classical Boltzmann transport equation (BTE) can be used to model distributions of carriers and their numerous transport mechanisms. The MC method has been used successfully in simulating electron transport [32] and has been recently utilized to simulate phonon transport [10, 12–15]. The adaptability of the MC technique due to its probabilistic nature make it one of the most promising methods for simulating phonon transport. Most MC methods employ several approximations to reduce computational time, and include the use of scaling factors, approximations related to the polarization and dispersion behavior of phonons, and the representation of phonon-phonon scattering. In order to advance the field of thermal transport, these approximations must be addressed. The statistical phonon transport (SPT) model described herein obviates the need for several assumptions that currently limit the

MC technique, while retaining the probabilistic view of phonon transport that makes the MC technique so powerful.

3.1 Motivation for SPT Model Development

The primary goal of this research was to develop a full three-dimensional probabilistic simulation that could model thermal transport from nanoscale to bulk semiconductor materials. The motivation to develop a novel model for simulating phonon transport stems from the interest in being able to engineer materials that could have desired thermal transport characteristics, as mentioned in Chapter 1 § 1.4. Additional motivation came from the want to develop a model that could accurately predict thermal transport in semiconductor materials across multiple length scales with the ability to capture the complex transport mechanisms from the ballistic to diffuse transport regimes.

The modeling techniques reviewed in Chapter 1 § 1.3 show promise for various aspects of multiscale thermal transport modeling, but only the MC technique showed promise for being able to address most of the foreseen challenges. Significant research into the capabilities and limitations of the MC technique was performed. The following list of "strengths" and "weaknesses" of the MC technique was made. Surely some of these can be argued, but for the most part these statements accurately assess the technique and identify areas needing improvement.

MC Strengths:

1. Conceptually simple (model the physics of individual particles as they drift and scatter).
2. Capable of modeling complex geometries due to each particle being tracked.
3. Can treat various drift and scattering mechanisms individually.

MC Weaknesses:

1. Pseudo-random number generation requires that several runs of the same simulation be done so that results can be averaged.
2. Must track each particle's location throughout its entire lifetime which is computationally intensive.
3. Due to the computational requirements associated with having to track each particle throughout its lifetime, the use of scaling factors is required for most simulations.
4. The majority of works reported in the literature utilize an isotropic BZ. This is mainly due to computational requirements. This limits the scattering models to be based on the relaxation time approximation where heuristic parameters are commonly used to hone features of the three-phonon scattering so thermal transport results match experimental results.
5. Results have been shown to be dependent on the number of phonons considered.
6. The majority of works add or delete phonons at the end of scattering to conserve energy.
7. The isotropic assumption commonly used does not allow for pseudo-momentum to be conserved.

It is noticeable that there are several limitations to the model that could potentially lead to errors in predicted results. Although, even with all of the approximations and limitations in the MC technique, encouraging results related to thermal transport have been presented in the literature [10, 12–15]. Therefore, a model that could eliminate many of the weaknesses associated with the MC technique while retaining the positive aspects would be a significant contribution to the field.

3.2 SPT Model Algorithm Description

The structure of the SPT model algorithm in a serial processing framework is shown in the Fig. 3.1.

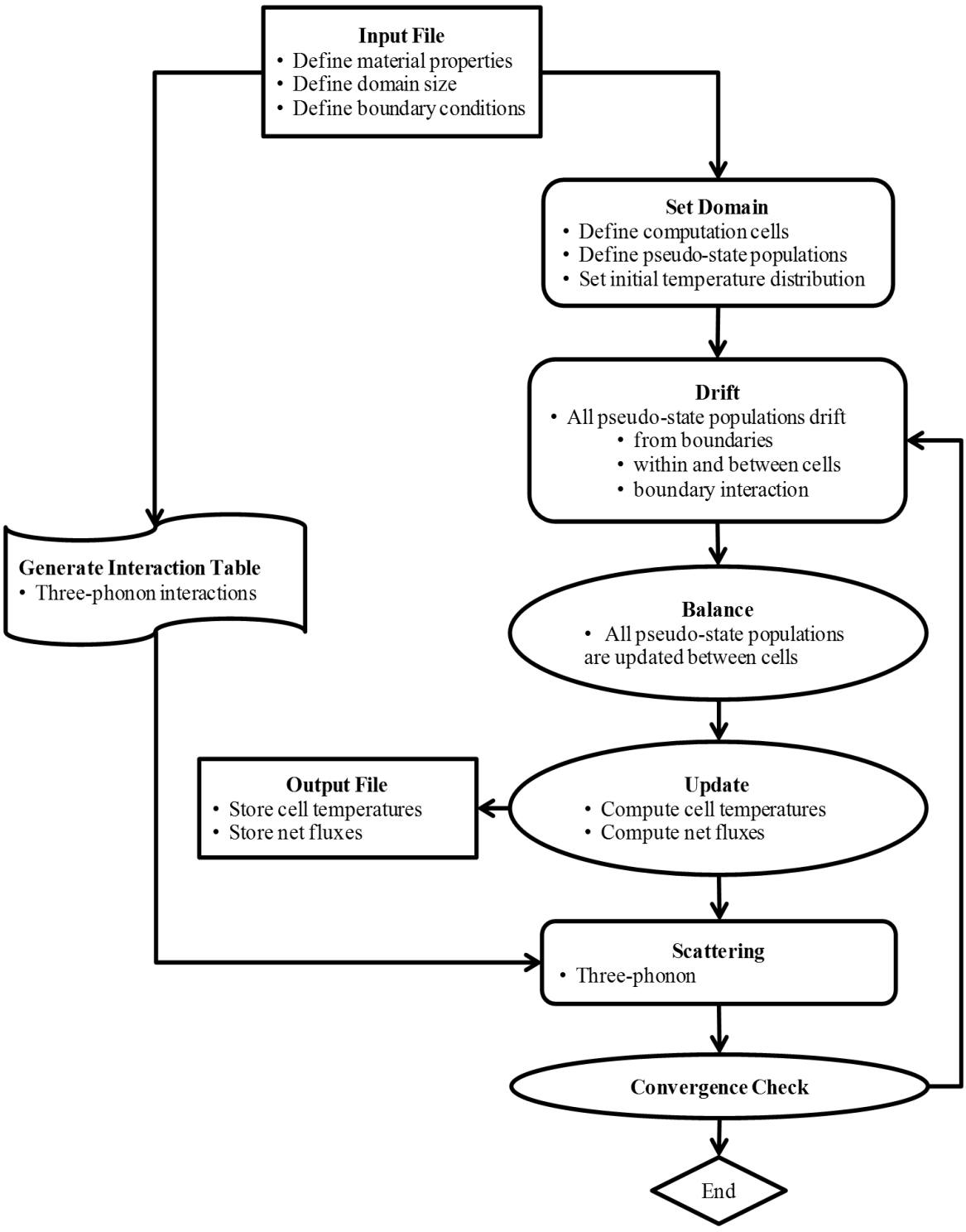

Figure 3.1 Flow chart of the SPT model algorithm.

The various aspects of the model depicted in Fig. 3.1 are described in the following sections. An example of the SPT model input file and a sample of the three-phonon interaction table can be found in the appendices.

3.3 SPT Model Assumptions

The following assumptions underlie the work to be presented herein.

1. Central and angular force constants used in a lattice dynamics model for computing dispersion curves are determined by fitting experimentally measured bulk silicon dispersion curves. The lattice dynamics model is used to determine the corresponding frequency for any arbitrary wave vector in the BZ.
2. The classical particle description of phonon transport is assumed. The critical domain dimensions are greater than the phonon coherence length and wavelength in silicon [54].
3. Bulk anisotropic phonon dispersion is considered. The critical domain dimensions are greater than those that would require consideration of confinement effects on dispersion [14].
4. A manually selected acceptance criteria, ω_ε is used for satisfying conservation of energy in the creation of a three-phonon interaction table. Conservation of pseudo-momentum is accomplished through the definition the pseudo-states. The influence of this assumption is evaluated herein.
5. Phonons are uniformly distributed over the **K**-space of a pseudo-state, with each phonon assigned the frequency, energy, and group velocity of the pseudo-state centroid.
6. Phonons are uniformly distributed over the spatial volume of a geometric element.
7. Two methods are presented for determining the probability that any particular event contained within the interaction table will be allowed to proceed at

any instant of time. The first method, herein called simply scattering model "A" assumes that each scattering iteration is infinitely long, and that all events have an equal probability of occurrence. In model A, the probability of whether a phonon participates in a scattering event is driven by the distance that the pseudo-state is above or below its equilibrium population, and the entire population of partner phonons available for each reactant state to interact with. The second method, herein called model "B", employs a relaxation time based probability adapted from the perturbation model [55]. Here the decaying phonon populations are distributed uniformly across all candidate scattering interactions and are then limited by the available population of phonon partners.

8. Phonons are considered to be the only heat carriers in the SPT model. Thus, the model is valid for simulating thermal transport in semiconductor and dielectric materials. While it is clearly understood that optical branch phonons participate in phonon-phonon scattering, indirectly playing a role in impeding thermal transport through interactions with high frequency acoustic modes, in this work they are neglected. Optical modes may be included within the proposed SPT model framework, but this effort is deferred to a future work.

9. Two methods for modeling isothermal boundary cells are employed. In Model A, each boundary is "self-scattered" at the start of each time step. In Model B, the boundary cells are reset to the local thermodynamic equilibrium.

3.4 Phonon Pseudo-State Definition

The definition of phonon pseudo-states lies at the heart of the SPT model. A phonon pseudo-state can be uniquely defined by its properties of wave vector and polarization. Each pseudo-state represents a discrete volume of the BZ. The first BZ consists of an angular space of extent 4π as well as a wave number space $[0, K_{max}]$, where K_{max} depends on the direction of the wave vector, $\mathbf{K}$ [9]. The discretization of the BZ leads to a finite number of pseudo-states. Details of the discretization are

discussed in § 3.5, but for now consider the discretization results in $N_{E_{octant}}$ elements in the first octant of the BZ.

The number of phonon pseudo-states, M, within the BZ is

$$M = N_{E_{octant}} \times N_p \times N_{octant} \quad . \tag{3.1}$$

where $N_{E_{octant}}$ is the number of elements in the first octant and N_p is the number of polarizations considered. For silicon, N_p=6 and includes the TAI, TAII, LA, T0I, T0II, and LO branches. The pseudo-states in the first octant can be extended to represent the entire first BZ by performing the necessary rotations using planes of symmetry as described in Chapter 2 § 2.2. The lattice dynamics eigenvalue problem described in Chapter 2 § 2.4.1 is solved at the centroid of each BZ element to determine the frequency of all N_p modes in the BZ element. Phonons are assumed to be uniformly distributed over the **K**-space of a pseudo-state with each phonon assigned to the pseudo-state polarization and having a frequency, and group velocity of the pseudo-state centroid. All phonons that are later populated into the pseudo state associated with a BZ element are assigned the frequency (and hence, energy) and group velocity of the BZ element centroid. Each BZ element has a unique wave vector and a polarization-dependent frequency for each pseudo-state, providing a full anisotropic model of the dispersion curves, group velocities, and density of states. The group velocity is determined using the same lattice dynamics eigenvalue problem solved at the face centers of the BZ element, and the results are employed to estimate the group velocity $\boldsymbol{\nu}_m$ of pseudo state m, having a wave vector $\mathbf{K}$ and polarization p using a second order central finite difference model to the gradient resulting in

$$\boldsymbol{\nu}_m = \boldsymbol{\nu}_{\mathbf{K},p} = \nabla_{\mathbf{K}} \omega_{\mathbf{K},p} \quad . \tag{3.2}$$

Each pseudo state (consisting of a unique wave vector and polarization) may have a unique group velocity.

3.5 BZ Discretization

The BZ discretization is directly related to the pseudo-state definition. Therefore, it is an important aspect of the model.

Several works [9, 55] discretize the anisotropic BZ in their finite volume models of phonon transport. They use a methodology of dividing the angular space into $N_\theta \times N_\phi$ control angles each of extent $\Delta\Omega_i$, where Ω is the 4π solid angle, and θ and ϕ are the polar and azimuthal angles, respectively. The wave number space is discretized into bands of extent ΔK_j. This discretization results in elements that have unequal volumes.

For electron transport modeling both structured and unstructured BZ discretizations have been utilized. Structured meshes consist of uniform volume hexahedral elements. Unstructured meshes consist of uniform volume tetrahedral elements. Both have their advantages and disadvantages.

The BZ discretization currently used in the SPT model utilizes a structured hexehedral mesh, however the SPT model is not limited to utilizing this discretization.

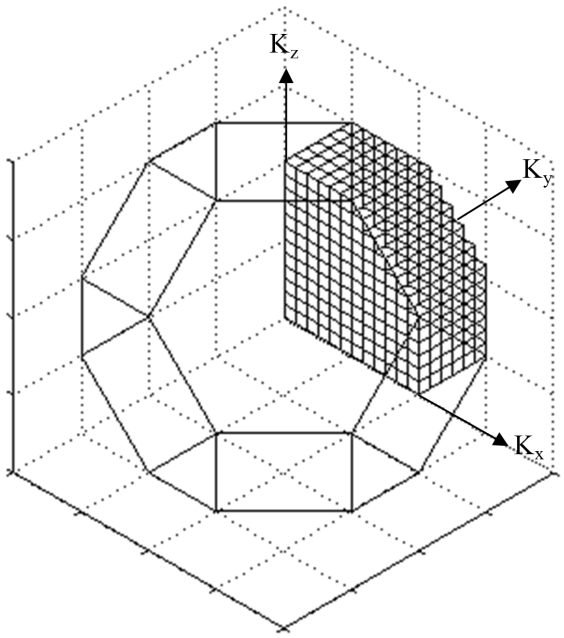

Figure 3.2 A typical structured discretization of the first octant of the BZ used in the pseudo-state definition.

In contrast to Fig. 3.2, the BZ shown previously in Fig. 2.5 has $1/48^{th}$ symmetry. One forty-eigth of the BZ is known as the irreducible wedge. Any point within the BZ can be represented by an equivalent point in the irreducible wedge. When using an unstructured mesh it is possible to mesh the irreducible wedge and use the appropriate reflections and permutations to expand the mesh throughout the BZ. In using a structured mesh it is convenient to utilize the first octant of the BZ ($1/8^{th}$ symmetry), which has been done in this work. The first octant wave number space is discretized in the x, y, and z directions into an equal number of ΔK bins. This generates a cube of hexahedral elements. Then, a check is performed to determine whether or not the element is fully within the BZ. Any element outside the BZ is not utilized in the pseudo-state definition. A structured mesh consisting of equal volume hexahedral elements is utilized to discretize the first octant of the BZ as shown in Fig. 3.2. For this work, a $12 \times 12 \times 12$ BZ element mesh in the first octant is utilized for many results. Additional mesh discretizations are demonstrated. For a $12 \times 12 \times 12$ BZ element mesh in the first octant approximately one-half of the 1,728 hexahedral

elements lie within the first BZ. This equates to approximately 41,000 pseudo-states within the entire BZ.

3.6 Spatial Discretization

Consider a homogeneous semiconductor material with isothermal boundaries at the X_{min} and X_{max} domain surfaces and periodic adiabatic boundaries at the Y_{min}, Y_{max}, Z_{min}, and Z_{max} domain surfaces, as shown in Fig. 3.3.

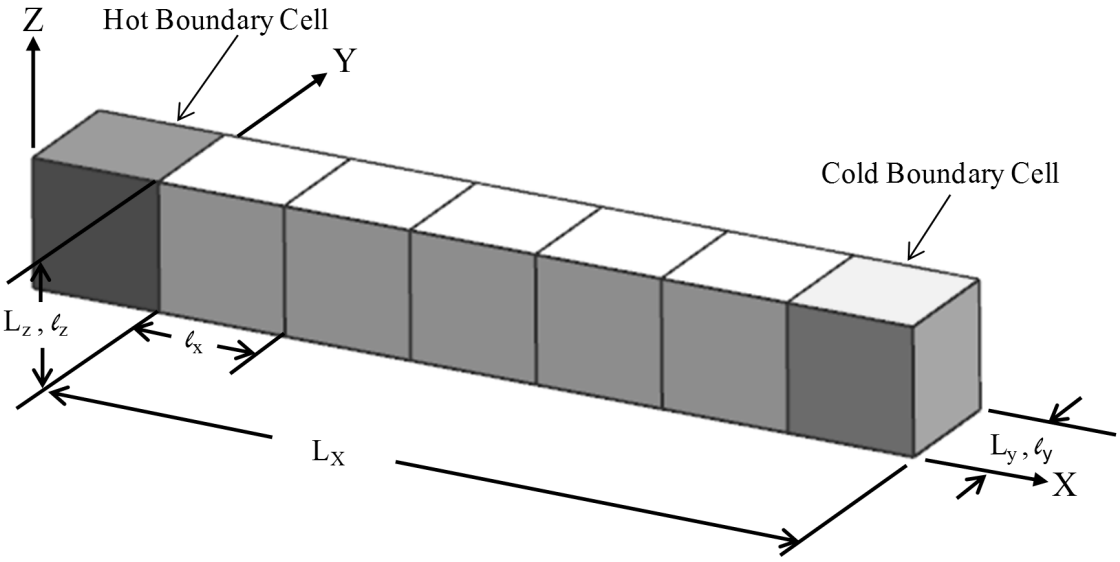

Figure 3.3 A typical domain discretization used in the SPT model.

The material is discretized into a three-dimensional computational domain consisting of C rectilinear cells. Each cell, c, contains the full population of $N_{c,m}$ phonons in each pseudo-state, m, for the represented volume in reciprocal space.

$$N_{\mathbf{m}}=V_{\mathbf{c}}n_m\frac{\partial\mathbf{K}}{(2\pi)^3} \quad , \tag{3.3}$$

where $V_{\mathbf{c}}$ is the cell volume. A local state vector, $\{LSV\}_c$ of length M is defined for each geometric cell, $1 \leq c \leq C$, in the domain as

$$\{LSV\}^c_{\mathbf{m}} = \left\{ \begin{array}{c} N_{\mathbf{1}} \\ N_{\mathbf{2}} \\ \vdots \\ N_{\mathbf{M}} \end{array} \right\} \quad , \tag{3.4}$$

where the phonon population, N^c_m, is the population of phonons of pseudo-state m, $1 \leq m \leq M$ contained in cell c. The phonon populations associated with a given pseudo-state are assumed to be uniformly distributed across the volume of each geometric cell. It is also noted that unlike MC models, scaling factors are not utilized. Therefore, each geometric volume contains the actual number of phonons specified by Eq. (3.3), evaluated at the cell's specified initial condition temperature distribution. For reference it is noted that the number of phonons present in any simulation is quite large. As an example, a 100 nm cubic cell at 500 K contains approximately 9×10^7 phonons spread across approximately $41,000$ pseudo-states for a $12 \times 12 \times 12$ BZ discretization.

3.7 Preprocessing

The material properties associated with each pseudo-state are pre-computed and stored in a data object. Each pseudo-state inherits a unique wave vector, polarization, number density, and group velocity. As the number of hexahedral elements used to model the pseudo-states increases, the **K**-space volume associated with each pseudo-state decreases. Following creation of the pseudo-states, the table of permissible interactions (which are pre-computed to satisfy energy and momentum) is created and stored as three vectors of integers, corresponding to the pseudo-states participating in each reaction. The pseudo-state data and interaction table are computed once and stored for subsequent use. After initialization, the SPT model proceeds sequentially through a series of time steps, from the initial condition until a steady state

is achieved. Each time step is divided into three distinct phases: drift, balance, and scattering.

3.8 Phonon Pseudo-State Drift

The drift phase is considered to be from time step τ to time step $\tau + 1/2$, while the scattering phase occurs from time step $\tau + 1/2$ to time step $\tau + 1$. The spatially uniformly distributed population of phonons associated with each pseudo-state in each cell are allowed to drift in a probabilistic manner. The computational time step, Δt, is limited by the cell size and the group velocity associated with the pseudo-states. In order to avoid ballistic jump over several cells, the following conservative time-step limit is enforced

$$\Delta t = \frac{\ell_{min}}{\boldsymbol{\nu}_{m,max}} \quad , \tag{3.5}$$

where ℓ_{min} is the minimum cell length and $\boldsymbol{\nu}_{m,max}$ is the maximum group speed in the x,y, and z directions for all pseudo-states [13]. During the drift phase pseudo-states drift linearly at their respective group velocities (using the mean values associated with each pseudo-state) for the prescribed time step. A general pseudo-state drift scheme along with three distinct boundary conditions (isothermal, periodic and adiabatic specular/diffuse) is briefly described.

Consider the two-dimensional geometric cell, c, of size ℓ_x by ℓ_y as shown in Fig. 3.4, having eight neighbors as indicated.

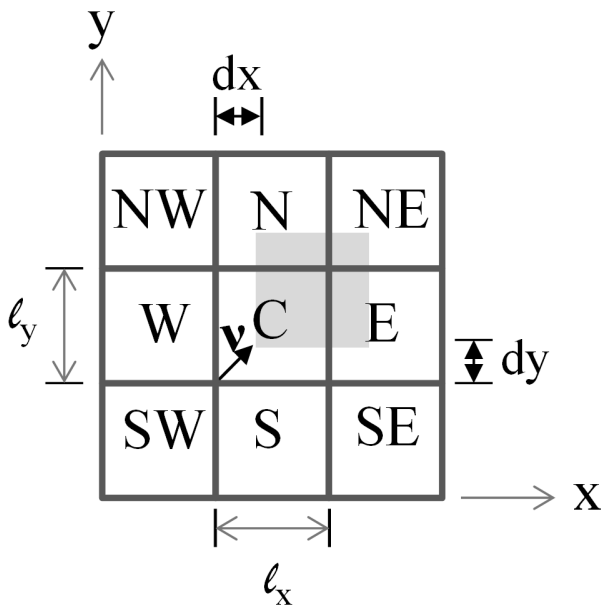

Figure 3.4 A depiction of the interior cell drift scheme for a given pseudo-state.

This cell contains a uniformly distributed population of phonons in each pseudo-state $1 \leq m \leq M$. Consider one particular pseudo-state, m, whose population is initially uniformly distributed across the volume of the cell, c, and moving with a group velocity, $\boldsymbol{\nu}_m$. After a small interval of time, Δt, the uniform population of phonons will drift as shown by the shaded area in the Fig. 3.4. The probabilities that the phonon population will drift into neighboring cells are given by:

$$\begin{aligned}
&P_{EAST} = dy(\ell_x - dx)/(\ell_x \ell_y) \\
&P_{NORTH} = dx(\ell_y - dy)/(\ell_x \ell_y) \\
&P_{NORTHEAST} = (dxdy)/(\ell_x \ell_y) \\
&P_{NORTHWEST} = 0 \\
&P_{WEST} = 0 \\
&P_{SOUTHWEST} = 0 \\
&P_{SOUTH} = 0 \\
&P_{SOUTHEAST} = 0
\end{aligned} \quad , \tag{3.6}$$

where dx equals $\boldsymbol{\nu}_{m,x}\ \Delta t$ and dy equals $\boldsymbol{\nu}_{m,y}\ \Delta t$. The probability that the phonons will remain in the center cell, c, is given as

$$P_C = (\ell_x - dx)(\ell_y - dy)/(\ell_x \ell_y) \quad . \tag{3.7}$$

A drift state vector, DSV, of length M is constructed for each cell, c, in the domain. The DSV is used to store pseudo-state populations as they drift. Let us denote the DSV's using an object-oriented matrix notation. Thus, we can say that

$$Cell\{c\}.DSV[Neighbor][m] = P_{Neighbor} * Cell\{c\}.LSV[m] \quad , \tag{3.8}$$

for $1 \leq Neighbor \leq 9$ (in two-dimensions) and $1 \leq m \leq M$, noting that $Neighbor$ =9 represents the DSV for the current cell since some of the pseudo-state populations will not drift out of the current cell. At the end of the drift phase, the LSV for each cell is empty as the entire population of each pseudo-state has been distributed to one of the DSV's associated with the cell c. This formulation is significant, in that any one cell, c, contains all information needed to populate its drift state vectors for all neighbors, without communication to any other cell in the domain. Drift calculations can be completely conducted in parallel.

3.9 Boundary Conditions

3.9.1 Isothermal Boundary Drift. An isothermal process is a thermodynamic process in which the temperature of the system remains constant. Similarly, an isothermal boundary condition is a constant temperature boundary condition. The isothermal boundary condition is implemented by resetting the LSV's of the isothermal cells to a pseudo-state population corresponding to the Bose-Einstein distribution at a prescribed boundary temperature at the beginning of each computational time step. During the drift phase of the computational time step the pseudo-state phonon populations of the isothermal cells are allowed to drift into the cells within the computational domain that border the isothermal cells, just as interior cells are allowed to

drift. Figure 3.5 depicts a 2-D depiction of a pseudo-state drifting from an isothermal boundary cell into the domain.

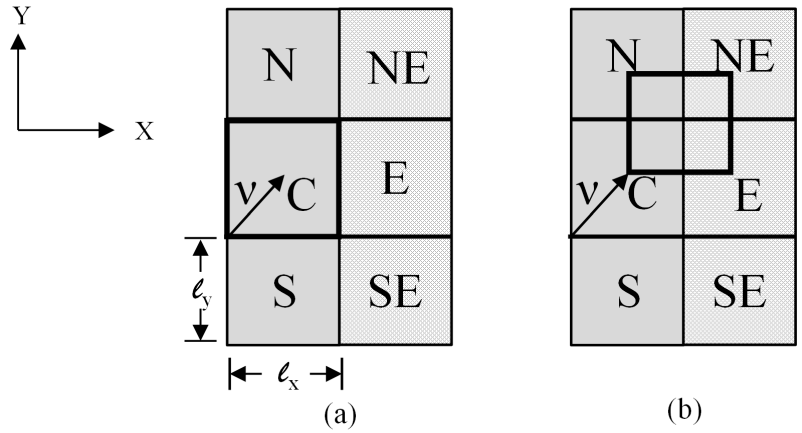

Figure 3.5 A depiction of the isothermal cell drift scheme for a given pseudo-state.

However, after the drift phase is completed, we discard all phonons entering the boundary from its neighbors, and restore it to its pre-drift condition. For the case of a one-dimensional isothermal boundary cell, we have:

$$\begin{aligned} Cell\{b\}.LSV[m] &= Cell\{b\}.DSV[CENTER][m] + Cell\{b\}.DSV[EAST][m] + \\ & \quad Cell\{b\}.DSV[WEST][m] \quad , \end{aligned} \tag{3.9}$$

for all boundary cells, b, and all pseudo-states, $1 \leq m \leq M$.

3.9.2 Periodic Boundary Condition. A periodic boundary condition is used to simulate a direction having infinite extent. This is achieved by assuring that there is no net loss of energy in the specified direction. So, for a given direction, the flux leaving one extreme boundary will immediately be replaced back into the domain at the opposite extreme boundary. When a pseudo-state drifts within a cell that borders a periodic boundary, some portion of the pseudo-state population may encounter the periodic boundary. The portion of the pseudo-state population that would normally leave the cell had the periodic boundary not been present is reintroduced back into the

cell, in the same pseudo-state. Since all neighbors are stored as indices to other cell numbers, the periodic boundary condition is readily achieved by a simple definition of "neighbor."

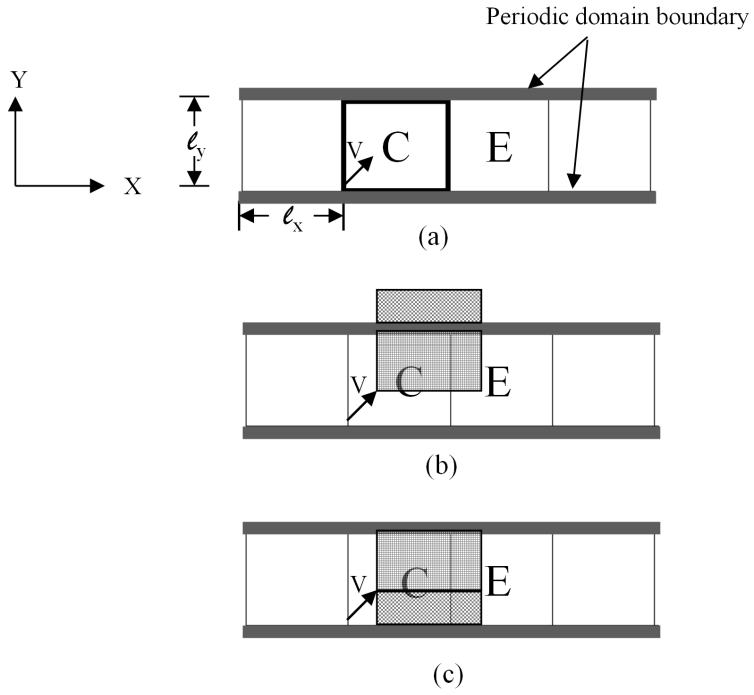

Figure 3.6 A depiction of the periodic boundary condition.

Consider Fig. 3.6 consisting of a one-dimensional domain such that the only significant cells are, $WEST$, $CENTER$, and $EAST$. All cells above and below the centerline are considered to be periodic boundary conditions. For each interior cell, c, we can define its periodic boundary neighbors as:

$$\begin{aligned} &Cell\{c\}.CENTER = Cell\{c\}.NORTH = Cell\{c\}.SOUTH = c \\ &Cell\{c\}.EAST = Cell\{c\}.NORTHEAST = Cell\{c\}.SOUTHEAST = c+1 \\ &Cell\{c\}.WEST = Cell\{c\}.NORTHWEST = Cell\{c\}.SOUTHWEST = c-1 \end{aligned} \quad , \tag{3.10}$$

Thus, implementation of periodic boundary conditions becomes trivial and they may be balanced the same as interior cells.

3.9.3 Adiabatic Specular/Diffuse Boundary Condition. An adiabatic process is a thermodynamic process in which the net heat transfer is zero. Thus, at an adiabatic boundary the heat flux is zero. When a pseudo-state drifts within a cell that borders an adiabatic boundary some portion of the pseudo-state population may interact with the adiabatic boundary. The SPT model allows the specularity of an adiabatic boundary to range from completely specular to completely diffuse. Adiabatic boundary scattering is an elastic process, thus it only effects the direction at which the pseudo-state travels.

Consider a pseudo-state, m, in a cell, c, that borders a completely specular domain. During drift, if a portion of the population interacts with the specular domain, that portion of the pseudo-state, m, will be reflected such that the angle of incidence is equal to the angle of reflection, resulting in a new pseudo-state, m', as shown in Fig. 3.7.

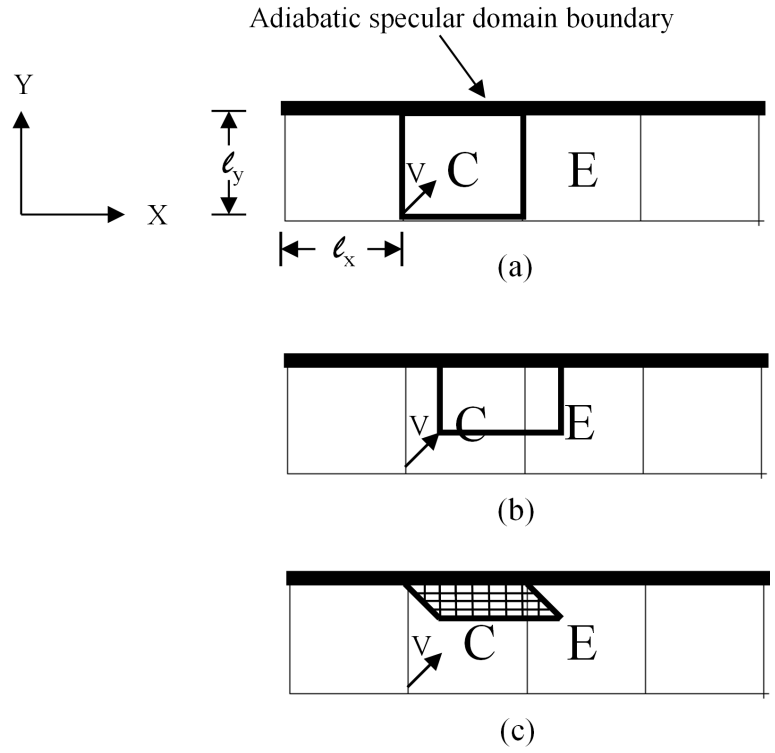

Figure 3.7 A depiction of the specular boundary condition.

Therefore, the LSV will lose a portion of the phonon population of pseudo-state m and will gain that portion in pseudo-state m', thus conserving energy. Pseudo-state m' has the same frequency and wave number as pseudo-state m, but a different group velocity direction.

During drift, if a portion of the population interacts with a diffuse domain, that portion of the pseudo-state m will be reflected such that the outgoing pseudo-states group velocity direction is independent of the incoming group velocity direction, while conserving energy. This is achieved by uniformly distributing the reflected population of m to all pseudo-states m' that have the same frequencies, polarizations, and normal velocity components to the diffuse surface of opposite sign. Similarly, the LSV will lose a portion of its population of pseudo-state m and will gain a portion in the resulting m' pseudo-states.

When the boundary specularity is between fully specular and fully diffuse, both drift mechanisms previously described will be invoked. Thus, some portion of the interacting pseudo-states population will be specularly reflected and the remaining portion will be diffusely reflected. The SPT model permits any knowledge of the surface properties to be used in determining the appropriate specular or diffuse reflection probabilities.

3.9.4 Interfacial Boundary Condition. Phonon transport can be quite different even in materials having similar crystal structures. When considering phonon transport across interfaces of different materials such as in superlattices or nanocomposites it is necessary to have an interfacial boundary condition model that can account for various phenomena that affect phonon transport across interfaces, such as differences in phonon spectra. Interfacial transport models such as the acoustic mismatch model, diffuse mismatch model or a variation of either could be implemented in a similar manner to the boundary conditions previously described. A full description of the interfacial transport models within the SPT model are deffered to future work.

3.10 Phonon Pseudo-State Balance

Upon completion of the drift phase, a phonon balance is conducted upon all interior cells. Each cell may retain a fraction of its original LSV population, and may gain and lose phonons in each pseudo state from and to its neighbors.

3.10.1 Interior Cell Balance . In the case of a one-dimensional interior cell, this is easily expressed by:

$$\begin{aligned} Cell\{c\}.LSV[m] &= Cell\{c\}.DSV[CENTER][m] + Cell\{c-1\}.DSV[EAST][m] + \\ & \quad Cell\{c+1\}.DSV[WEST][m] \quad , \end{aligned} \tag{3.11}$$

for all interior cells, c, and all pseudo states, $1 \leq m \leq M$.

3.10.2 Isothermal Boundary Cell Balance. After the drift phase is completed, we discard all phonons entering the boundary from its neighbors, and restore it to it pre-drift condition. For the case of a one-dimensional isothermal boundary cell, we have:

$$\begin{aligned} Cell\{b\}.LSV[m] &= Cell\{b\}.DSV[CENTER][m] + Cell\{b\}.DSV[EAST][m] + \\ & \quad Cell\{b\}.DSV[WEST][m] \quad , \end{aligned} \tag{3.12}$$

for all boundary cells, b, and all pseudo states, $1 \leq m \leq M$. The balance phase requires communication between neighboring cells. In a parallelized computer implementation, the balance phase requires inter-processor communication.

3.11 Compution of Cell Energies

Upon completion of the balance phase, the energy of each cell can be computed from its LSV as

$$Cell\{c\}.U = [N_1, N_2, \ldots, n_m, \ldots N_M]_{1xM}^{\tau+1/2} \left\{ \begin{array}{c} \hbar\omega^1 \\ \hbar\omega^2 \\ \vdots \\ \hbar\omega^M \end{array} \right\}_{Mx1} \tag{3.13}$$

where $Cell\{c\}.U$ represents the energy contained in each cell, c, in the domain.

3.12 Compution of Energy Flux

Several aspects of the validation require consideration of the net energy flux across computational domain. The net energy flux, q_{net}, across the c^{th} cell, can be defined as the sum of the flux in a given direction for each pseudo-state within the cell, where the flux for a given pseudo-state m in the x, y, and z directions are defined respectively as

$$\begin{aligned} q_{m,x} &= \tfrac{Cell\{c\}.LSV[m]}{V_c}(\hbar\omega_m)\boldsymbol{\nu}_{m,x} \quad , \\ q_{m,y} &= \tfrac{Cell\{c\}.LSV[m]}{V_c}(\hbar\omega_m)\boldsymbol{\nu}_{m,y} \quad , \\ q_{m,z} &= \tfrac{Cell\{c\}.LSV[m]}{V_c}(\hbar\omega_m)\boldsymbol{\nu}_{m,z} \quad . \end{aligned} \tag{3.14}$$

The net energy flux can be used to determine when steady-state has been reached and additionally in the calculation of effective thermal conductivity by analogy to Fourier's law.

3.13 Compution of Equivalent Cell Temperatures

A local temperature for each cell, $Cell\{c\}.Temperature$, can be obtained by fitting the Bose-Einstein distribution with the assumption of local thermodynamic equilibrium. This is done numerically by using a bisection algorithm on the cell energy. First an LSV_{guess} is created as shown by Eq. (3.4) using an initial temper-

ature guess. From LSV_{guess}, the $Cell\{c\}.U_{guess}$is computed using Eq. (3.13). This energy is then compared to the actual energy of the cell, $Cell\{c\}.U$. If the cell energy is within a small tolerance, then the cell temperature is reported, otherwise a new temperature guess is made and the bisection algorithm continues to iterate until the cell temperature is determined.

3.14 Computation of Effective Thermal Conductivity

As mentioned is § 3.12, once steady-state has been reached, the effective thermal conductivity can be calculated by analogy to Fourier's law. A second order central finite difference approximation to the temperature gradient is utilized along with the net energy flux incorporating Fourier's law. For a 1-D case, the effective conductivity is computed as

$$k = 2(q_{net,x})\frac{\ell_x}{Cell\{c-1\}.Temperature - Cell\{c+1\}.Temperature} \ . \qquad (3.15)$$

The SPT model is fully anisotropic, so for a 3-D domain it is possible to calculate conductivity tensor.

3.15 Three-Phonon Scattering

Recently there has been significant discussion pertaining to the concept of phonon engineering. Additionally there have been considerable efforts to modeling thermal transport in submicron semiconductor materials with the goal of simulating thermal transport in micro- nanoscale semiconductor devices. However, the complex mechanisms of phonon transport, in particular phonon-phonon interactions, are not fully understood. Detailed information regarding phonon-phonon interactions cannot be obtained experimentally. Theoretical studies for the most part have used approximations and fitting parameters that overshadow the intricacies of intrinsic scattering [56]. An improved understanding of phonon-phonon interactions is of critical importance to advance the field of micro- nanoscale thermal transport.

The Monte Carlo (MC) technique, applied to solving the BTE numerically, has been used over the past years to simulate conduction at submicron length scales [10, 12–15]. Even with rather crude approximations related to phonon-phonon scattering, the use of isotropic dispersion, and the inherent issues associated with stochastic methods that involve pseudo-random number generation, the MC technique has been shown to be quite promising. Researchers have shown the capability of MC technique to predict thermal transport in both the diffuse and ballistic regimes as well as bulk and thin film thermal conductivities that compare well with experimental data [10, 12–15]. Although, since Mazumder and Majumdar [12] presented the first comprehensive MC research, relatively little progress in actually advancing the ability to better model the intricate physics of phonon transport has been made.

Phonon-phonon interactions are due to third and higher order terms in the lattice potential energy. As a result, a phonon of a particular wave vector and polarization will decay into other phonons after a finite amount of time [57]. Phonon-phonon scattering involving four or more phonons is important only at temperatures above the Debye temperature [17]. Therefore, most discussions of phonon-phonon scattering are limited to three-phonon scattering.

3.15.1 Three-Phonon Scattering Processes. Three-phonon processes arise due to the anharmonic nature of the interatomic potential energy. There are two type of three-phonon processes, normal and Umklapp. These processes are governed by the conservation laws of energy and pseudo-momentum. There are two distinct ways in which a phonon may scatter in a three-phonon interaction. Type I interactions consist of two phonons combining and resulting in a third phonon. Type II interactions consist of a single phonon decaying into two phonons.

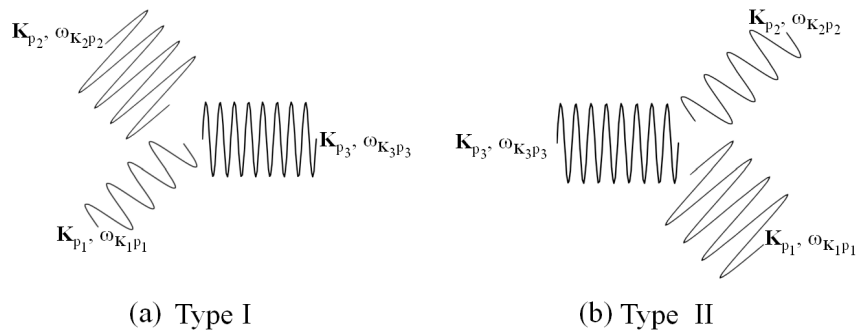

Figure 3.8 Type I and Type II three-phonon interaction processes.

The Type I three-phonon scattering interaction is described in terms of the participating pseudo-states as

$$m_1 + m_2 = m_3 \quad . \tag{3.16}$$

For a three-phonon interaction, the conservation of energy is given as

$$\omega_1 + \omega_2 = \omega_3 \quad . \tag{3.17}$$

The conservation of pseudo-momentum for normal processes is given as

$$\mathbf{K}_1 + \mathbf{K}_2 = \mathbf{K}_3 \quad . \tag{3.18}$$

The conservation of pseudo-momentum for Umklapp processes is given as

$$\mathbf{K}_1 + \mathbf{K}_2 = \mathbf{K}_3 + \mathbf{G} \quad . \tag{3.19}$$

where $\mathbf{G}$ is the reciprocal lattice vector as described in Chapter 2 § 2.1.

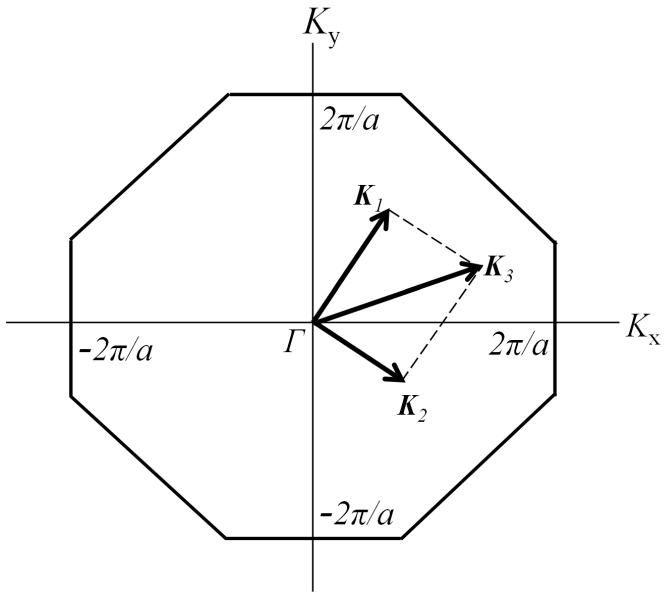

Figure 3.9 A three-phonon normal scattering process in the BZ.

In Fig. 3.9, the wave vectors $\mathbf{K}_1$ and $\mathbf{K}_2$ represent the momenta of the incoming phonons that when added result in a phonon with momentum $\mathbf{K}_3$ residing in the first BZ. Since normal processes conserve both energy and momentum they do not pose any resistance to heat transfer. Umklapp processes involve two phonons interacting resulting in a third phonon in which $\mathbf{G}$ from Eq. (3.19) does not equal zero. Figure 3.10 depicts an Umklapp process where the boundary of the BZ is $2\pi/a$.

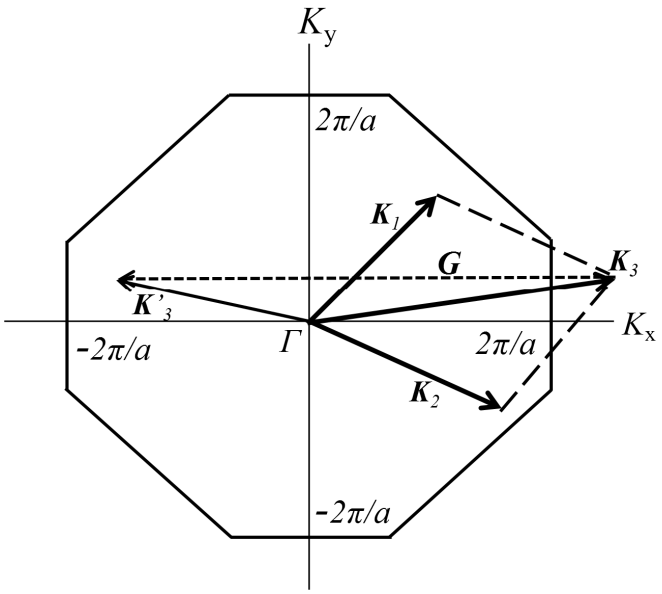

Figure 3.10 A three-phonon Umklapp scattering process in the BZ.

It is apparent that the vector sum of $\mathbf{K}_1$ and $\mathbf{K}_2$ extends beyond the boundary of the first BZ. Since any point outside the first BZ is physically equivalent to a point within the first BZ, $\mathbf{K}_3$ can be replaced by a vector within the first BZ by adding to it a reciprocal lattice vector $\mathbf{G}$. Since Umklapp processes do not conserve momentum they directly pose resistance to heat transfer. Umklapp processes are highly temperature dependent and are not active at very low temperatures where boundary and isotope scattering dominate thermal transport. Normal and Umklapp processes may both progress as forward and reverse reactions as shown in Eqs. (3.18) and (3.19).

3.15.2 Review of Monte Carlo Approach to Three-Phonon Scattering. One of the most complicated aspects of phonon transport is phonon-phonon scattering. Attempts at capturing this phenomenon utilizing the MC technique are far from sufficient. Mazumder and Majumdar [12] accounted for the acoustic phonons with an isotropic dispersion model. Scattering probabilities between acoustic modes were computed using a cumulative distribution function for the exponential distribution given as

$$P = 1 - e^{(-\lambda t)} \tag{3.20}$$

where λ represents the rate parameter. The rate parameter used to compute the scattering probabilities was based on heuristic expressions for relaxation times from Holland [5]. Since the selection rules associated with energy and pseudo-momentum conservation were not strictly followed during scattering, an ad-hoc method of energy conservation was adopted. It involved phonon addition/deletion within computational cells post-scatter to bring the resulting phonon distribution energy to its pre-scattering level. This scattering methodology did not obey detailed balance. Chen *et al.* [14] utilized similar scattering probabilities to that of Mazumder and Majumdar [12], but they developed a genetic algorithm that enforced energy conservation during phonon-phonon scattering. Understanding the importance of a phonon-phonon scattering model obeying detailed balance and being self consistent, Lacroix *et al.* [13] modified the method or phonon addition/deletion post-scatter by inclusion of a new distribution function that guaranteed energy conservation during phonon-phonon scattering. Recently, Mittal and Mazumder [10] included the optical branch in their isotropic dispersion model. They used a combination of Holland's [5] relaxation time expressions for normal processes and Han and Klemens [58] relaxation time expressions for Umklapp processes. The inclusion of optical phonons offered insight into their importance and role in phonon-phonon scattering.

From this brief review it is apparent that a significant amount of fundamental work is needed to further understand phonon-phonon scattering. One reason that significant advances have not been made is the computational cost associated with the MC technique. For this reason, current MC algorithms require the use of scaling factors on phonon populations and isotropic dispersion assumptions. With this coarse of a representation of the phonon distributions, a rigorous implementation of phonon-phonon scattering obeying the selection rules associated with energy and pseudo-momentum conservation over the entire anisotropic Brillouin zone is hardly feasible.

3.15.3 Compution of Three-Phonon Scattering Events. Following the discretization of the BZ, an interaction table is computed and stored for subsequent

use. The approach used for creating the interaction list is a variation of those by Wang [9] and Pascual-Guiterrez *et al.* [55]. Multiple sample points are created within the elements of the discretized BZ and an exhaustive search is conducted computing all normal and Umklapp interactions following the energy and pseudo-momentum conservation selection rules. The three-phonon scattering model used herein similarly accounts for all frequency and wave vector combinations. To illustrate the three phonon scattering selection process, consider two pseudo-states m_1 and m_2 in the first octant of the BZ, shown as a two-dimensional slice in Fig. 3.11, participating in a Type I normal process.

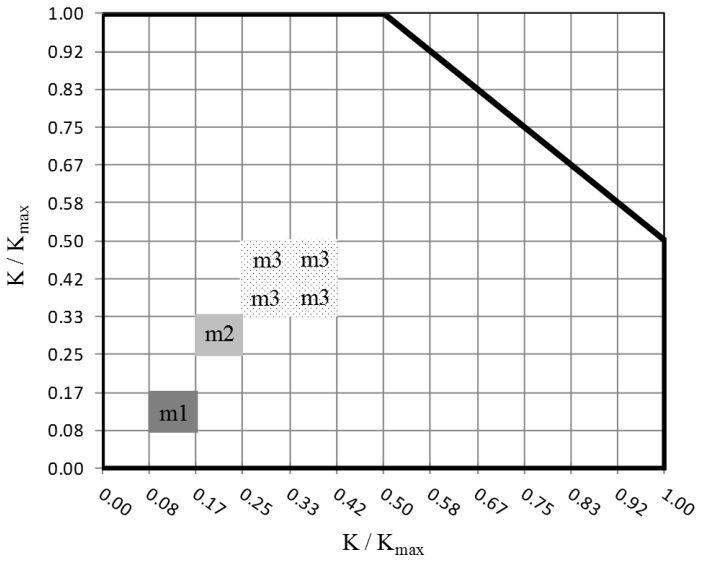

Figure 3.11 Momentum conservation of two pseudo-states during a Type I three-phonon normal scattering process.

The phonons occupying each reactant pseudo-state, m_1 and m_2, are assumed to be uniformly distributed over the **K**-space of the pseudo-state. When these phonon pseudo-momentum distributions are vectorially added together, they will result in a population of phonons distributed across 4 product states, m_3, (8, in the actual three-dimensional **K**-space) as shown in Fig. 3.11. These resultant populations are guaranteed to conserve pseudo-momentum (with the addition of a reciprocal lattice

vector for Umklapp processes). Every BZ element is compared to every other BZ element in the entire BZ, including all 8 octants. Each pairing of two BZ elements will result in the original population of phonons from the reactant state being distributed across at most eight product states. Some of the product states resulting from a reactant pair may be normal processes, and some may be Umklapp processes. All eight product states, m_3, are known to conserve pseudo-momentum and must be checked for conservation of energy, for each polarization, p. The centroid frequencies of each element m_1, m_2, and m_3 are used to check for conservation of energy, and the energy imbalance is proportional to the frequency imbalance

$$\Delta\omega = \omega_{K_3,p_3} - (\omega_{K_1,p_1} + \omega_{K_2,p_2}) \quad . \tag{3.21}$$

An interaction is considered valid and added to the interaction list if the following frequency criteria is met

$$\frac{|\Delta\omega|}{\omega_{K_3,p_3}} < \omega_\varepsilon \quad . \tag{3.22}$$

For every pair of reactant pseudo-states, $m_1$and m_2, Eq. (3.22)is checked against the eight possible product pseudo-states, m_3. The selection of the energy conservation criteria, ω_ε, is a critical parameter in defining an acceptable interaction event. If ω_ε, is chosen to be too large of a value, then energy is only loosely conserved, and the interaction table will contain too many elements to effectively manage. Conversely, if ω_ε, is chosen to be too small, then energy may be conserved to a very tight tolerance, but a relatively small number of interactions may be permitted depending on the density of the BZ discretization. The selection rule for conservation of energy and pseudo-momentum is mentioned in numerous MC articles, but the influence of the selection rule is not typically a subject of robust investigation.

The SPT model assumes that the phonons in a pseudo-state are uniformly distributed across the **K** space of the state, but they are tracked with a single frequency to represent the mean energy content of the population. This approach permits the

SPT model to forgo the requirement of tracking positions of individual phonons, and instead model populations of phonons sharing similar characteristics.

3.15.4 Three-Phonon Scattering Model A. To introduce model A, assume that each pseudo-state is populated with some number of phonons, N_m. The energy, U, associated with this population of phonons can be computed from Eq. (3.13). The energy stored within a geometric volume of space can then be used to determine an equivalent temperature, by fitting the Bose-Einstein distribution with the assumption of local thermodynamic equilibrium. Given the equivalent temperature associated with the current phonon population distribution, the equilibrium population of phonons associated with each pseudo-state, N_m^* is computed. If the current phonon population is above its equilibrium population, then that pseudo-state is more likely to serve as a "donor" state, while if the current phonon population is below its equilibrium population, then that pseudo-state is more likely to serve as a "recipient" state. If the current population is at the equilibrium population, then it is equally probable to participate in any particular interaction as either a donor or a recipient. A simple linear cumulative distribution function (CDF), Fig. 3.12, illustrates the probability of pseudo-state m being a donor, P_m^d.

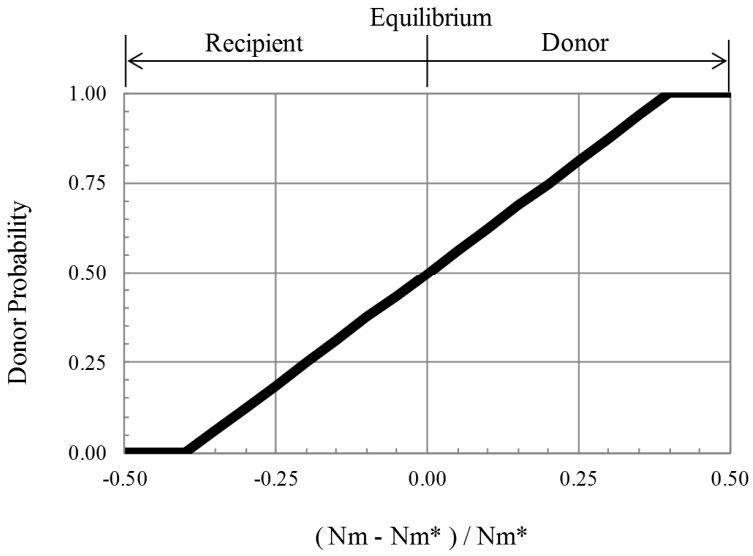

Figure 3.12 Linear cumulative distribution function.

While a more sophisticated CDF may be used, the linear CDF is computationally efficient, and is sufficient following many scattering iterations.

The equilibrium-limited probability that a Type I reaction will occur as a result of the distance from equilibrium, P_{eq}^{I}, is assigned to be

$$P_{eq}^{I} = (P_{m_1}^{d})(P_{m_2}^{d})(1 - P_{m_3}^{d}) \quad . \tag{3.23}$$

while the equilibrium-limited probability that a Type II reaction will occur as a result of the distance from equilibrium, P_{eq}^{II}, is assigned to be

$$P_{eq}^{II} = (1 - P_{m_1}^{d})(1 - P_{m_2}^{d})(P_{m_3}^{d}) \quad . \tag{3.24}$$

The interaction list is studied for every pseudo-state m. The number of possible Type I events for row i of the interaction table is limited by the lesser of the populations of pseudo-states m_1 and m_2:

$$e_i^{I} = min(N_{m_1}, N_{m_2}) \quad . \tag{3.25}$$

while the number of possible Type II events for row i of the interaction table is limited by the population of pseudo-state m_3.

$$e_i^{II} = N_{m_3} \quad . \tag{3.26}$$

The total number of events that each pseudo-state participates in, E_m, is the summation of Eqs. (3.25) and (3.26) over all rows of the interaction table given as

$$\begin{aligned} E_m^I &= \sum_{i=1}^{N_{Int}} e_i^I \quad , \\ E_m^{II} &= \sum_{i=1}^{N_{Int}} e_i^{II} \quad . \end{aligned} \tag{3.27}$$

The population-limited probability that a Type I reaction in row i of the interaction table will occur is taken to be dependent upon all potential partners that each pseudo-state m_1 and m_2 may interact with:

$$P_{pop-i}^I = min(\frac{e_i^I}{E_{m_1}^I}, \frac{e_i^I}{E_{m_2}^I}) \quad , \tag{3.28}$$

while the population-limited probability that a Type II reaction in row i of the interaction table will occur is taken to be

$$P_{pop-i}^{II} = (\frac{e_i^{II}}{E_{m_3}^{II}}) \quad . \tag{3.29}$$

After the interaction table has been evaluated in light of the current phonon populations, then the total probability that row i of the interaction table will occur is given by the product of the equilibrium-limited and population-limited probabilities:

$$\begin{aligned} P_{Total-i}^I &= (P_{pop-i}^I)(P_{eq}^I) \\ P_{Total-i}^{II} &= (P_{pop-i}^{II})(P_{eq}^{II}) \end{aligned} \quad . \tag{3.30}$$

The overall probabilities for each row i of the interaction table are applied to each event, and the initial phonon populations are redistributed to a new phonon population as a result of the scattering events. The entire process may then be repeated in an iterative fashion. For model A, three-phonon scattering is applied to all interior and isothermal boundary cells. For model B, three-phonon scattering is applied only to interior cells.

3.15.5 Three-Phonon Scattering Model B. Considering that all three-phonon interactions have been computed within the discretized BZ and stored in an interaction table, it is possible to adapt the time-dependent perturbation theory to compute individual transition rates for each event within the list [9, 55]. This is a viable method that may be incorporated into the SPT model, although at significant computational expense. A computationally less demanding approximation is employed here. Model B also begins with a known population of phonons N_m occupying each pseudo-state in the BZ. While model A used the concept of "donor probability" to determine whether a phonon population would be more or less likely to participate in any given interaction, and neglected the time dependence of the event, model B conversely considers the current mean lifetime of the phonon population relative to its relaxation time, and then determines the probability that the population will decay instantaneously at the current time. An empirical model, loosely based on the work of Pascual-Gutierrez *et al.* [55] is used to estimate the relaxation time for the acoustic modes of silicon as:

$$\tau_p = A_p \omega^{B_p} \quad . \tag{3.31}$$

A power law fit was applied to the relaxation time curves reported by Pascual-Gutierrez *et al.* [55].

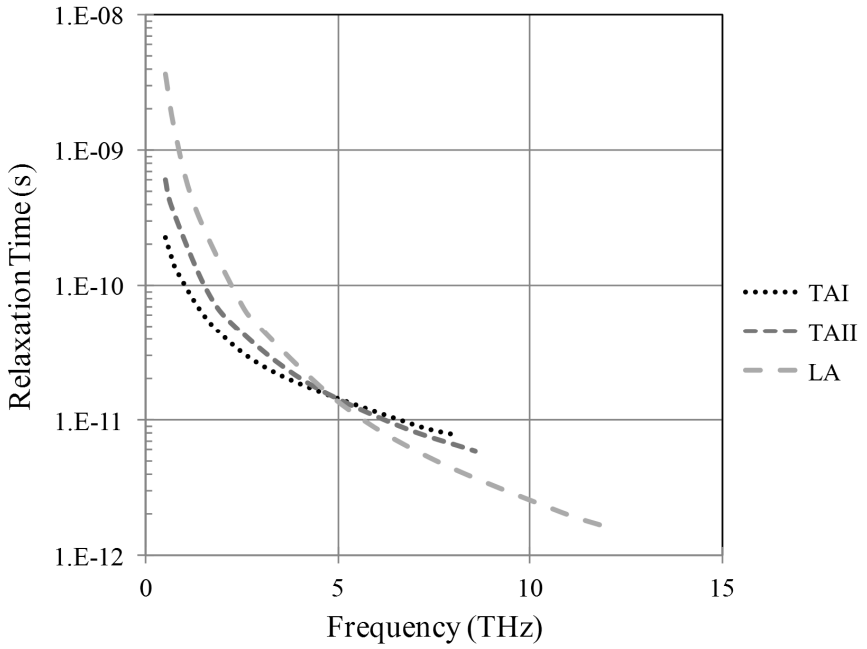

Figure 3.13 Power law fit to the relaxation times from [55] at 500K.

For mode TAI, A = 34021 and B = -1.202 . For mode TAII, A = 8E9 and B = -1.634, while for mode LA, $A = 1{\times}10^{20}$ and B = -2.431, with all units expressed in SI. The mean lifetime of the phonon populations of pseudo-state m is denoted as t_m, and is a weighted average of the lifetimes of all phonons in the pseudo-state m population, updated once each scattering iteration using a sequential estimation algorithm. Model B is used to estimate the fraction of the population of pseudo-state m that will decay at the current time:

$$P_m^{Decay} = 1 - e^{-(\frac{t_m}{3\tau_m})} \quad . \tag{3.32}$$

The number of phonons of pseudo-state m to scatter at the current time is taken to be

$$N_m^{Decay} = P_m^{Decay} N_m \quad . \tag{3.33}$$

while the remaining phonons of pseudo-state m persist in an unscattered state. The total number of rows, i, from the interaction table that engage pseudo-state m is

counted, and tallied as I_m. The decaying phonons from pseudo-state m are uniformly distributed over these I_m rows independent of the event populations e_i^I or e_i^{II} associated with these rows. If state m participates in interaction row i as a Type I reactant, then the number of scattered phonons of pseudo-state m is limited by the smaller of the available reactant populations given as

$$N_m^{I,Decay} = min(\frac{N_m^{Decay}}{I_m}, \frac{N_{m_2}^{Decay}}{I_{m_2}}) \times Limit \quad , \tag{3.34}$$

subject to the perturbation $Limit$ as the population approaches equilibrium, where

$$\begin{aligned} Limit \quad &= \quad (n_1 n_3 + n_2 n_3 - n_1 n_2) + & (3.35) \\ &\quad [-n_1(n_{0,2} - n_{0,3}) - n_2(n_{0,1} - n_{0,3}) + n_3(n_{0,1} + n_{0,2} + 1)] \quad , & (3.36) \end{aligned}$$

or $Limit = 1$ for populations far from equilibrium. If pseudo-state m participates in interaction row i as a Type II reactant, then the number of scattered phonons of pseudo-state m is given by

$$N_m^{II,Decay} = (\frac{N_m^{Decay}}{I_m}) \quad . \tag{3.37}$$

3.15.6 Pseudo-State Population Updating. During the creation of the interaction table, the centroid energy of the pseudo-states is approximately conserved, as noted by Eq. (3.22). The SPT model tracks large quantities of phonons, and small errors in energy will rapidly accumulate over multiple scattering iterations. When scattering events are computed, only whole phonons are permitted as reactants. However, the number of products is computed as a real number in order to achieve strict energy conservation. Effectively, this enforces the quantum effects of discrete events, but mitigates the error in assuming that all phonons within a pseudo-state exist at the centroid frequency, even though they are distributed across **K**-space within the

pseudo-state. For a Type I reaction, the number of products is given by

$$N^{I}_{Products} = \frac{(\omega_{K_1,p_1} + \omega_{K_2,p_2})}{\omega_{K_3,p_3}} N^{I}_{Reactants} \quad . \tag{3.38}$$

The reciprocal relation is used for Type II reactions as

$$N^{II}_{Products} = \frac{\omega_{K_3,p_3}}{(\omega_{K_1,p_1} + \omega_{K_2,p_2})} N^{II}_{Reactants} \quad . \tag{3.39}$$

The ratio of products to reactants is approximately unity.

As a result of scattering, the initial pseudo-state phonon populations are re-distributed to new pseudo-state phonon populations. This is performed for a given pseudo-state m as follows

$$N_M^{\tau+1} = N_M^{\tau+\frac{1}{2}} + \sum_{i=1}^{N_{Int}} (N_m^{I,Products,i} - N_m^{I,Reactants,i}) + (N_m^{II,Products,i} - N_m^{II,Reactants,i}) \quad , \tag{3.40}$$

for $1 \leq m \leq M$. The entire process is repeated in an iterative fashion, and the mean lifetime of each pseudo-state is updated based on the populations of phonons persisting in their unscattered state, the number of phonons destroyed at the current time, and the number of phonons created at the current time. The mean lifetimes are updated using a sequential estimator. The mean lifetime is given as

$$\begin{aligned} \bar{t}_M^{\tau+1} = & \tfrac{1}{N_M^{\tau+1}} \{ \bar{t}_M^{\tau+\frac{1}{2}} \times N_M^{\tau+\frac{1}{2}} + \\ & \sum_{i=1}^{N_{Int}} (N_m^{I,Products,i} \Delta t - N_m^{I,Reactants,i} \bar{t}_M^{\tau+\frac{1}{2}}) + \\ & \sum_{i=1}^{N_{Int}} (N_m^{II,Products,i} \Delta t - N_m^{II,Reactants,i} \bar{t}_M^{\tau+\frac{1}{2}}) \} \quad , \end{aligned} \tag{3.41}$$

for $1 \leq m \leq M$.

3.15.7 Isotope Scattering. Isotope scattering becomes important at temperatures below 200 K [55]. At these temperatures the phonon populations associated with high wave number pseudo-states are scarce, therefore the availability of partners

for Umklapp is limited. Thus, in addition to boundary scattering, isotope scattering influences phonon transport. The elastic isotope scattering events can be calculated in a similar manner as three-phonon scattering events, and tabulated in the pre-processing step of the SPT model. In this work, isotope scattering is not addressed.

CHAPTER 4

Preprocessing Results

Accuracy in thermal transport modeling starts at the level of material characterization. For the SPT model the current focus has been on crystalline semiconductor materials such as silicon and germanium. The isotropic assumption that has been assumed in many past studies is replaced by a fully anisotropic material description. The SPT model material characterization of silicon is performed as described in Chapter 2. The anisotropic BZ is discretized and a lattice dynamics model is utilized to extract wave vector and polarization dependent properties. Results are now presented that demonstrate the material characterization of silicon used in subsequent thermal transport results. Justification for the chosen BZ discretization is provided.

4.1 Brillouin Zone Discretization

In order to numerically model phonon transport it is necessary to discretize the BZ. A structured hexahedral mesh is utilized for the current work as shown in Fig. 3.2. The results described in this section pertain to the two different levels of refinement for the structured mesh, namely $12 \times 12 \times 12$ and $18 \times 18 \times 18$. These discretizations correspond to approximately 40,000 and 140,000 pseudo-states respectively. Figure

4.1 shows a comparison of the $12 \times 12 \times 12$ mesh discretization (a) with the $18 \times 18 \times 18$ discretization (b).

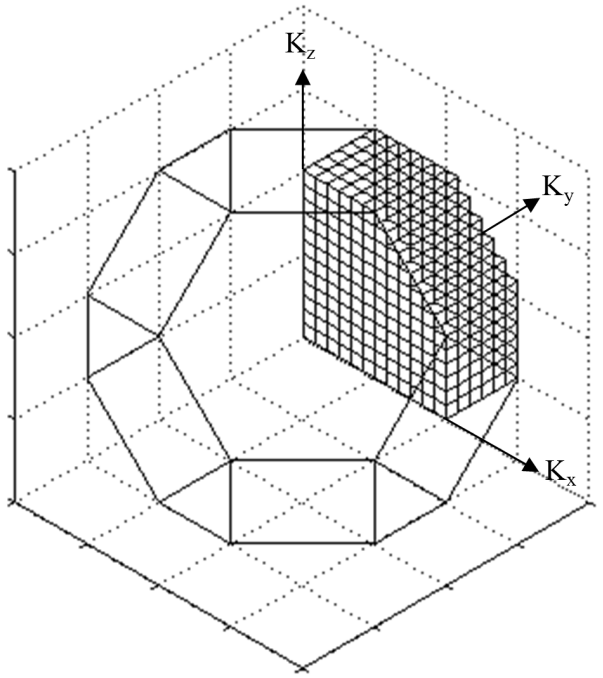

(a)

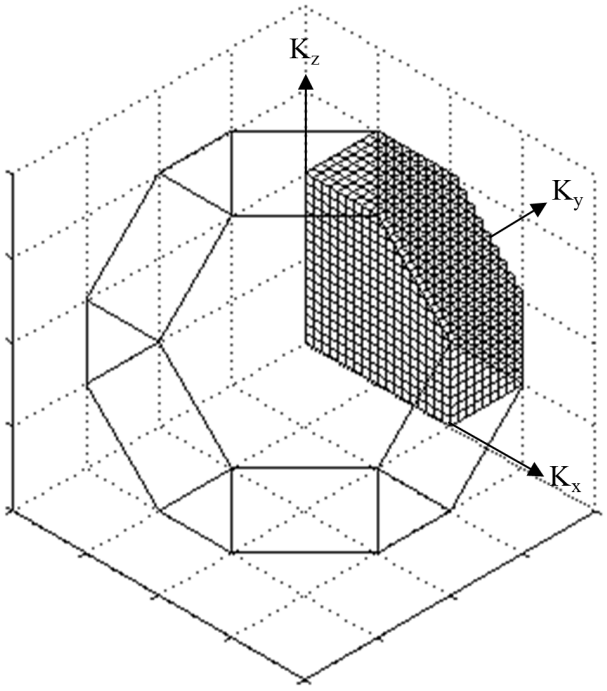

(b)

Figure 4.1 Comparison of two different BZ discretizations, $12 \times 12 \times 12$ (a) and $18 \times 18 \times 18$ (b).

4.2 Dispersion

Dispersion relations are useful to understand the relation between frequency and wave vector for the pseudo-states defined in Chapter 3 § 3.4, representing the anisotropic BZ. The dispersion relation distributions shown here are for acoustic and optical polarizations. These distributions include all wave vectors in the BZ.

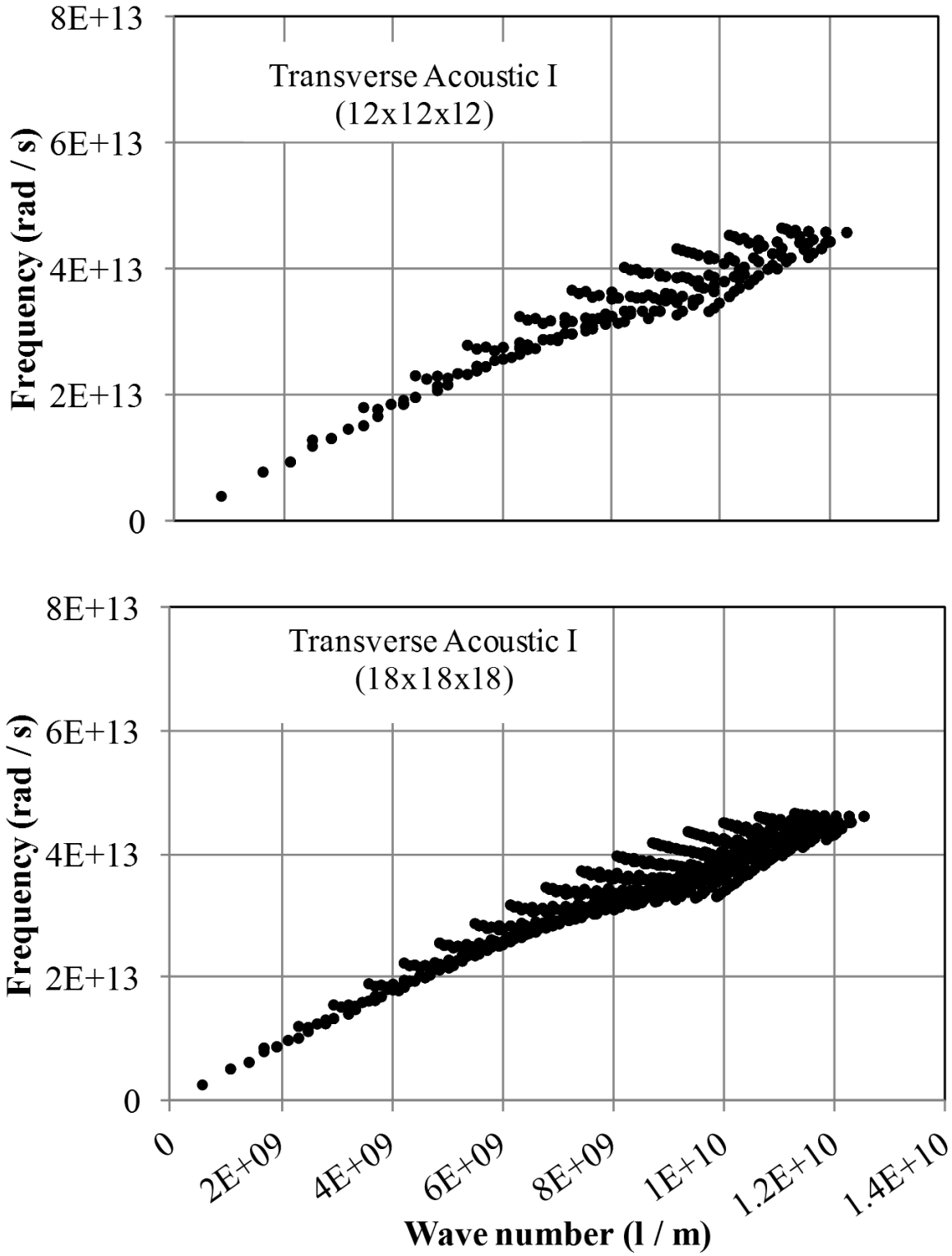

Figure 4.2 Comparison of the transverse acoustic I dispersion distributions for $12 \times 12 \times 12$ and $18 \times 18 \times 18$ BZ discretizations.

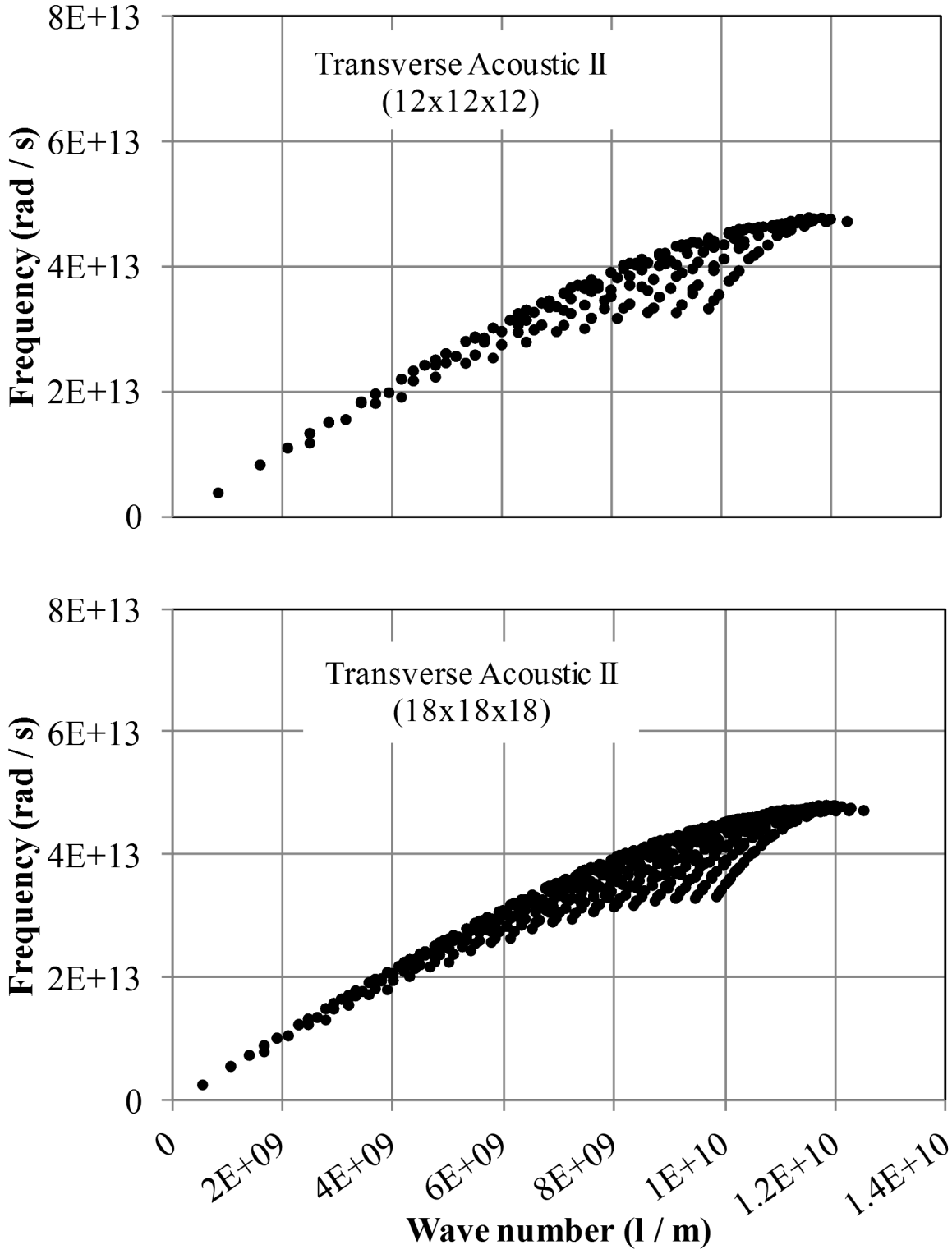

Figure 4.3 Comparison of the transverse acoustic II dispersion distributions for $12 \times 12 \times 12$ and $18 \times 18 \times 18$ BZ discretizations.

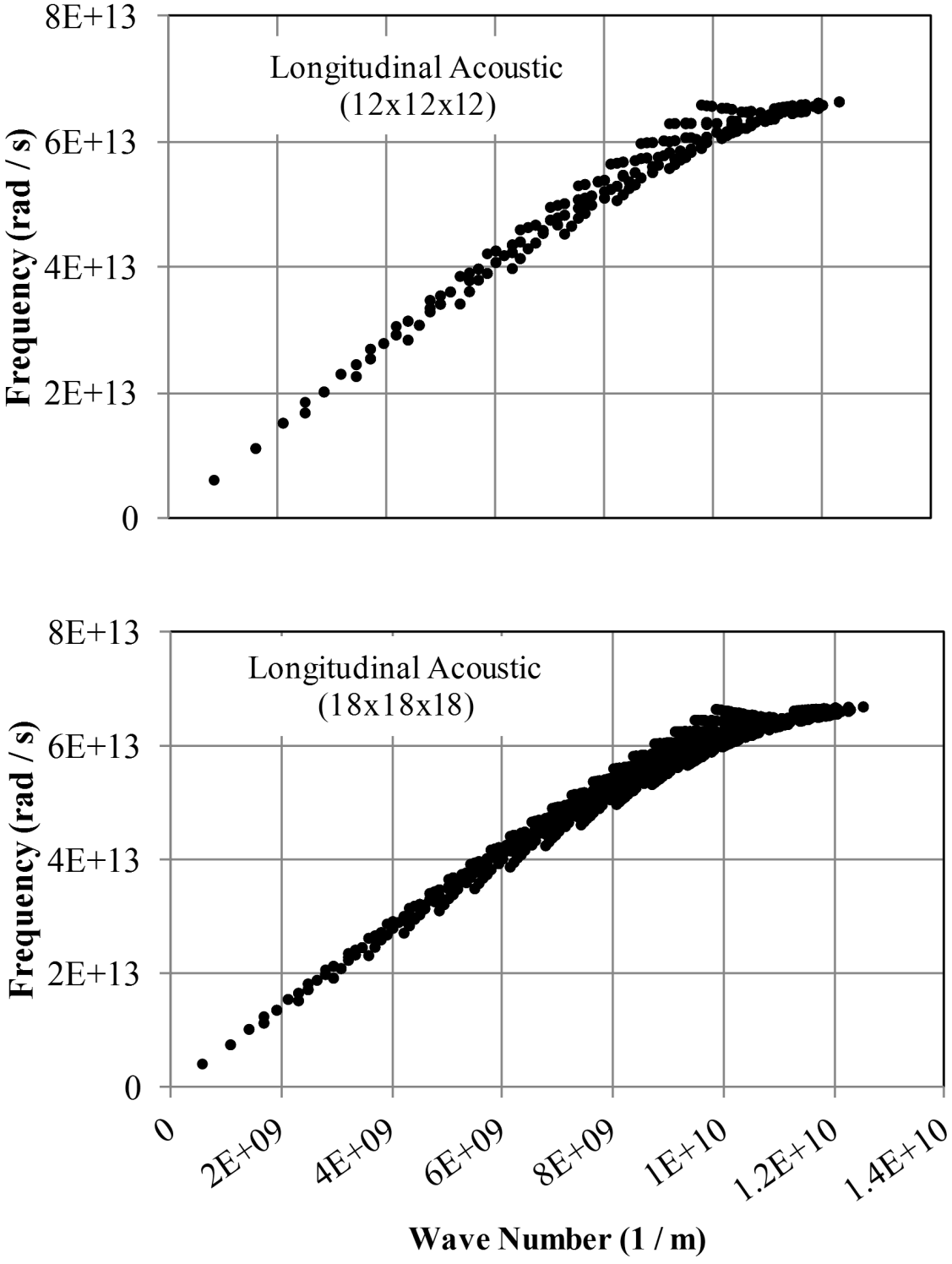

Figure 4.4 Comparison of the longitudinal acoustic dispersion distributions for $12 \times 12 \times 12$ and $18 \times 18 \times 18$ BZ discretizations.

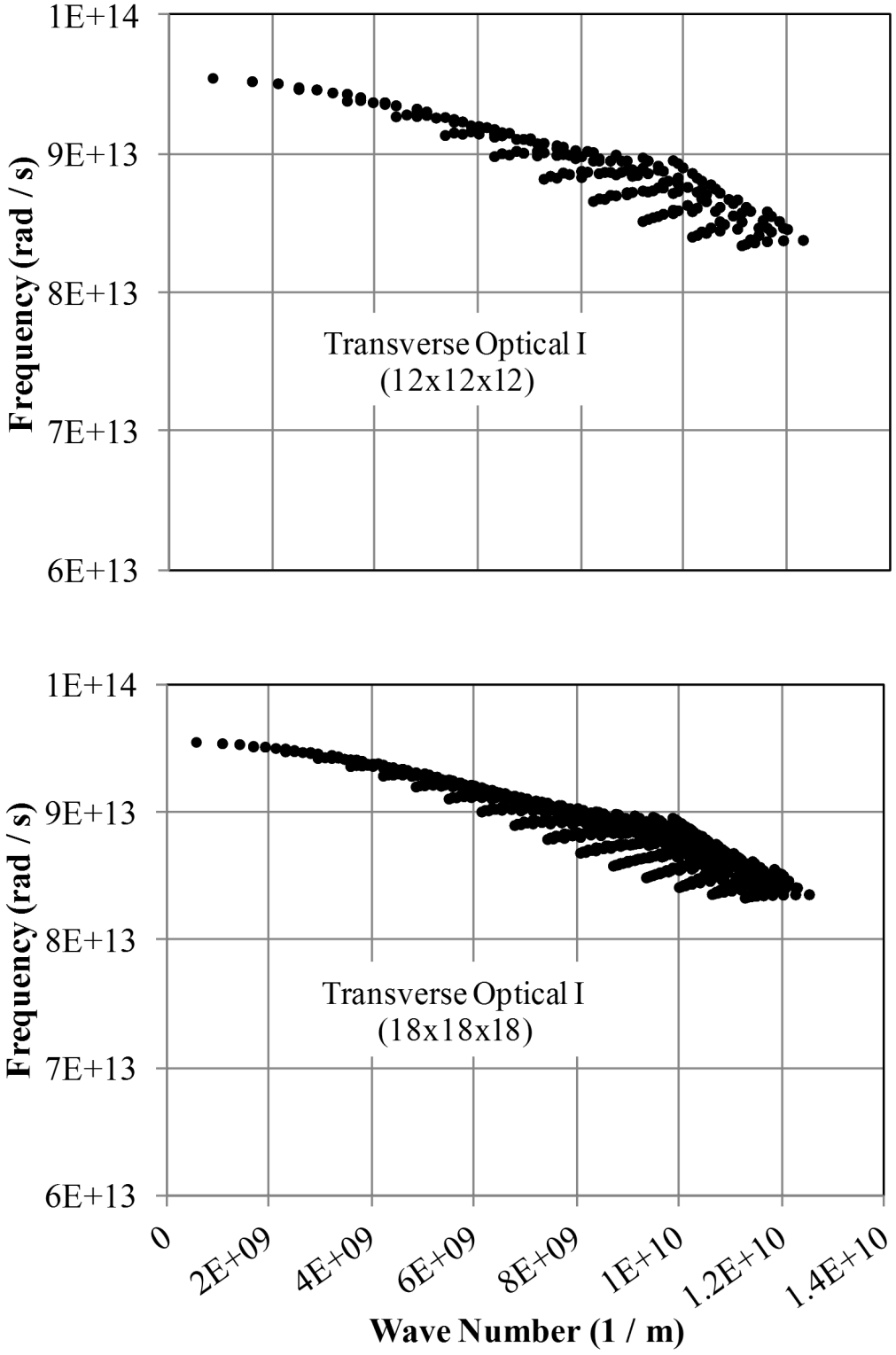

Figure 4.5 Comparison of the transverse optical I dispersion distributions for $12 \times 12 \times 12$ and $18 \times 18 \times 18$ BZ discretizations.

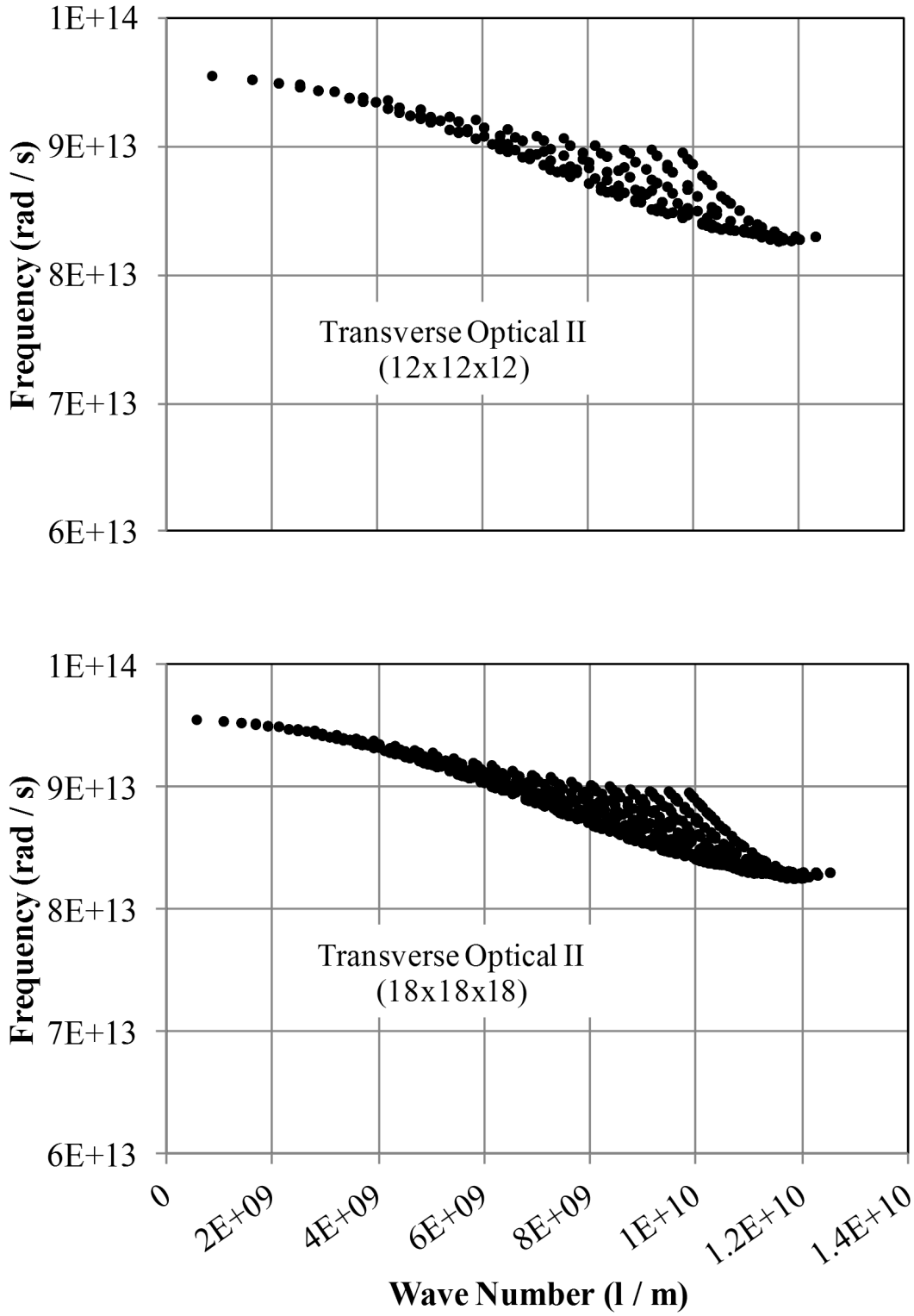

Figure 4.6 Comparison of the transverse optical II dispersion distributions for $12 \times 12 \times 12$ and $18 \times 18 \times 18$ BZ discretizations.

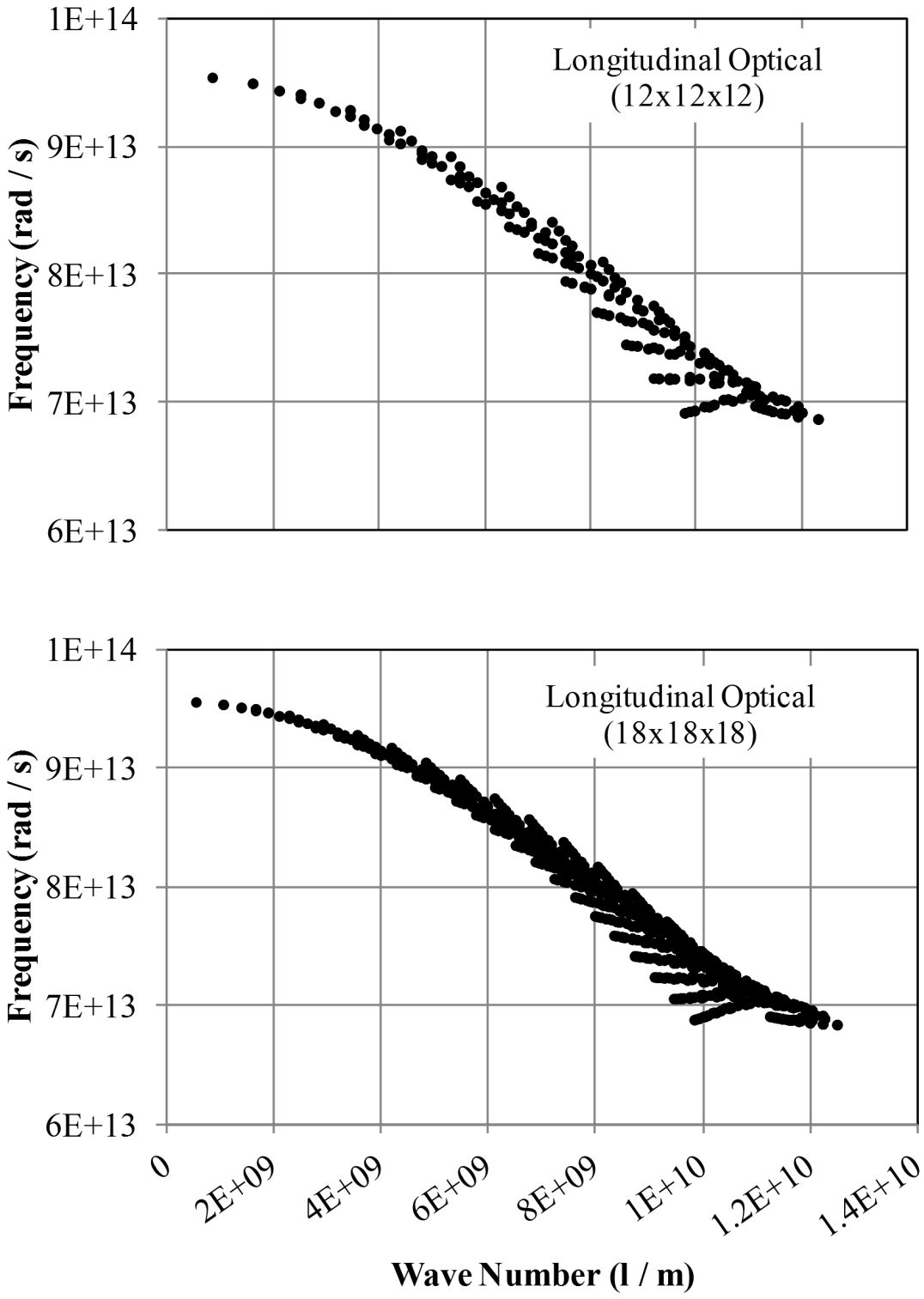

Figure 4.7 Comparison of the longitudinal optical dispersion distributions for $12 \times 12 \times 12$ and $18 \times 18 \times 18$ BZ discretizations.

It is noted that with the finer BZ discretization that the distributions get denser, but the overall characteristic shapes do not change. The dispersion relations in Fig. 2.6 are given for the high symmetry directions. In most MC models the [100] direction is utilized for the isotropic dispersion assumption. If we compare the dispersion distributions shown in Figs. 4.2 through 4.7, utilized by the SPT model, to the isotropic dispersion relations in Fig. 2.6, employed by most MC models, we can see that the isotropic assumption is a significant simplification that may not be sufficient. The ability to consider individual events in intrinsic scattering comes from the representation of the anisotropic BZ shown by the dispersion distributions.

4.3 Group Velocity

In order for the pseudo-state phonon populations to drift throughout a domain at an accurate velocity it is important that the group velocities are accurate. Figures 4.8 through 4.13 show the magnitude of the group velocity distributions in a similar manner to how the dispersion relations were plotted. Similarly, as the mesh discretization is refined, the group velocity distributions get more dense, but the overall shape remains similar.

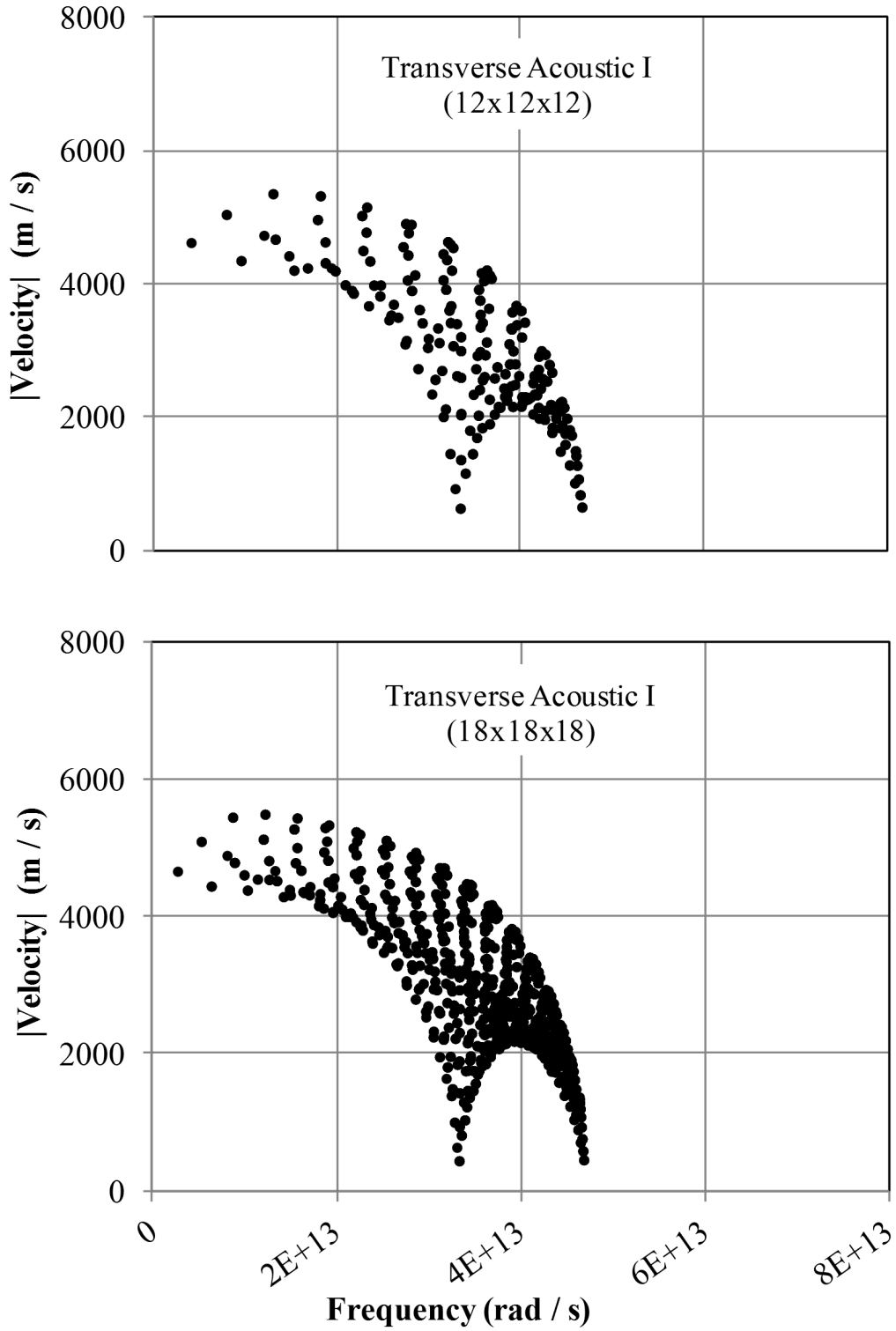

Figure 4.8 Comparison of the transverse acoustic I group velocity magnitude distributions for $12 \times 12 \times 12$ and $18 \times 18 \times 18$ BZ discretizations.

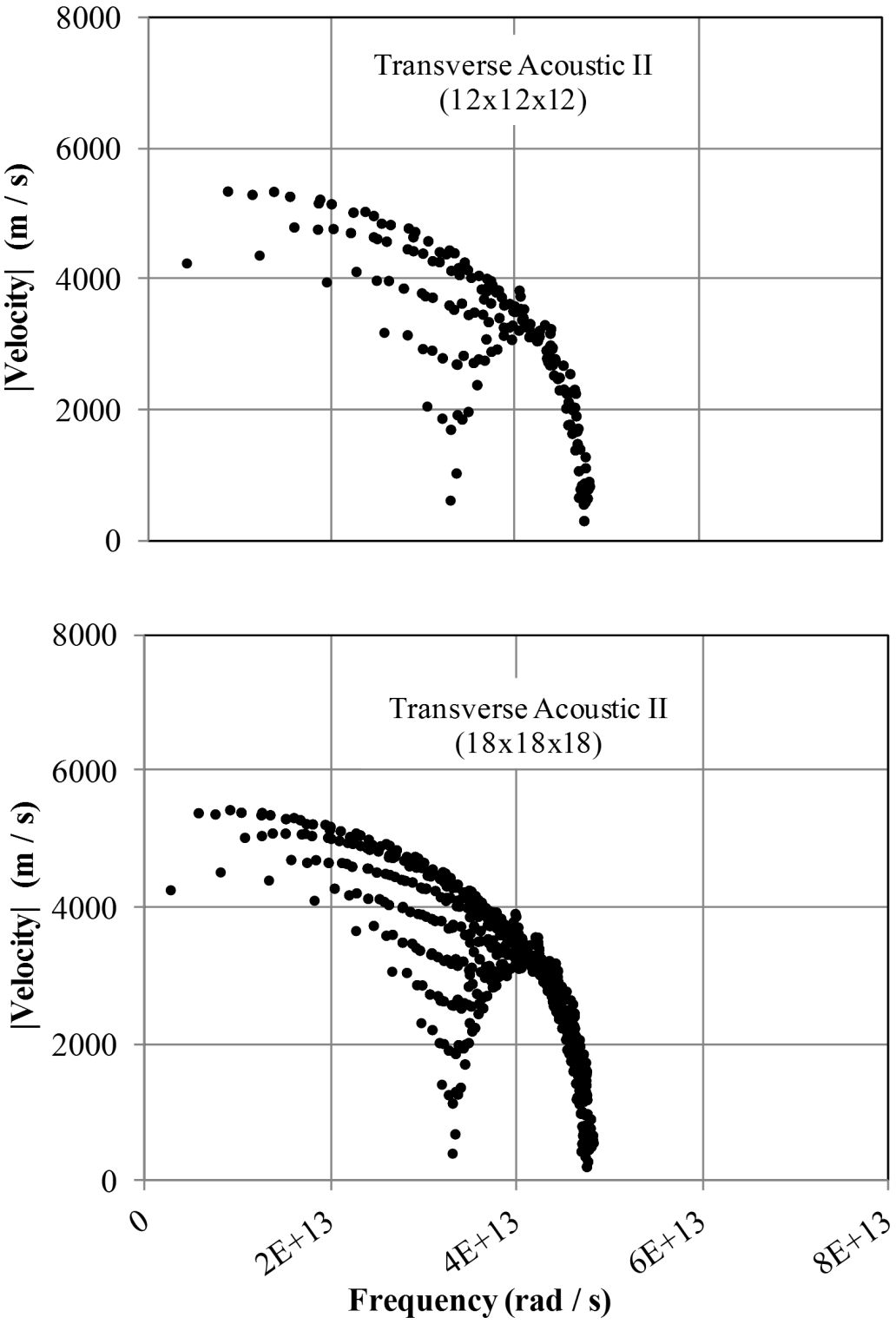

Figure 4.9 Comparison of the transverse acoustic II group velocity magnitude distributions for $12 \times 12 \times 12$ and $18 \times 18 \times 18$ BZ discretizations.

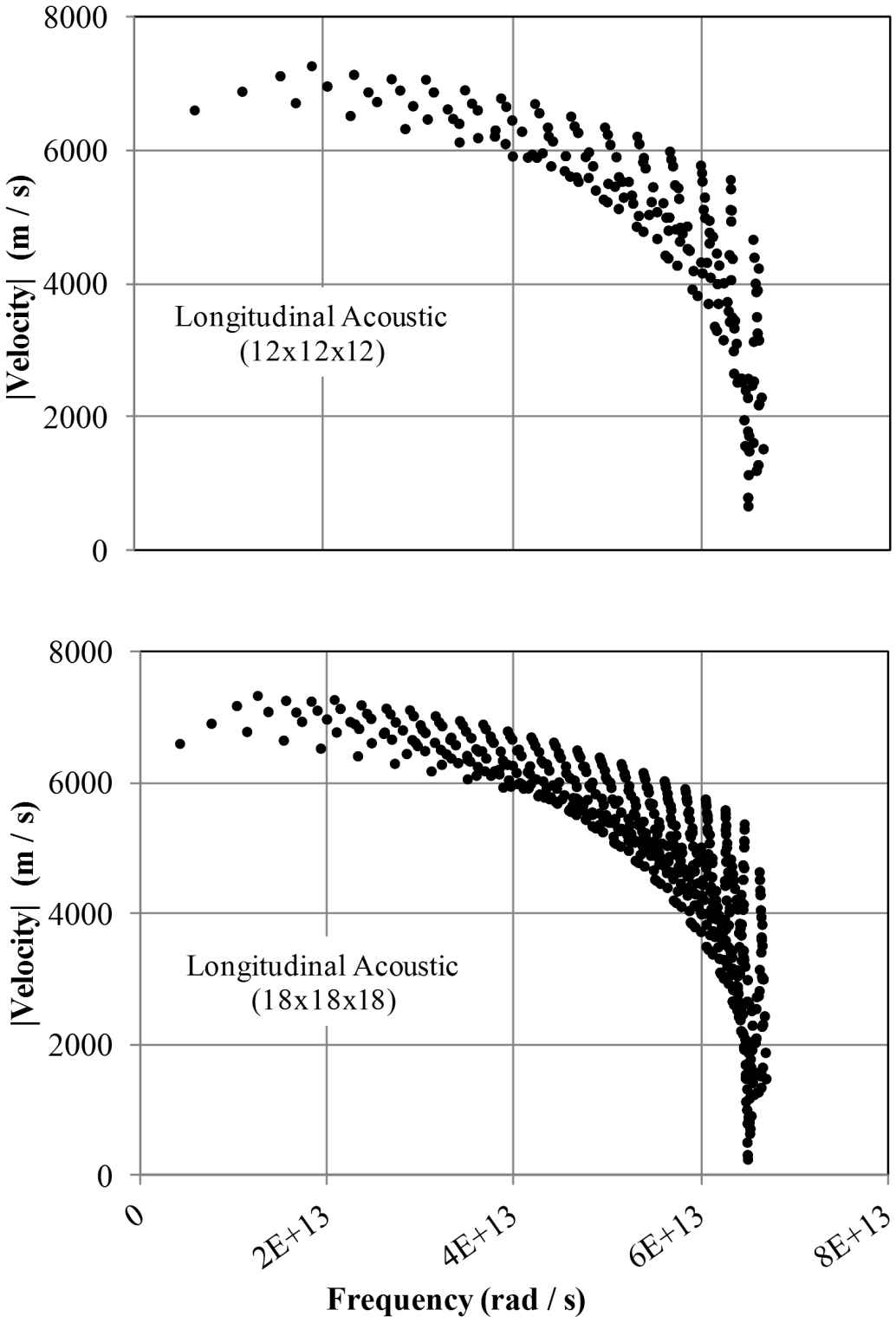

Figure 4.10 Comparison of the longitudinal acoustic group velocity magnitude distributions for $12 \times 12 \times 12$ and $18 \times 18 \times 18$ BZ discretizations.

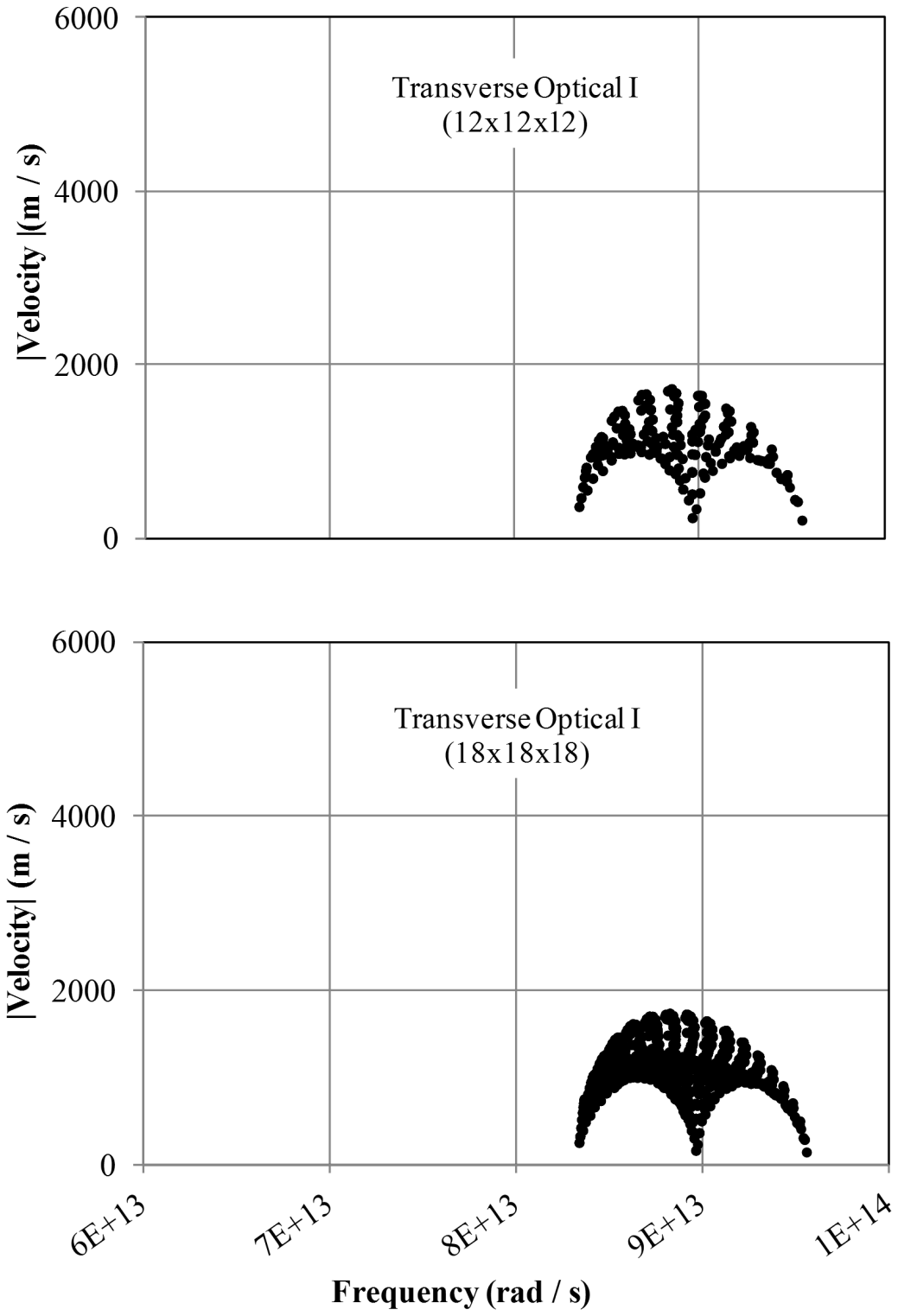

Figure 4.11 Comparison of the transverse optical I group velocity magnitude distributions for $12 \times 12 \times 12$ and $18 \times 18 \times 18$ BZ discretizations.

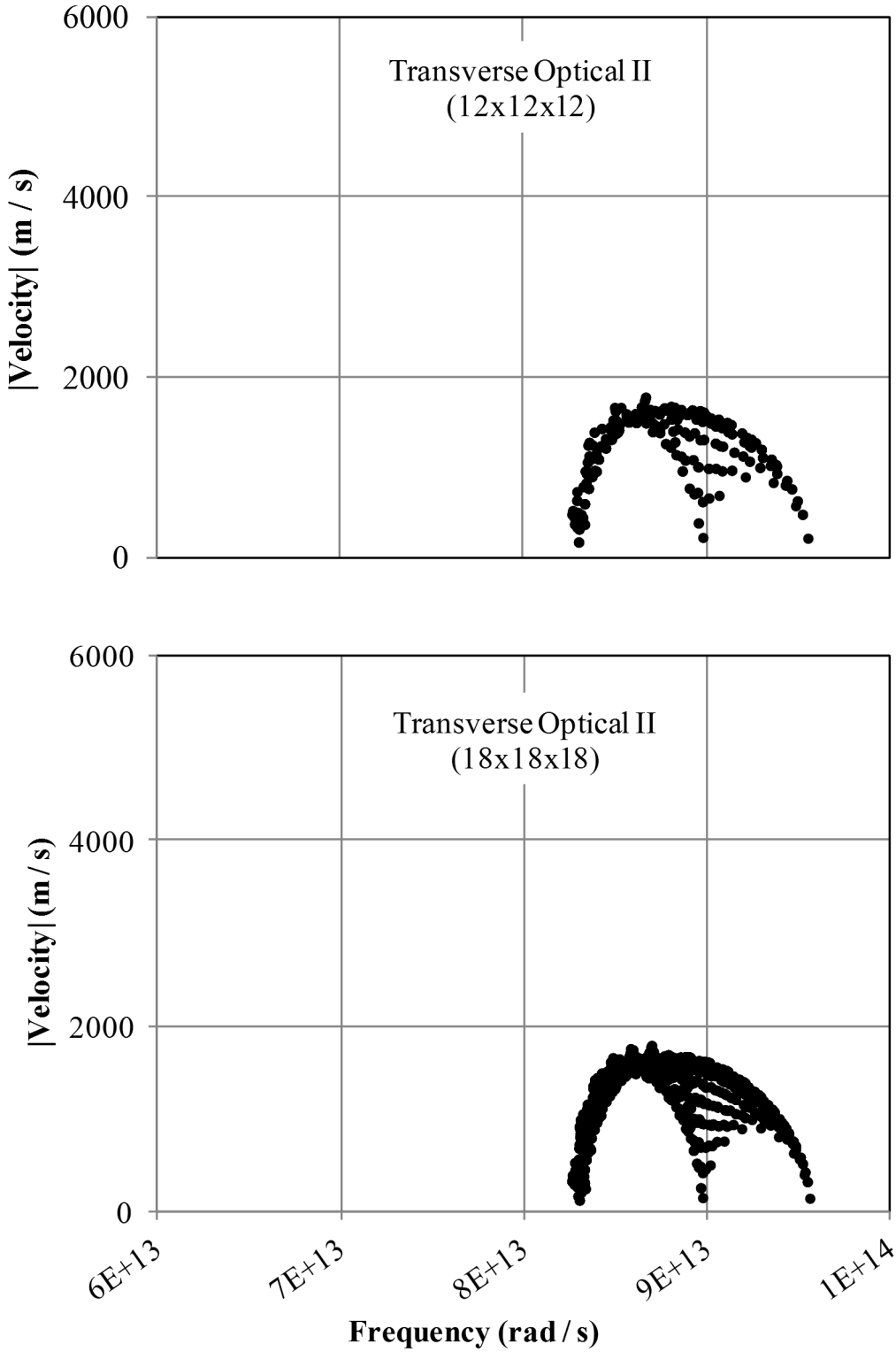

Figure 4.12 Comparison of the transverse optical II group velocity magnitude distributions for $12 \times 12 \times 12$ and $18 \times 18 \times 18$ BZ discretizations.

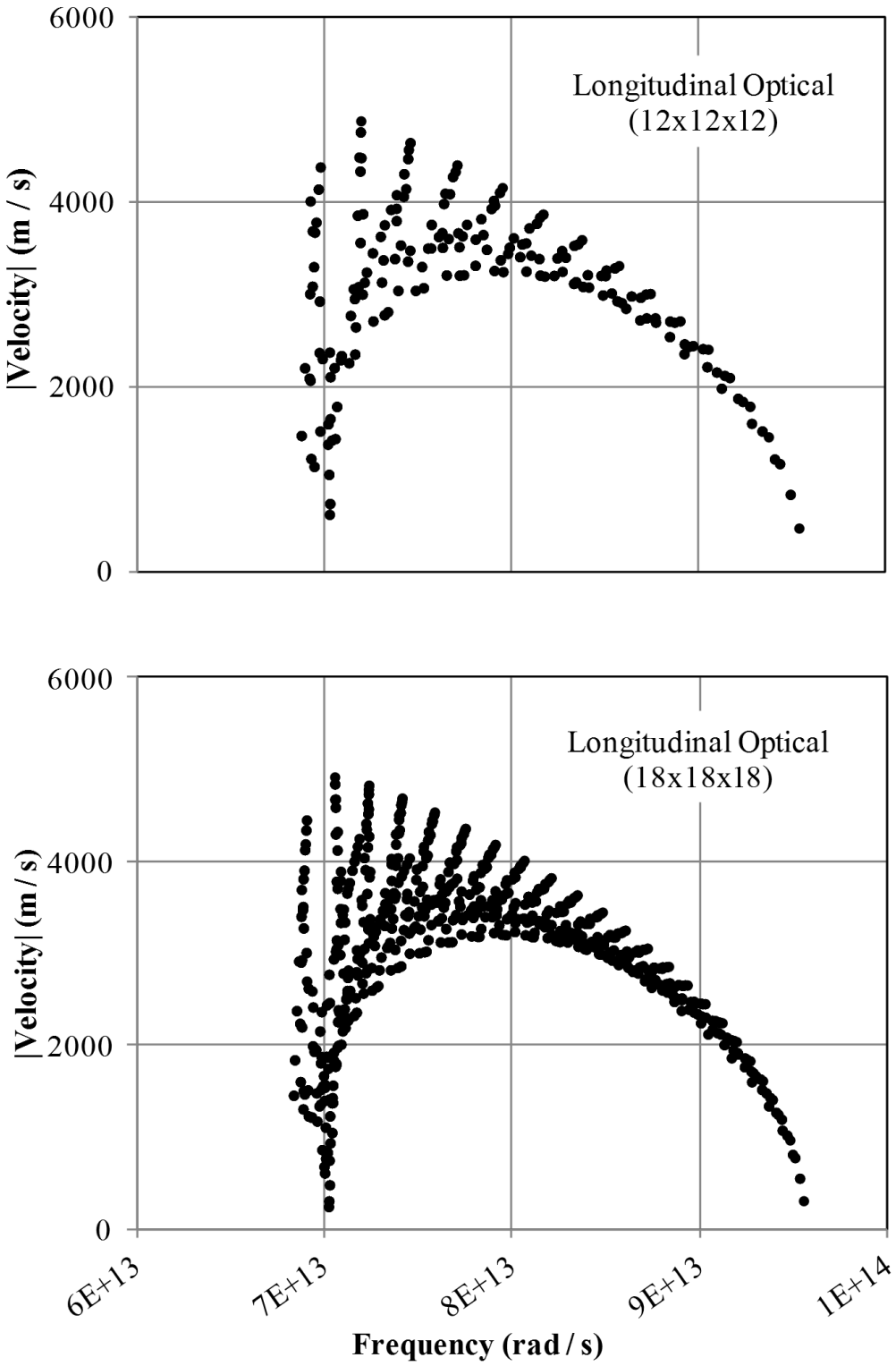

Figure 4.13 Comparison of the longitudinal optical group velocity magnitude distributions for $12 \times 12 \times 12$ and $18 \times 18 \times 18$ BZ discretizations.

The group velocity magnitude distributions shown here that are utilized in the SPT model, can be compared to those in the [100] direction for bulk silicon in Fig. 2.8 that are commonly used in MC models. It is obvious that the group velocity magnitude distributions obtained from the anisotropic BZ give a much more complete representation of how the pseudo-state phonon populations are allowed to drift.

4.4 Density of States

The density of states informs how the energy of a crystal is distributed with respect to frequency. The density of states for four different BZ meshes, 6×6×6, 10×10×10, 12×12×12, and 18×18×18 denoted as Mesh 6, 10, 12, and 18, respectively, are illustrated in Fig. 4.14.

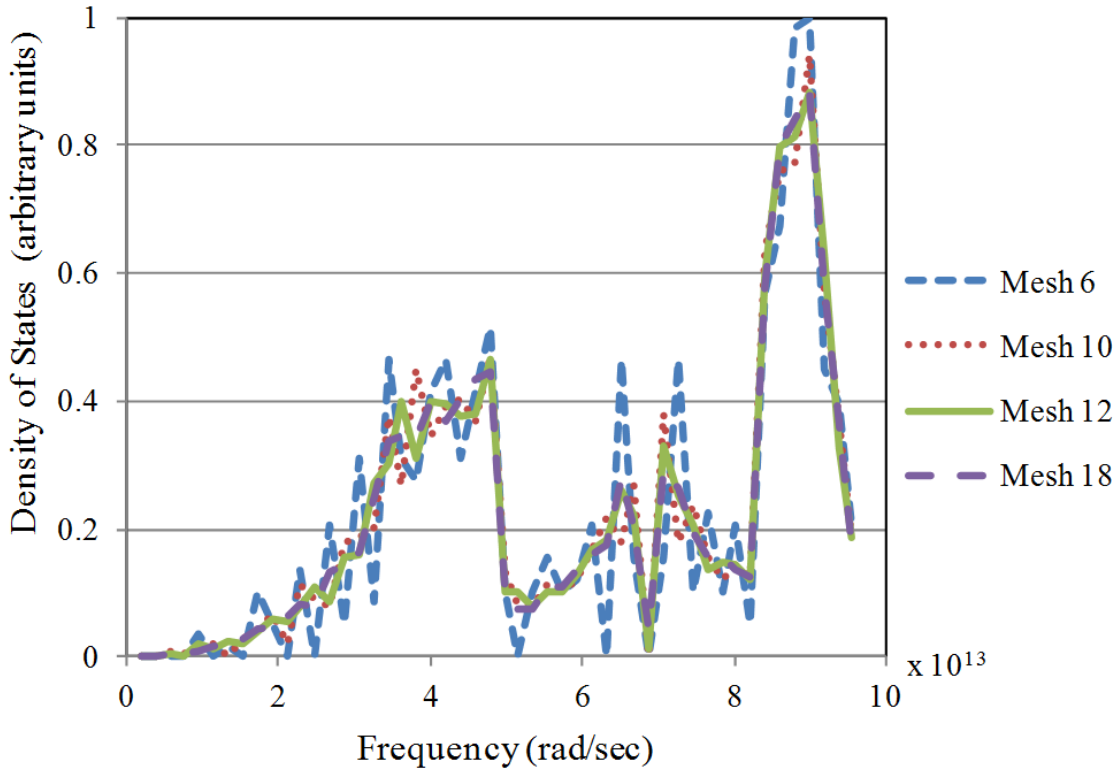

Figure 4.14 Comparison of density of states for silicon for several BZ discretizations.

The density of states shown in Fig. 4.14 was generated using the method described in Chapter 2 § 2.5. These DOS curves were prepared using 50 frequency bins. As the BZ mesh density increases, it is feasible to employ finer frequency bins. For the purpose of assessing BZ mesh density, it is valuable to retain consistent frequency bins for all DOS curves. The DOS of BZ Mesh 6 clearly shows that many frequency bins are not fully described by the discretization, and some of frequency bins are wholly absent. As the BZ mesh density increases, the DOS curves populate all of the bins. The finest discretization, BZ Mesh 18, exhibits a well behaved, smooth distribution for the density of states, and is it quite apparent all frequency bins are present. The DOS curves plotted as a function of BZ mesh refinement are helpful to understand the fidelity of the material property characterization. As the DOS plots converge with BZ mesh refinement, we can be increasingly confident of the accuracy of a particular material model. Additionally, the DOS curves make it possible to evaluate the computational tradeoffs associated with increasing the BZ mesh refinement. The density of states for silicon shown in Fig. 4.14 can be compared to that adapted from Pascual-Gutierrez *et al.* [55] shown in Fig. 2.7.

4.5 Density of Interactions

The density of states provides insight into the accuracy of the material model, but does not provide insight into the fidelity of three-phonon scattering interactions contained in the interaction table. A new concept, denoted as the "density of interactions" (DOI), is introduced as a tool for studying the fidelity of three-phonon scattering events, given a candidate BZ Mesh and frequency acceptance criterion. Upon completion of the interaction table using the energy and pseudo-momentum conservation rules presented previously, the density of interactions may be plotted as a histogram of frequency in a fashion similar to that of a density of states. This DOI depicts the overall participation level of pseudo-states involved in three-phonon interactions, both normal and Umklapp as a function of frequency. The DOI is created by considering each interaction and incrementing the number in the histogram frequency

bin associated with the frequency of each of the three participating pseudo-states. The DOI is shown in Fig. 4.15 for three different meshes for interactions involving only acoustic polarizations. The frequency bins used are consistent with those employed for the density of states. The choice of ω_ε is important to the quality of the density of interactions. A relatively large value of ω_ε, $\omega_\varepsilon = 5\times10^{-3}$ was used in generating Fig. 4.15.

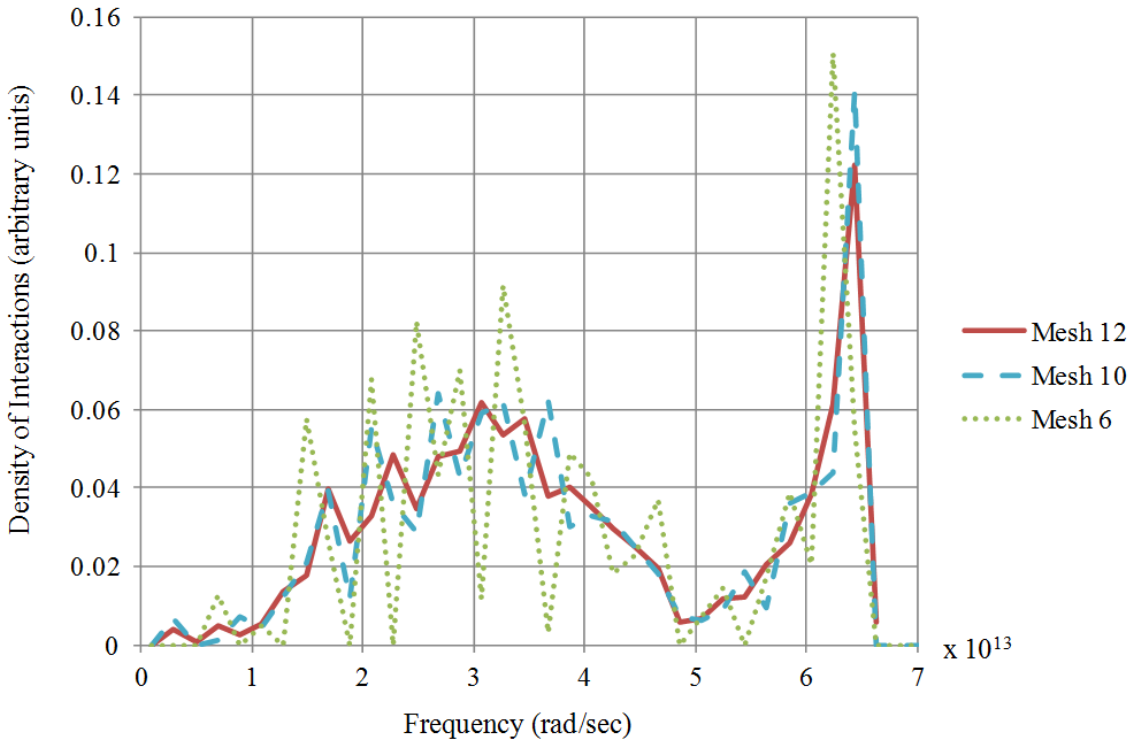

Figure 4.15 Comparison of density of interactions for acoustic polarizations for several BZ discretizations.

The DOI is normalized by the total number of states represented in the interaction table (three times the number of rows in the interaction table, since each row references three pseudo-states). While a figure of this nature has not been reported previously, it has been found that the interaction density spectrum is an excellent measure for the accuracy of the interaction list for a given BZ discretization. In particular, when one frequency band, (particularly) low frequency phonons, dominates the density of

interactions, then the subsequent three phonon scattering results are incorrectly dominated by these events. This effect is implicitly present in the selection rules employed by MC methods, but may be masked through the influence of scaling parameters and other heuristics. Fundamentally, the density of interactions quantifies the quality of stochastic scattering models.

4.6 Pseudo-State Interaction Density

An additional measure of interaction table quality, introduced herein as a "Pseudo-state Interaction Density" (PID), is useful for studying the participation of pseudo-states in the three-phonon scattering interactions. The PID is created by considering each interaction in the interaction table and incrementing the number in the pseudo-state bin associated with each pseudo-state in each row of the interaction table. The PID shown in Fig. 4.16 is for all pseudo-states, m, in the first octant of the BZ for Mesh 12, with $\omega_\varepsilon = 5{\times}10^{-4}$. The PID is normalized by the total number of entries in the data set.

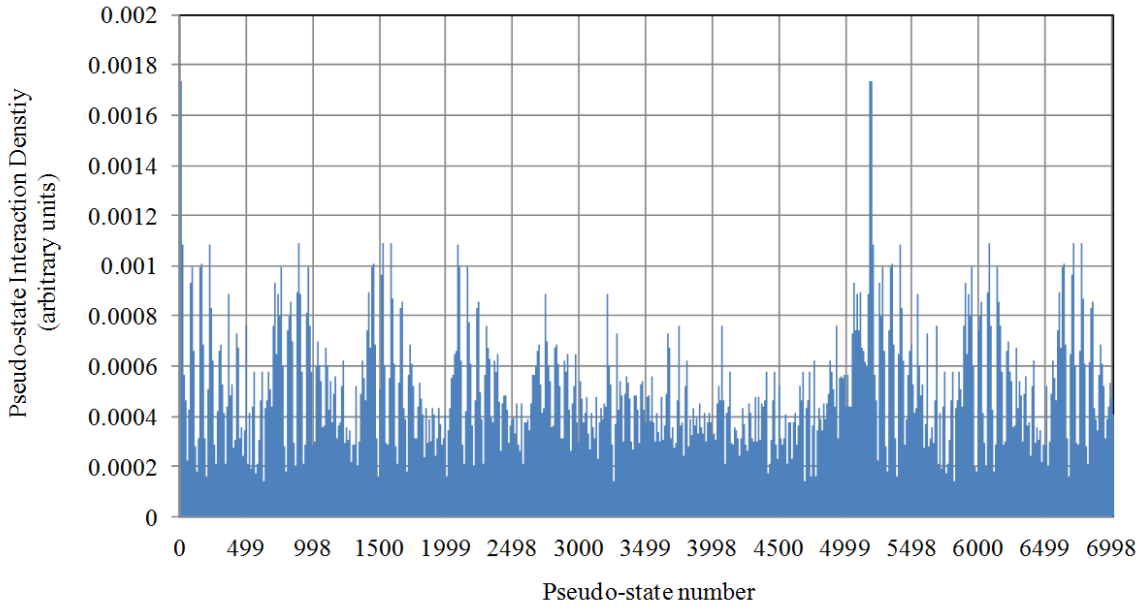

Figure 4.16 Pseudo-state Interaction Density for acoustic phonon pseudo-states in the first ocatant of the BZ, using a three-phonon scattering interaction table computed from BZ Mesh 12.

It is apparent from Fig. 4.16 that some pseudo-states appear in the interaction table more often than others. Detailed evaluation of Fig. 4.16 shows that low energy pseudo-states, near the center of the BZ, occur up to one order of magnitude more often than certain high energy pseudo-states. Depending upon the choice of discretization and frequency acceptance criteria, some pseudo-states may be fully absent from the PID. Also, some pseudo-states may appear only as Type I reactants, and others may appear only as Type II reactants.

A close up of Fig 4.16, shown in Fig 4.17., illustrates the PID for the TA1 phonon pseudo-states along the [100] direction of the first octant of the BZ.

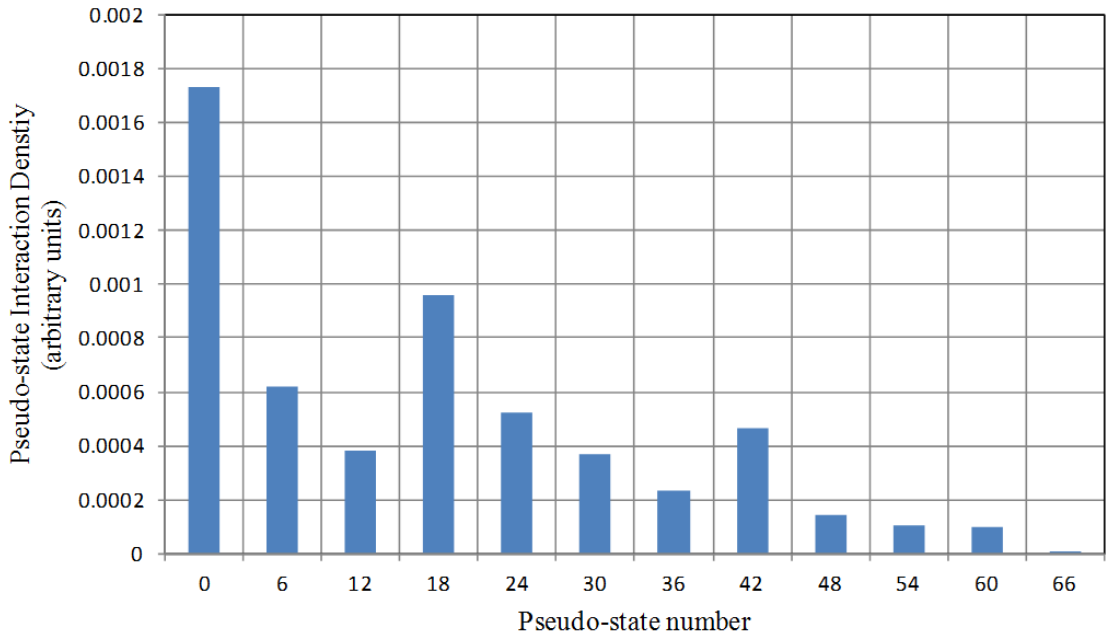

Figure 4.17 Pseudo-state Interaction Density for TAI phonon pseudo-states along the [100] direction with the scattering table computed from a BZ Mesh 12.

The highest energy pseudo-state, m=66, had only one appearance in the interaction table, while the lowest energy pseudo-state, m=0, appeared 720 times. Pseudo-state m=66 appeared only as a Type II reactant, while pseudo-state m=0 appeared only as a Type I reactant. This observation suggests that, based on the BZ discretization and frequency acceptance criterion used here, as a particular state, such as m=66, experiences a Type II decay into two phonons, it adds to the population of a low energy pseudo-state, such as m=0. The design of a subsequent three-phonon scattering algorithm must consider this case in order to enforce Kirchoff's law for those particular pseudo-states.

CHAPTER 5

Three-Phonon Scattering Model Verification

5.1 Single Cell Scattering

The SPT scattering models A and B may be investigated with a single geometric cell. The term "geometric cell" is used to distinguish the discretization of the geometric domain from the term "BZ element" which is used to describe the discretization of reciprocal space. The geometric cell is assumed to be completely isolated from its surroundings, with periodic boundary conditions on all sides, so that all drift phenomena, boundary scattering effects, and other influences such as geometry and isotope scattering may be neglected. A single geometric cell of dimensions $\ell_x \times \ell_y \times \ell_z$ is taken to be isolated at a temperature of $T(K)$. The number of phonons associated with a particular pseudo-state m for this cell volume, pseudo-state number density, and temperature is given by Eq. (3.3), where V_c is the cell volume. It is noted that in the SPT model the full population of phonons is considered without the use of scaling factors. At a temperature of 500 K, with ℓ_x=ℓ_y=ℓ_z=100 nm, the total number of phonons contained in the single geometric cell is 9.024×10^7, which are distributed across $41,472$ pseudo-states in accordance with Eq. (3.4) for a $12 \times 12 \times 12$ BZ discretization. Note that only acoustic modes are considered for scattering in the

current work, while both acoustic and optical modes may be populated for computing the proper internal energy of the geometric cell. Optical modes are present as storage terms, but are not permitted to scatter in the current presentation.

In order to evaluate the SPT framework, and compare scattering models "A" and "B", a single cell scattering study was performed. In this study phonon pseudo-state populations were initialized at an equilibrium distribution corresponding to an arbitrary temperature T=500 K using Eq. (3.3). The pseudo-state populations were uniformly distributed throughout a single three-dimensional cell of volume $V_c = \ell_x \times \ell_y \times \ell_z$. Multiple iterations of three-phonon scattering for acoustic only modes were performed and the relative rates of Type I and II events for each process, resulting distributions, and several other key aspects were studied.

5.1.1 Scattering Model A Results. If an interaction scheme is to be deemed reasonable, the phonon pseudo-state population distribution should remain the same after successive iterations of the three-phonon scattering algorithm at equilibrium. The following figure shows the population history for several exemplar states along the [100] direction of the BZ. These states represent acoustic mode TAI. In order to illustrate both the positive and negative aspects of model A, the linear CDF illustrated in Fig. 3.12 was chosen to have a broad distribution, allowing the populations of each pseudo-state to vary $+/-45\%$ of its equilibrium population. In this example, the geometric cell was populated with phonons at the Bose-Einstein equilibrium distribution for $T = 500\ K$. The single cell was then permitted to scatter in accordance with the rules of model A for $10,000$ iterations. The resulting phonon population history for selected states is illustrated in Fig. 5.1.

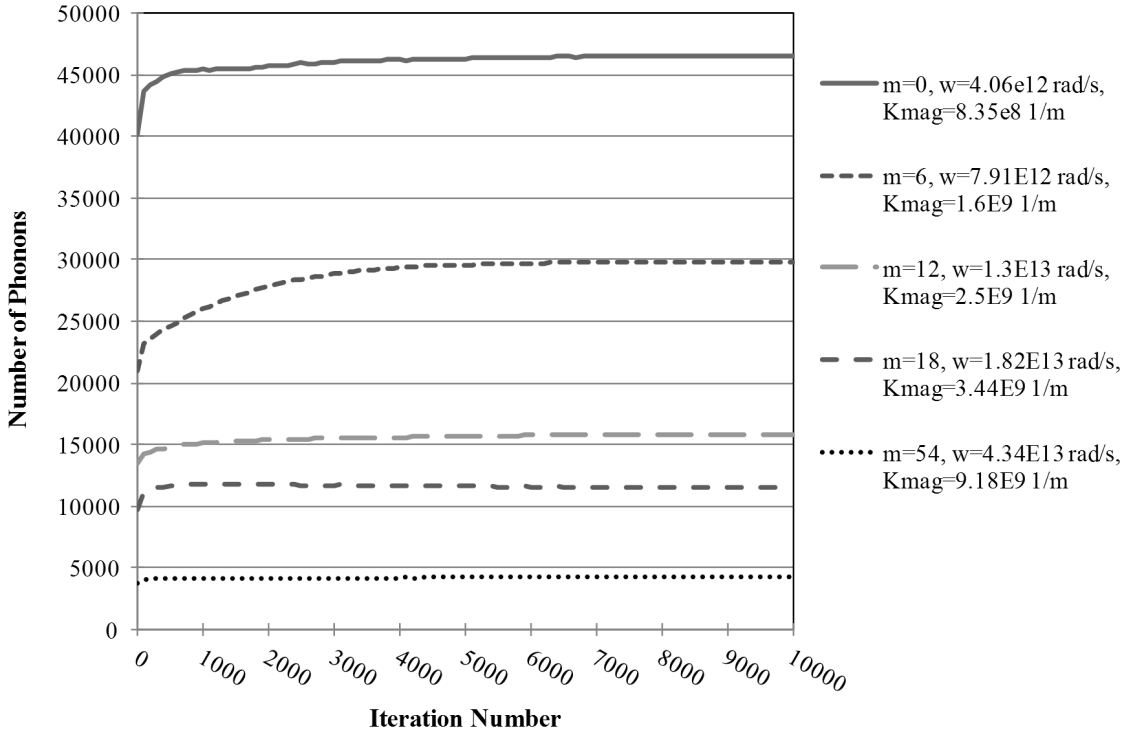

Figure 5.1 Scattering model A phonon population history for selected pseudo-states along the [100] direction of the BZ.

The pseudo-state phonon populations shown in Fig. 5.1 gradually move towards their equilibrium populations as a result of three-phonon scattering. The iteration history of each pseudo-state shows the change in the pseudo-state phonon population throughout the single cell scattering study. The results clearly indicate that states $m = 0$ and $m = 6$ gain a disproportionate share of phonons, while higher frequency states lose a relatively small number of phonons. At long times, the populations come to a new equilibrium condition, which is reflective of the accuracy of the BZ mesh used to model the material. As the mesh is increasingly refined, its accuracy improves and the error associated with approximating the pseudo-state energy with its centroid frequency is reduced. It should be noted that the very broad limits allowed for the linear CDF are the primary reason for allowing the large shift in the population of low frequency states. A tighter limit on the CDF (a more strict definition of donor and recipient phonon-states) reduces the population shift directly.

As the limit approaches zero, fewer scattering events are permitted to occur. Note also that model A assumes that all frequencies of phonons decay at equal rates, while it is well known that lower frequency acoustic phonons have longer relaxation times than higher frequency phonons. Through selection of tighter limits on the CDF, it is possible to demonstrate results which exhibit virtually no change from Bose-Einstein equilibrium. However, permitting the large variation in population is instructive. Numerical experimentation shows that a poor choice for ω_ε, coupled with a wide CDF, will cause the low frequency phonons to dominate the response since there are many more interactions which conserve energy and allow the low frequency states to participate. The density of interactions is helpful to understand this dynamic. The SPT model facilitates thorough investigation of the assumptions underlying proposed interaction and scattering algorithms. Such investigation is not possible, or is computationally prohibitive for MC simulations.

Figure 5.2 shows the ratio of forward to reverse interaction probabilities for the first 100 successive iterations.

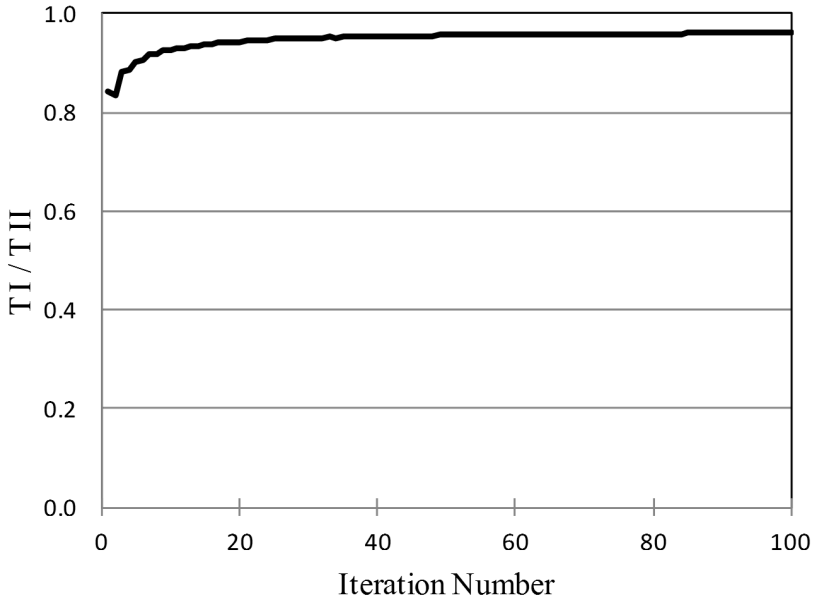

Figure 5.2 Ratio of forward to reverse interactions for 100 iterations of scattering model A.

From the initial condition until the conclusion of $100,000$ scattering iterations, the energy within the cell was conserved at 3.6461×10^{-13} Joules, and a cumulative 2.8×10^{11} phonons were scattered, in approximately equal numbers of Type I and Type II events. Figure 5.2 illustrates that Kirchoff's law is satisfied within the accuracy of the mesh model, and as the system approached an equilibrium condition the number of Type I and Type II events remained nearly equal. At equilibrium, large numbers of scattering events were observed, but virtually no net change in phonon populations resulted.

5.1.2 Scattering Model B Results. Model B was investigated in a manner similar to model A. However, the perturbation limit used in Eq. (3.35) causes the number of scattering events to go to zero at equilibrium. Thus, when the geometric cell was populated with phonons in accordance with Eq. (3.4), and the system was allowed to iterate under model B, no scattering events occurred. In order to induce a disturbance to the system, 5% of the energy was removed from pseudo-state $m = 12$ and was added to pseudo-state $m = 54$. The phonon population response subject only to the limitations of model B are illustrated in Fig. 5.3, using a time step of $0.001\ ps$.

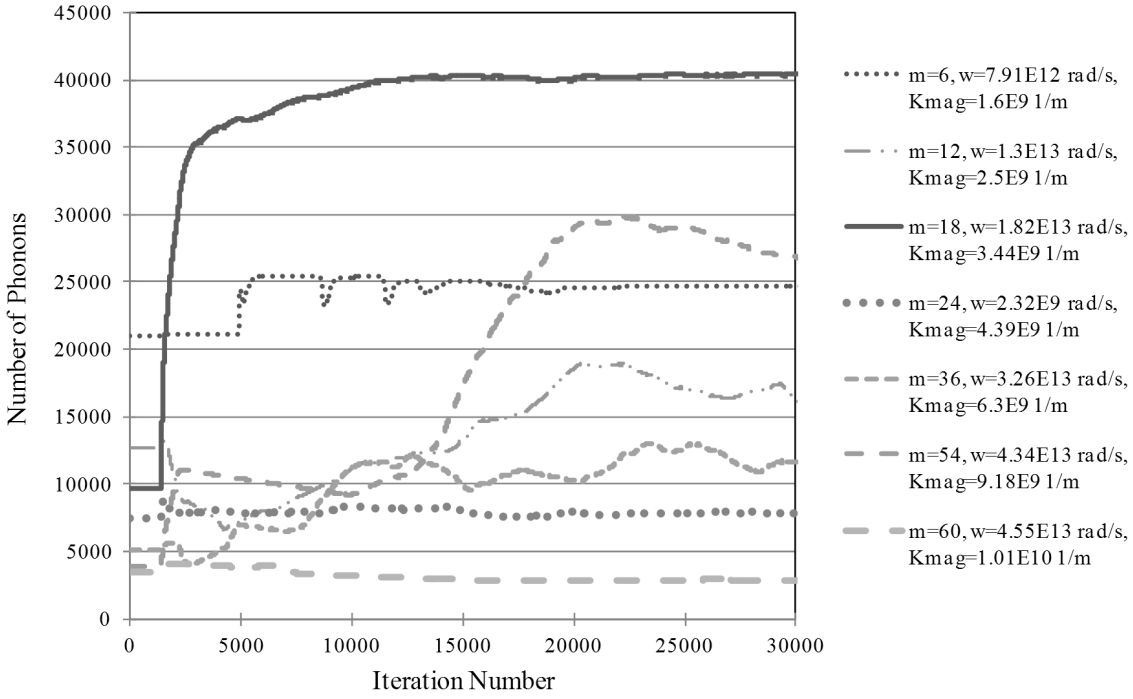

Figure 5.3 Scattering model B phonon population history for selected pseudo-states.

Because the perturbation model places no upper limit on the phonon populations, but rather shuts it "off" as equilibrium is approached, the population of pseudo-state $m = 18$ grows to four times its equilibrium population in response to the small disturbance. This is primarily a manifestation of the manner in which the interaction table was constructed, and the fact that the simplified relaxation time model does not accurately account for the anharmonic nature of discrete scattering events. As with model A, the ratio of Type I to Type II events was monitored, and it was confirmed that Kirchoff's law was satisfied, as were conservation of energy and pseudo-momentum.

Model B contains a simplified relaxation time model to reflect the dynamic response of the system in contrast to model A, which modeled the scattering events independently of time scale. The ratio of the mean phonon lifetime for the populations

of phonons over the corresponding relaxation time for the pseudo-state is presented for several exemplar pseudo-states in Fig. 5.4.

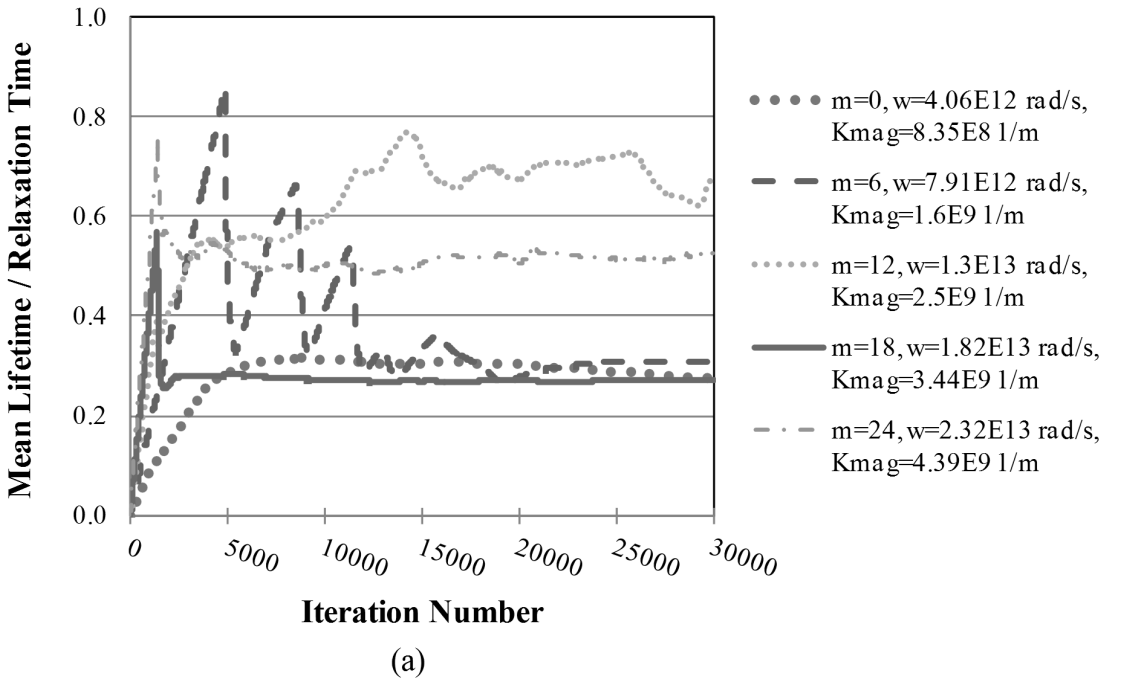

(a)

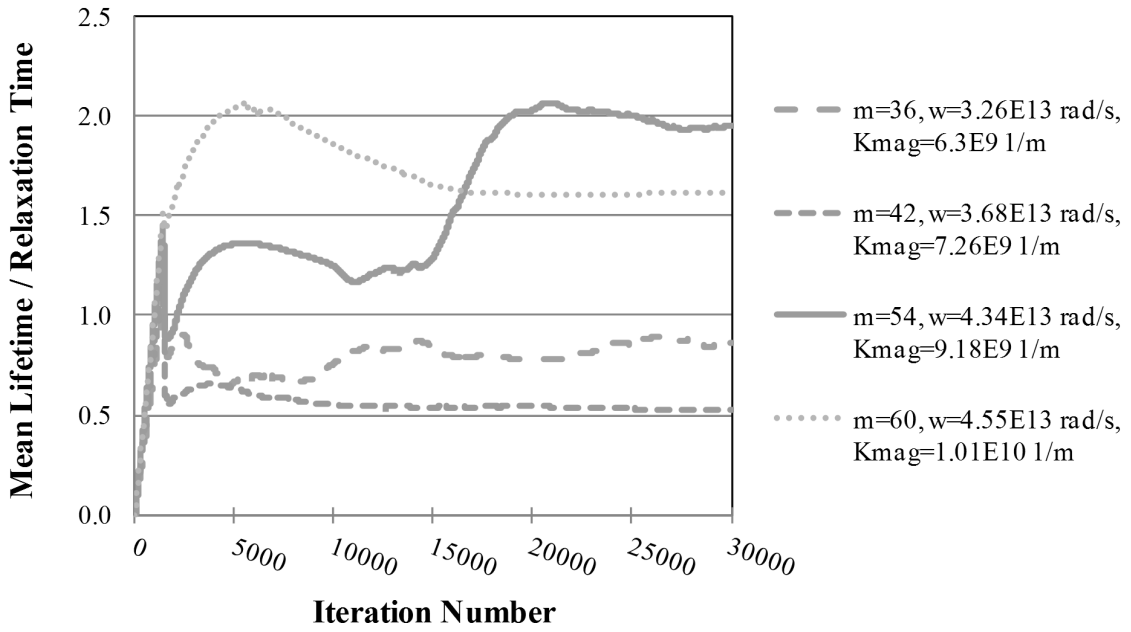

(b)

Figure 5.4 Scattering model B mean pseudo-state lifetime ratio for selected pseudo-states along the [100] direction of the BZ.

As illustrated in Fig. 5.4, pseudo-states $m = 54$ and $m = 60$ exhibit ratios in excess of unity, while the other states exhibit lifetimes below unity. The linear growth of each curve at early times reflects the fact that the mean lifetime of the populations has not yet risen to a level to enable scattering of that pseudo-state. As the mean lifetimes increase, the probability of the pseudo-state participating in scattering events increases, and the pseudo-state population changes accordingly.

In investigating various pseudo-states mean lifetime ratios it was noticed that some states grew unbounded. It was determined that these pseudo-states were only represented in the reaction side within the interaction table. These tended to be lower wave number pseudo-states who could not decay into two pseudo-states following the energy and pseudo-momentum selection rules.

5.1.3 Scattering Model Observations. Two models for scattering have been investigated, employing attributes common to many MC methods. Scattering model A permits a treatment of fully anisotropic scattering and requires no empirical inputs. Additionally, it allows the system to be bounded around an equilibrium distribution through specification of a narrow or wide linear cumulative distribution function. Scattering model B permits a realistic treatment of phonon lifetimes and is built upon a perturbation theory foundation, although greatly simplified in the interest of computational efficiency. Neither proposed scattering model captures all of the features desired for an effective three-phonon scattering model. The SPT framework permits a rigorous investigation of scattering algorithms and provides insight into the dynamic response of phonon transport systems. Future work will investigate a hybrid of both scattering models, using the first model to limit populations to a band around equilibrium, and the second model to capture the dynamic response characteristics. A full perturbation model, following Pascual-Gutierrez *et al.* [55] is believed to be the "ideal" scattering state transition model for the SPT model, but is not computationally feasible at the current time. Subsequent thermal transport results presented herein will utilize scattering model A.

CHAPTER 6

Thermal Transport Validation

Verification results of the SPT model in both the diffuse and ballistic transport regimes are presented using scattering model A. Additionally, the ability of the SPT model to handle adiabatic boundary conditions is demonstrated. Comparisons of results from the SPT model are compared to similar results from literature generated using the MC technique.

6.1 Adiabatic Boundary Verification

Based on the previous description of the isothermal boundary condition, its validation can be accomplished by considering a domain similar to that shown in Fig. 3.3 with all cells initialized at the same arbitrary temperature. If the drift phase of the model is implemented, the domain temperature should remain constant and the net energy flux throughout the domain should be zero throughout the simulation. To verify this, the dimensions of the silicon domain were chosen to be $L_z = \ell_z = 50\ nm$, $L_y = \ell_y = 50\ nm$, $L_x = 250\ nm$, and $\ell_x = 50\ nm$. For the y and z domain boundaries the periodic boundary condition was used, representing 1-D transport. The isothermal boundary temperatures T_h and T_c were both held at 30 K, respectively. The

simulation was allowed to run for 4 ns and after each time step the temperature of the domain and net flux at the isothermal boundaries were computed. It was verified that the temperature remained at 30K throughout the domain with zero net flux after each time step.

To validate the adiabatic boundary condition thoroughly it is necessary to confirm that as the degree of specularity of the boundary surfaces changes that the model exhibits the correct behavior, qualitatively. The SPT model was used to simulate a silicon thin film of dimensions $L_z = \ell_z = 50\ nm$, $L_y = \ell_y = 50\ nm$, $L_x = 500\ nm$, and $\ell_x = 50\ nm$. These results were previously reported by Brown and Hensel [59]. The isothermal boundary temperatures T_h and T_c were held at 40 K and 30 K, respectively. The z domain boundaries represent adiabatic scattering walls. The degree of specularity of these surfaces was varied from zero to unity. No other forms of scattering were considered. The results are shown in Fig. 6.1.

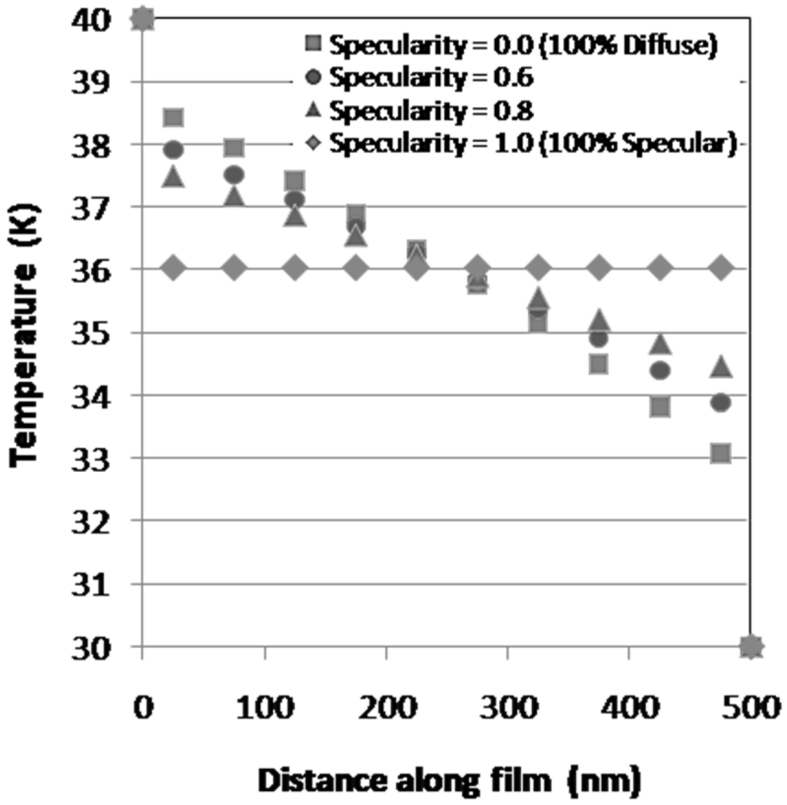

Figure 6.1 Steady-state temperature distribution in a silicon thin film in the ballistic transport regime for various degrees of specularity [59].

As the degree of specularity was decreased, boundary scattering at the z domain boundaries increased and a temperature gradient was established across the thin film. These results further validate the adiabatic boundary condition. These results are consistent with results obtained using the MC technique [10, 15]. The following figure illustrates the quality of results obtained for a similar simulation using the MC technique [15].

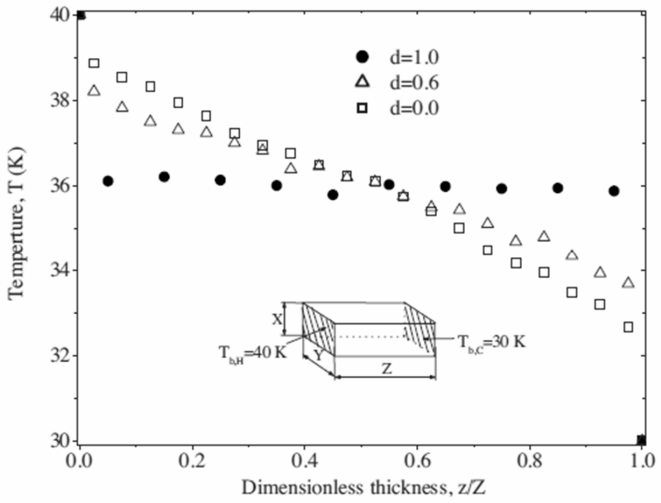

Figure 6.2 Influence of scattering by boundaries on the heat conduction across silicon films of 500 nm thickness at very low temperatures [15].

The results from the SPT model shown in Fig. 6.1 do not exhibit statistical noise as the results in Fig. 6.2 do since the SPT model does not require random number generation during the simulation.

6.2 Ballistic Transport Regime Verification

In the ballistic regime, phonon transport is governed by the Stefan-Boltzmann law. The SPT model was then used to simulate ballistic transport in a silicon nanowire of dimensions $L_z = \ell_z = 50\ nm$, $L_y = \ell_y = 50\ nm$, $L_x = 250\ nm$, and $\ell_x = 50\ nm$. For the y and z domain boundaries the periodic boundary condition was used, representing 1-D transport. The isothermal boundary temperatures T_h (cell 0) and T_c (cell 6) were held at 25 K and 15 K, respectively. All interior cells $(1-5)$ were given an initial temperature of T_c. The steady state analytical solution from the Stefan-Boltzmann law and the numerical SPT model results are shown in Fig. 6.3.

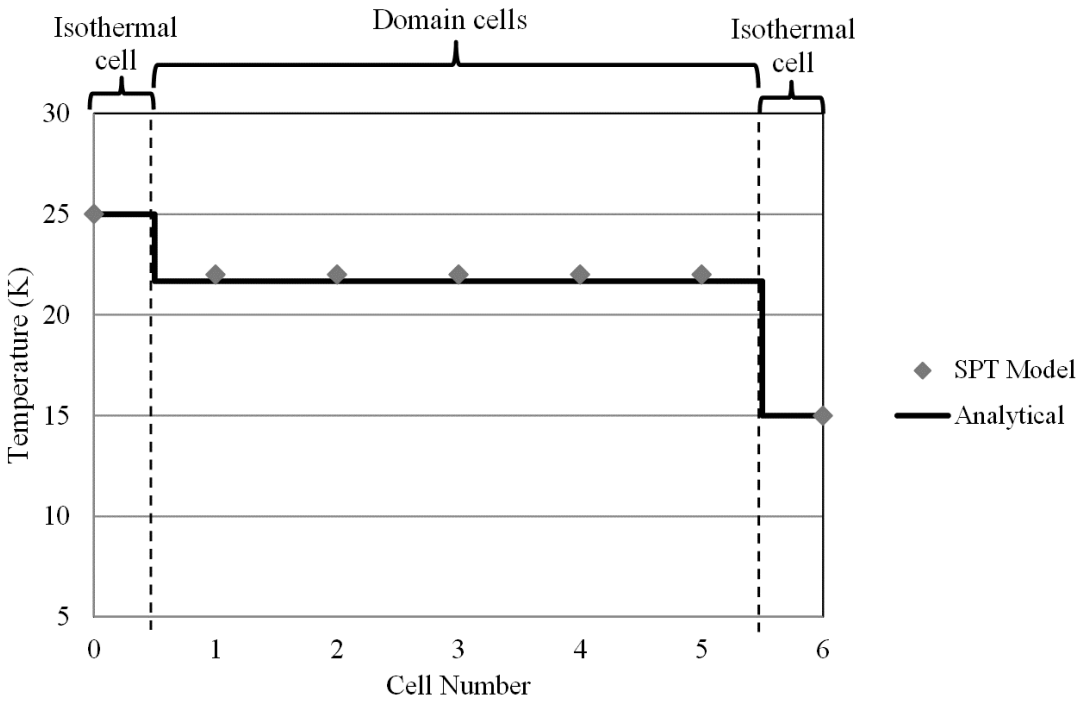

Figure 6.3 Comparison of steady-state temperature distribution in silicon in the ballistic transport regime using the SPT model and the Stefan-Boltzmann law.

The relative error was approximately 1%. These results confirm the ability of the SPT model to simulate thermal transport in the ballistic regime. Results from Mazumder and Majumdar [12] are shown in Fig. 6.4.

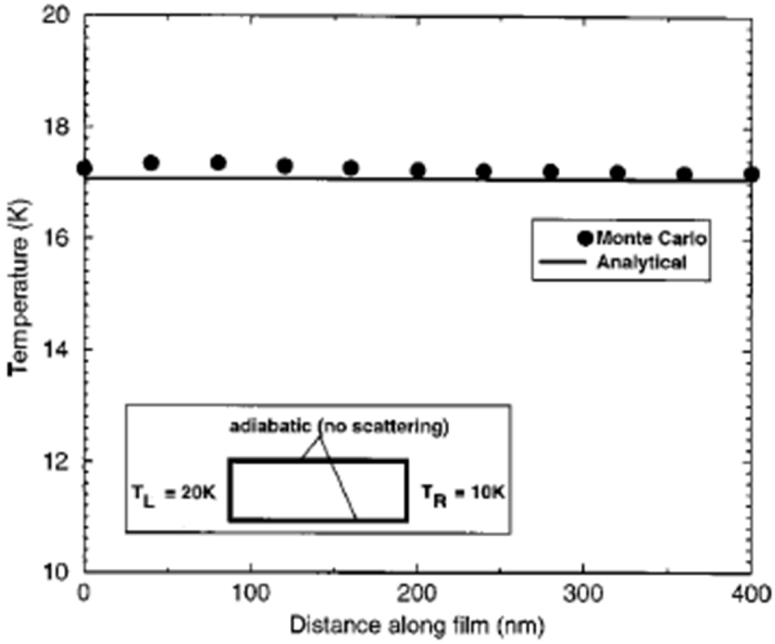

Figure 6.4 Comparison of the temperature profile obtained by MC solution of the BTE for phonons with analytical results in the ballistic limit [12].

It is evident that both the SPT model and MC technique appear to be capable of predicting thermal transport in the ballistic regime. However, the MC result shown in Fig. 6.4 exhibits slight fluctuations in the steady-state temperature profile that are not present in the SPT model or the analytical solution.

6.3 Size Effect Verification

Next, the role of the size effect on thermal transport and the ability of the SPT model to capture this phenomena was studied. As the characteristic dimensions of a structure approach that of the phonon mean free path, regardless of temperature, ballistic transport should be observed. The domain dimensions were $L_z = \ell_z = 50$ nm, $L_y = \ell_y = 50$ nm, and ℓ_x was held constant at 50 nm while L_x was varied from 200 nm to 2000 nm. The isothermal boundary temperatures T_h and T_c were held at 505 K and 495 K, respectively. Similarly, all cells were given an initial temperature of T_c. The resulting steady-state temperature profiles are shown in Fig. 6.5.

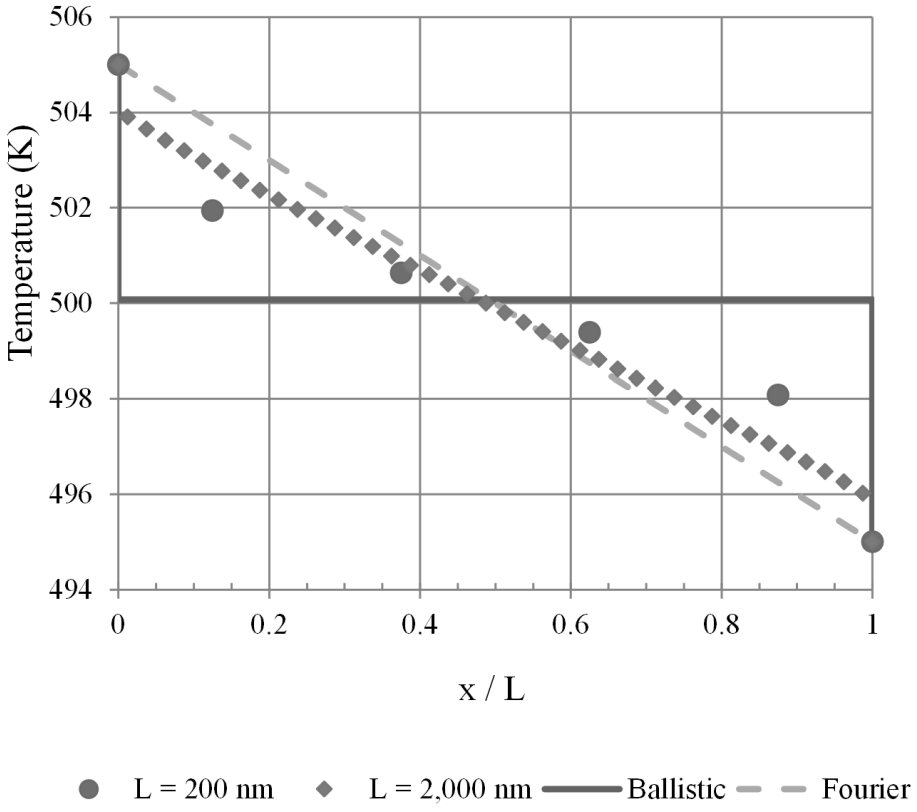

Figure 6.5 Steady-state temperature distribution in silicon in the mixed transport regime.

These results show that as the domain length decreases a mixed thermal transport regime is present and that the SPT model is able to capture this phenomenon.

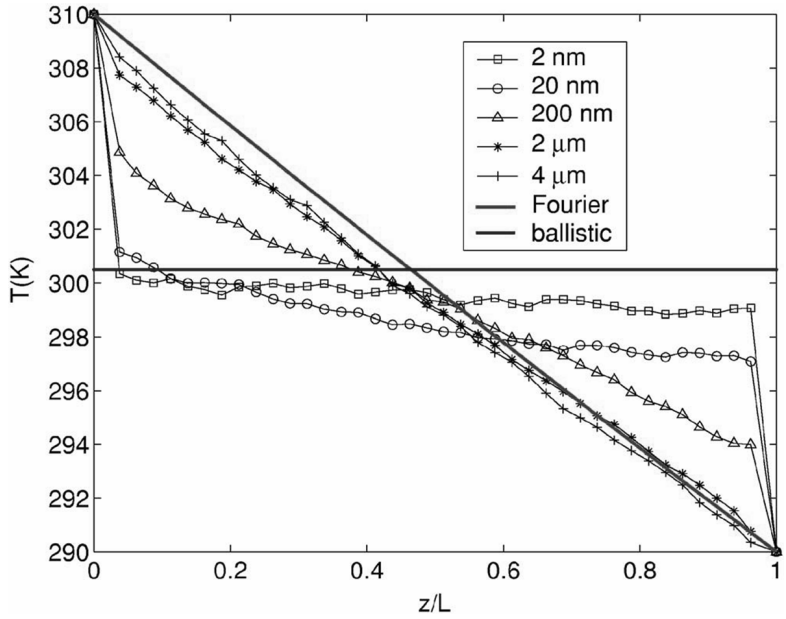

Figure 6.6 Steady-state temperature for silicon, influence of the slab thickness; comparison to the analytical solution in the diffusive and ballistic limits [13].

Similar to previous comparisons, by comparing results from the SPT model shown in Fig. 6.5 with those from the MC solution technique [13] shown in Figure 6.6 it is apparent that the SPT model does not suffer from the fluctions present in the MC model.

6.4 Diffuse Transport Regime Verification

In the diffuse regime phonon transport is governed by Fourier's Law. The ability of the SPT model to accurately predict thermal transport in the diffuse regime was examined using a domain similar to that in the ballistic verification study. The domain dimensions were $L_z = \ell_z = 50\ nm$, $L_y = \ell_y = 50\ nm$, and $L_x$was held constant at 2000 nm while ℓ_x was varied. The isothermal boundary temperatures T_h and T_c were held at 505 K and 495 K, respectively. Similarly, all cells were given an initial temperature of T_c.

The steady state profile compared to the Fourier solution is shown in Fig. 6.7.

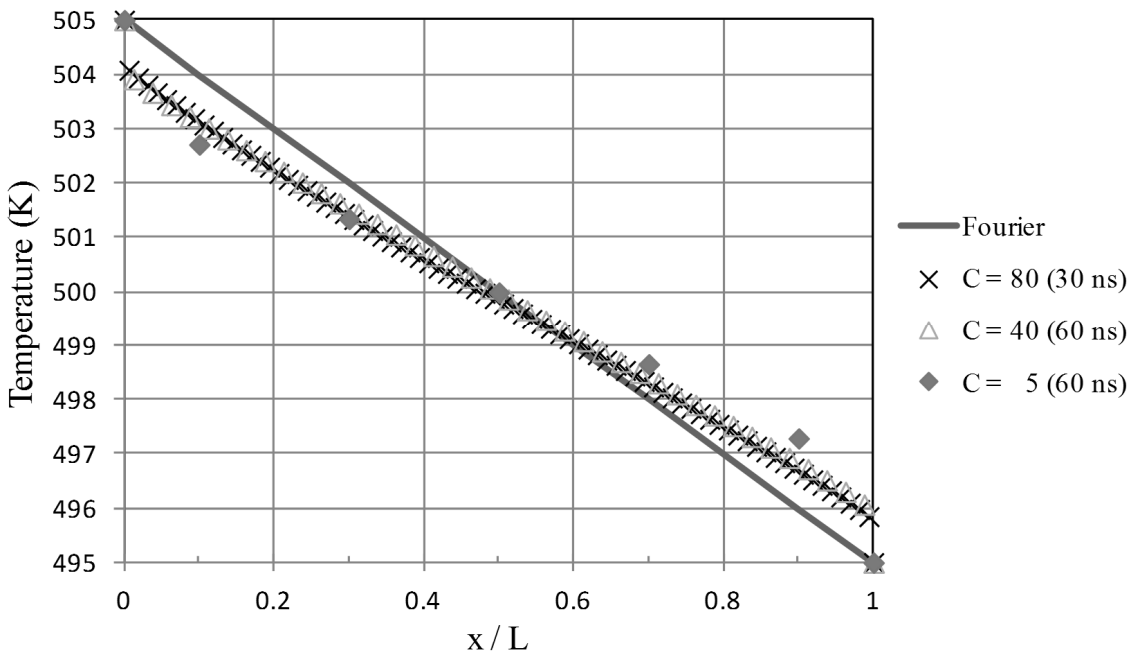

Figure 6.7 Steady-state temperature distribution for bulk silicion in the diffuse transport regime.

It is observed that there is a slight ballistic effect occurring near the boundaries of the domain, which decreases as the number of cells in the x direction is increased from 5 to 40. There is a less noticeable change in the temperature jump at the boundaries as the number of cells is increased from 40 to 80. Ballistic effects near domain boundaries have been mentioned by several MC investigators [12, 13].

In addition to computing the temperature of each cell during the simulation, the mid-plane cell flux is computed based on Eq. (3.14). For the current simulation the flux results are shown in Fig. 6.8. It is noticed that as the domain mesh is refined, the average flux tends to decrease.

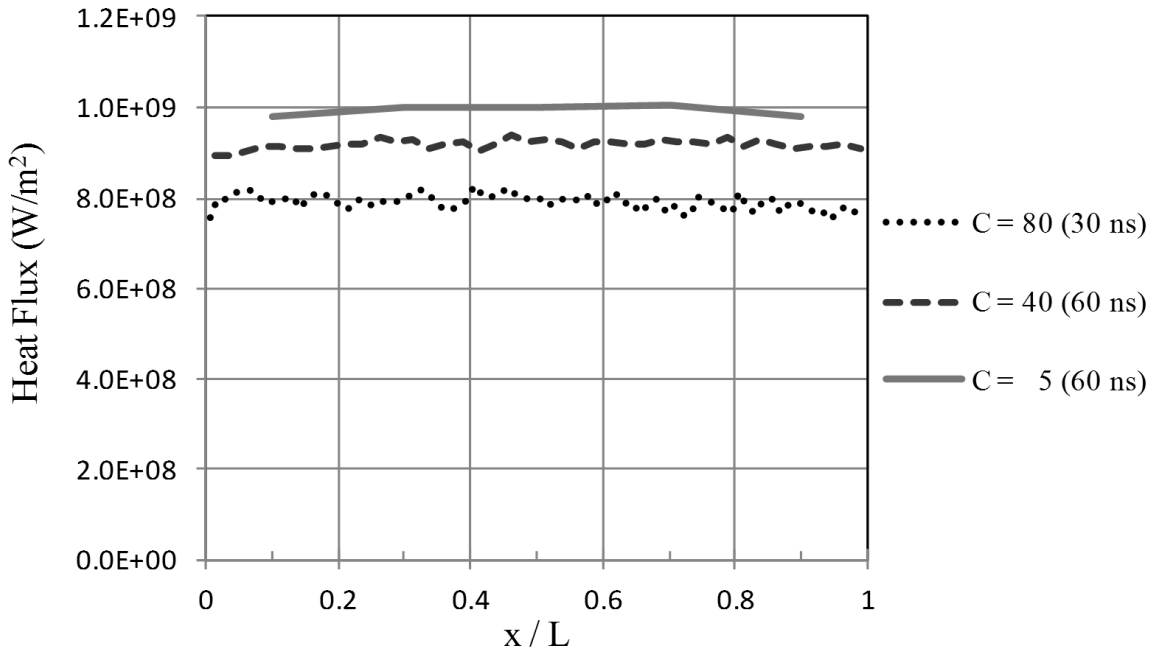

Figure 6.8 Steady-state flux for bulk silicon in the diffuse transport regime.

Once a simulation has reached steady-state and the flux at each cell midplane is extracted for the entire domain, Fourier's law can be used to compute the effective thermal conductivity. Figure 6.9 contains effective thermal conductivity data for the simulation.

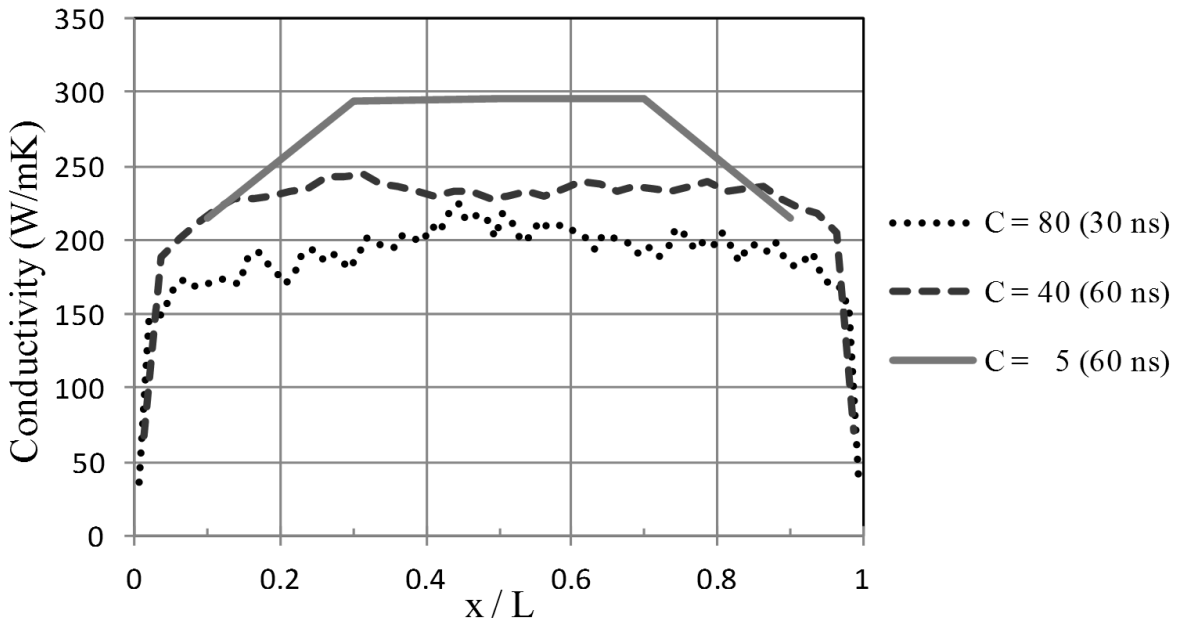

Figure 6.9 Steady-state effective thermal conductivity for bulk silicon at 500K.

It is apparent that the effective thermal conductivity decreases as the domain mesh is refined. Each of these simulations was run for 60 ns. The simulation for the 80 cell case was only run for 30 ns, which was not long enough to reach steady-state. Therefore, the average thermal conductivity would be slightly higher than at steady-state. The average thermal conductivities for the 5, 40, and 80 cell cases were 263 W/mK, 222 W/mK and 188 W/mK, respectively. The experimental value of thermal conducitivity at $500K$ is approximately 80 W/mK [5].

Several researchers have investigated the contribution of phonon polarizations to the heat flux [10, 55]. The results from Mittal and Mazumder [10] suggest that LA phonons contribute most to the heat flux, while Pascual-Gutierrez *et al.* [55] suggest that TAII phonons are the dominant polarization. In the current work, much like that of Pascual-Gutierrez *et al.* [55], the selection rules of three-phonon processes are strictly obeyed. Similarly, it is found that TAII phonons contribute the most to the heat flux. Figure 6.10 shows the heat flux as a function of polarization in each computational cell of the domain at steady-state.

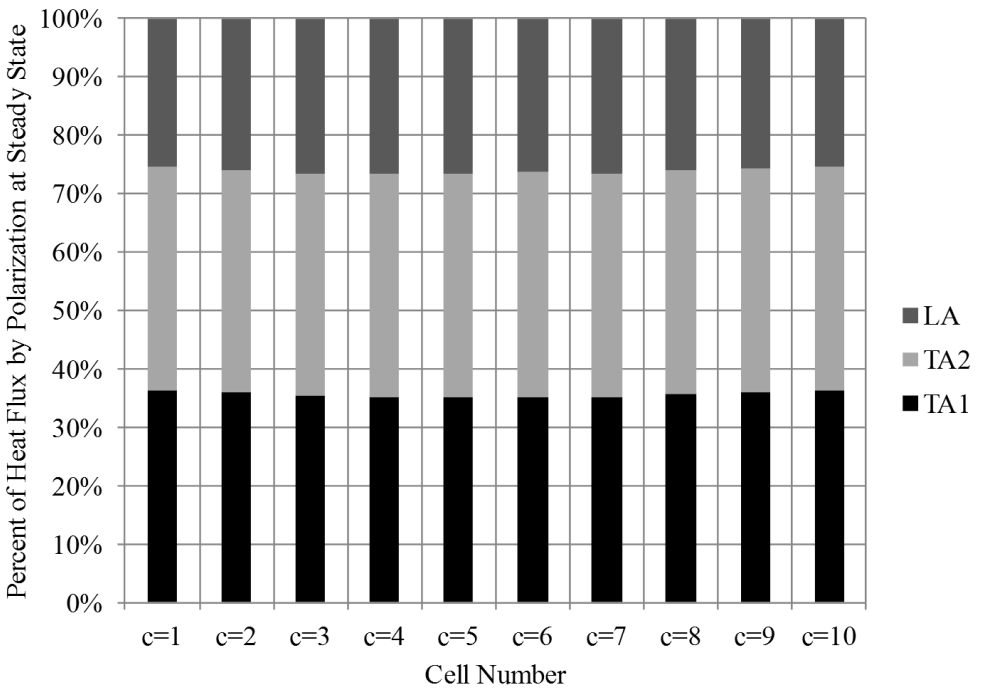

Figure 6.10 The polarization dependent heat flux in bulk silicon at 500 K.

In addition to investigating steady-state thermal transport in the diffuse regime, the transient behavior was also considered using the same domain parameters. Figure 6.11 contains transient temperature results along with an analytical solution, assuming a constant thermal diffusivity of $\alpha_{Si} = 0.37 \times 10^{-4}\ m^2/s$, given as

$$\frac{T(x,t) - T(L,t)}{T(0,t) - T(L,t)} = \left[\text{erfc}\left(\frac{x}{2\sqrt{\alpha t}}\right) - \text{erfc}\left(\frac{2L - x}{2\sqrt{\alpha t}}\right) + \text{erfc}\left(\frac{2L + x}{2\sqrt{\alpha t}}\right) \right] \quad , \qquad (6.1)$$

where t is the time, L is the domain length, x is the position along L, erfc is the complimentary error function and α is the thermal diffusivity [13].

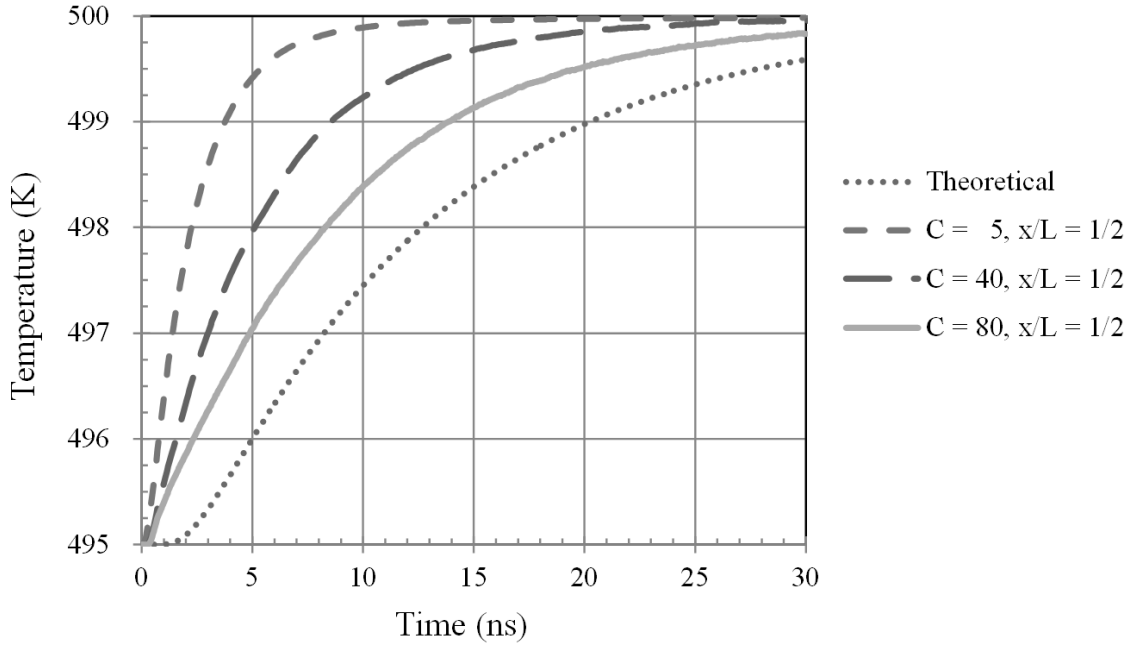

Figure 6.11 Transient temperature response for bulk silicon in the diffuse transport regime.

Similarly, as the domain mesh is refined the transient results approach the analytical solution.

The heat flux at the center of the domain was computed every tenth time step during the transient simulation and is shown in Fig. 6.12.

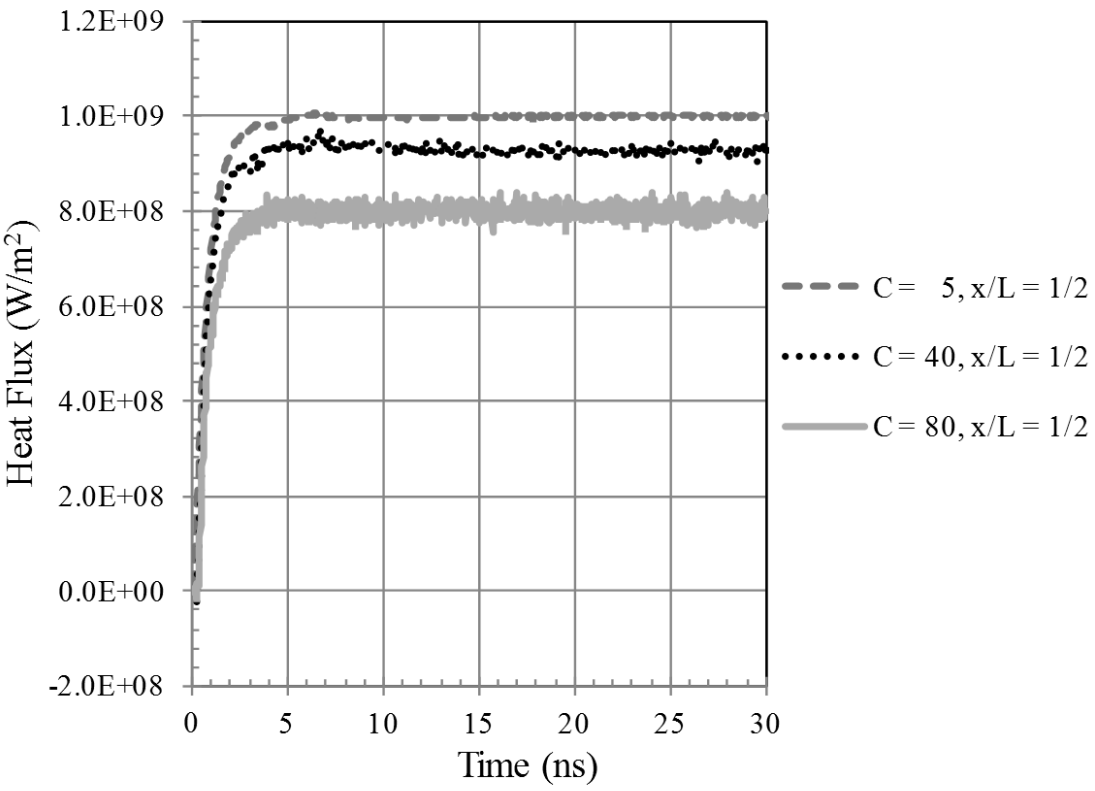

Figure 6.12 Transient flux response for bulk silicon in the diffuse transport regime.

It is interesting to point out that the heat flux has small fluctuations from one time step to the next. As previously described, for any given iteration there are approximately 1.8×10^9 phonons present per geometric cell in the model that both drift and scatter. Due to the large number of Type I and Type II events occurring at equilibrium in a given time step under scattering model A, there will be inherent and physically realistic statistical fluctuation in the flux.

CHAPTER 7

Conclusions

The goal established in Chapter 1 § 1.5 has been achieved. The Statistical Phonon Transport (SPT) model is a full three-dimensional probabilistic model that can simulate thermal transport from nanoscale to bulk semiconductor materials. The SPT solution of the BTE has been shown to employ a fully anisotropic dispersion model. Three-phonon scattering has been demonstrated with a rigorous enforcement of energy and pseudo-momentum. The SPT model does not require the use of pseudo-random number generation, which is typical of other stochastic solutions to the BTE. The SPT model provides a flexible framework that permits incorportation of additional scattering mechanisms and various scattering models. The SPT model may be used to simulate the complex three-dimensional geometric domains necessary for simulating thermal transport in semiconductor devices.

A framework has been presented for a Statistical Phonon Transport model. The SPT model requires no random number generation, unlike Monte Carlo methods, but permits a statistical analysis of phonon transport in crystalline solids. Phonon populations are modeled using pseudo-states, enabling the use of the full number of phonons without reliance on scaling factors. The material properties are modeled

using lattice dynamics, with few underlying assumptions. The SPT model includes a discretization of the BZ and yields a fully anisotropic model for phonon dispersion. The SPT model provides a density of states that is fully consistent with the dispersion curves. Phonon group velocities are calculated directly from the dispersion model used to define the pseudo-states. The group velocities and energy of a pseudo-state are approximated by their centroid values. The pseudo-state drift model allows full phonon populations to move throughout a geometric domain considering several boundary scattering regimes. Pseudo-momentum is rigorously conserved using an assumption of a uniform distribution of phonons across reciprocal lattice space for each pseudo-state. Normal and Umklapp scattering events are modeled in a fully anisotropic manner. Energy is conserved within a specifed tolerance during the creation of an interaction table. Use of too strict of an energy tolerance may cause important interactions to be overlooked, while too lenient of an energy tolerance may cause low frequency phonon populations to dominate the response. A density of interactions histogram has been introduced, which permits understanding of the three-phonon selection criteria in a manner similar to the way in which the density of states histogram permits assessment of the accuracy of a material model. Selection rules for interactions have been discussed only to limited extent in prior work. The current work demonstrates that interaction selection rules and interaction probability rules are essential elements in any statistical treatment of phonon transport, including Monte Carlo methods. During scattering, conservation of energy is enforced in a manner consistent with the use of centroidal frequencies and the approach of modeling phonon populations as opposed to individual phonons.

Validation of the SPT model against analytical test cases has shown that the SPT model is capable of predicting thermal transport in the diffuse, mixed and ballistic regimes. Each result shown was achieved in a single run of the simulation. Averaging of multiple runs is not required. All results shown (temperature, heat flux and conductivity) are self-consistent. The silicon thermal conductivity at 500 K predicted by the SPT model along the [100] direction with a cell size of 25 nm in

the transport direction is twice that of the experimentally reported value of approximately 80 W/mK [5]. It is believed that the inaccuracies in thermal conductivity results can be attributed to the BZ discretization as well as the selection rules for creating the interaction table.

While certain MC investigators [10, 12, 13, 15] have reported a closer approximation to experimentally observed values of thermal conductivity, each of those results have required the use of a user-specified heuristic parameter to achieve the result. Conversely, the SPT scattering model A requires no such heuristic parameter. SPT scattering model B does permit a tuneable relaxation time parameter, which may be appropriate for engineering heat transfer simulations.

Work is currently under way to address the near-boundary ballistic jump phenomena observed in the current work and common to other models. Future work to investigate a more sophisticated scattering algorithm with modest increases in computational time is anticipated. Concurrently, investigation into more robust criteria for including three-phonon events in the scattering table will be performed. The relationship between the near-boundary ballistic jump, the three-phonon scattering interaction table, and non-local equilibrium at the domain edges remains under investigation.

CHAPTER 8

Recommendations for Future Work

A number of extensions to the current work may be investigated to improve the prediction of thermal transport at reduced length scales using the Statistical Phonon Transport (SPT) model. The following future work can be divided into two distinct sections; recommendations for increasing SPT model robustness (1-5) and recommendations for utilizing the SPT model to predict thermal transport in practical applications (6-8).

1. Interaction table study

   The interaction table generated in the preprocessing step of the SPT model is crucial to accurately represent the possible scattering events (three-phonon or isotope) that can and should be permitted to occur. A criterion for selecting events that follow the energy and pseudo-momentum conservation selection rules was given. Also, several measures of the quality of the interaction table were presented in this research. Further work into the selection criteria should be investigated.

2. Improvements to the three-phonon scattering models

The current work presented two models for three-phonon scattering rate algorithms. The first model does not include any relaxation time component. The second model utilizes curve fits of relaxation time data to predict scattering rates for the pseudo-state phonon populations. These average relaxation times do not distinguish between Type I and Type II scattering events or normal and Umklapp processes. It is possible to calculate transition rates for unique three-phonon scattering events using perturbation theory and Fermi's Golden Rule [55]. With the current model if individual transition rates for particular events in the interaction table were known they could easily be incorporated into the SPT model. There is some concern that this would significantly increase computational costs. Therefore, it is recommended that individual scattering rates are computed for individual events and these rates are incorporated into the SPT model's treatment of three-phonon scattering. Once results are investigated for both accuracy of phonon transport and computational cost requirements a decision can be made as to the possibility of implementing a hybrid model that could help reduce computational costs while retaining accuracy in the three-phonon scattering model.

3. Isotope scattering

   The SPT model may be extended to include the treatment of isotope scattering in addition to three-phonon scattering. Incorporation of isotope scattering within the SPT model requires creation of an isotope scattering interaction table and development of an appropriate isotope scattering rate algorithm.

4. Extension of boundary condition library

   An interfacial scattering model is required in order to investigate thermal transport in super-lattice or nano-composite structures. Incorporating geometric elements of multiple materials within a domain having interfacial scattering boundary conditions would increase the applicability of the SPT model to the design of novel devices.

5. Brillouin Zone (BZ) mesh refinement study

   Currently the first octant of the BZ is discretized using a structured mesh of equal volume hexahedral elements. This discretization benefits from 1/8th symmetry of the BZ octants. It is known that the BZ has up to 1/48th symmetry by considering the irreducible wedge. Using an unstructured tetrahedral mesh may provide benefits related to the representation of the BZ, allowing for a finer mesh without increasing computational costs.

6. Thermal transport in complex geometries

   The SPT model accounts for 3-D phonon transport, but in the current work is limited to 1-D thermal transport examples. Extending the SPT model to handle complex 3-D geometries to investigate thermal transport is desired.

7. Metal–oxide–semiconductor field-effect transistor (MOSFET) Simulation

   MOSFET device thermal transport simulations require coupling both a macroscale Fourier conduction model with a model that can accurately predict thermal transport at reduced length scales. Additionally, the transmission coefficients across the interfaces between the two computational domains must be addressed. Incorporating a multigrid method above the SPT model is desired to be able to predict thermal transport in devices.

8. Electron-phonon scattering

   In order to investigate thermal transport in bulk silicon transistors it is necessary to have the appropriate heat generation rates to be assigned to different pseudo-state groups. Attempts to couple full-band MC simulators with phonon transport models have been single-sided. Extending the SPT model to couple with electron MC models to run in parallel is desired.

APPENDIX A

Statistical Phonon Transport Model Input Files

The SPT model requires several input files. In this appendix examples of each of these input files are given.

The SPT model requires information related to the material that is being simulated. This includes not only various constants associated with the material such as the lattice constant, but also information related to the discretization of the BZ. Figure A.1 contains an example of the material property input file.

Silicon 12x12x12;	Descriptive Name of the material being modeled and the pseudo-state mesh being used
0.0000000005431;	Lattice Constant (m)
4.663706415253E-26;	Atomic Mass (kg)
2.75;	Central force constant
0.65;	Angular force constant
1.05459E-34;	Planck's Constant (J s)
1.38062E-23;	Boltzman's Constant (J/K)
19652768;	Number of entries in the interaction table
input/SiliconMesh12ScatterTable.m1;	Path and name of the binary file containing the m1 scattering partners for three phonon scattering
input/SiliconMesh12ScatterTable.m2;	Path and name of the binary file containing the m2 scattering partners for three phonon scattering
input/SiliconMesh12ScatterTable.m3;	Path and name of the binary file containing the m3 scattering partners for three phonon scattering
1.0704E+24;	Number density (1/m^3)
5184;	Number of pseudo states in the first octant
7;	Number of columns

'Freq (1/sec)'	'U_kx (-)	'U_ky (-	'U_kz (-)'	'|k_mag| (1/m)'	'GroupSpeed (m/s)'	'Polarizaton (0-5)'
4.06E+12	0.57735	0.57735	0.57735	834929485.9	4628.331907	0
4.06E+12	0.57735	0.57735	0.57735	834929485.9	4251.217679	1
6.25E+12	0.57735	0.57735	0.57735	834929485.9	6607.529939	2
9.54E+13	0.57735	0.57735	0.57735	834929485.9	469.943141	3
9.55E+13	0.57735	0.57735	0.57735	834929485.9	221.0192692	4
9.55E+13	0.57735	0.57735	0.57735	834929485.9	211.1201165	5
7.91E+12	0.30151	0.30151	0.90453	1598767199	5049.039412	0
8.55E+12	0.30151	0.30151	0.90453	1598767199	5350.412693	1
1.13E+13	0.30151	0.30151	0.90453	1598767199	6887.89099	2
9.49E+13	0.30151	0.30151	0.90453	1598767199	834.1240583	3
9.52E+13	0.30151	0.30151	0.90453	1598767199	485.4550369	4
9.53E+13	0.30151	0.30151	0.90453	1598767199	425.7668853	5
1.30E+13	0.19245	0.19245	0.96225	2504782892	5360.863579	0
1.36E+13	0.19245	0.19245	0.96225	2504782892	5344.652477	1
1.69E+13	0.19245	0.19245	0.96225	2504782892	6715.897447	2
9.41E+13	0.19245	0.19245	0.96225	2504782892	1217.521342	3
9.46E+13	0.19245	0.19245	0.96225	2504782892	767.5058818	4
9.47E+13	0.19245	0.19245	0.96225	2504782892	736.0765255	5
1.82E+13	0.14003	0.14003	0.9802	3442503595	5328.606503	0
1.86E+13	0.14003	0.14003	0.9802	3442503595	5225.16761	1
2.27E+13	0.14003	0.14003	0.9802	3442503595	6523.497696	2
9.29E+13	0.14003	0.14003	0.9802	3442503595	1602.291473	3
9.38E+13	0.14003	0.14003	0.9802	3442503595	1037.057577	4
9.39E+13	0.14003	0.14003	0.9802	3442503595	1030.487273	5
				⋮		

Figure A.1 An example of the material property input file used in the SPT model.

The three-phonon interaction table is related to the discretization of the BZ and is a required input for the SPT model. Figure A.2 contains an example of the interaction table utilized during the three-phonon scattering phase of the SPT model.

m1	m2	m3
0	0	582
0	3	585
0	3	586
0	3	587
0	4	586
0	4	587
0	5	586
0	5	587
1	1	583
1	1	584
1	2	585
1	2	586
1	3	587
1	4	586
2	2	587
2	3	586
2	3	587
	⋮	
822	46627	42195
823	46626	42195
823	46632	42009
823	46638	43209
823	46644	44469
823	46651	44229
823	46669	41703
824	46692	41903
824	46698	41699
824	46704	42634
824	46704	42635
824	46710	40858
824	46710	40859
824	46718	37054
824	46718	37055
824	46724	36047
825	46782	6617
825	46788	36677
825	46789	36677
825	46794	30376
825	46795	30377
	⋮	

Figure A.2 An example of the three-phonon scattering interaction table used in the SPT model.

In addition to material property information, the SPT model requires information related to the geometric domain that is to be modeled. Typically, for a given material, by changing on this input file many simulations can be performed. The following figure is an example of the geometric domain input file.

output/steady_state_300K;	Path and root name of the output files to be generated by the code
input/SiliconMesh12FirstOctantStates.csv;	Path and name of the file containing the pseudo-state information for the first octant of the BZ
0.001;	Time step increment (nsec)
20;	Number of geometric cells in the x direction, the direction of the one-d model
4000;	Length of the domain in the x direction (nm)
100;	Length of the domain in the y direction (nm)
100;	Length of the domain in the z direction (nm)
305;	Temperature at the left boundary of the domain (K)
295;	Temperature at the right boundary of the domain (K)
1;	Lateral (xy and xz planes) boundary scattering specularity

Figure A.3 An example of the geometric domain input file used in the SPT model.

References

[1] G. Chen, *Nanoscale Energy Transport and Conversion: A Parallel Treatment of Electrons, Molecules, Phonons, and Photons*. Oxford University Press, 2005.

[2] C. L. Tien, A. Majumdar, and F. M. Gerner, *Microscale Energy Transport*. Washington D.C.: Taylor & Francis, 1998.

[3] J. M. Ziman, *Electrons and Phonons*. London: Oxford University Press, 1960.

[4] J. Callaway, "Model for lattice thermal conductivity at low temperatures," *Physical Review*, vol. 113, no. 4, pp. 1046–1051, 1959.

[5] M. G. Holland, "Analysis of lattice thermal conductivity," *Physical Review*, vol. 132, no. 6, pp. 2461–2471, 1963.

[6] M. G. Holland, "Phonon scattering in semiconductors from thermal conductivity studies," *Physical Review*, vol. 134, no. 2A, pp. A471–A480, 1964.

[7] J. D. Chung, A. J. H. McGaughey, and M. Kaviany, "Role of phonon dispersion in lattice thermal conductivity modeling," *Journal of Heat Transfer*, vol. 126, pp. 376–380, 2004.

[8] K. C. Sood and M. K. Roy, "Longitudinal phonons and high-temperature heat conduction in germanium," *Journal of Physics: Condensed Matter*, vol. 5, pp. 301–312, 1993.

[9] T. Wang and J. Y. Murthy, "Solution of the phonon boltzmann transport equation employing rigorous implementation of phonon conservation rules," in *Proceedings of the ASME International Mechanical Engineering Congress and Exposition*, Chicago, Illinois, USA, November 2006.

[10] A. Mittal and S. Mazumder, "Monte carlo study of phonon heat conduction in silicon thin films including contributions of optical phonons," *Journal of Heat Transfer*, vol. 132, no. 5, p. 052402, 2010.

[11] S. V. J. Narumanchi, J. Y. Murthy, and C. H. Amon, "Submicron heat transport model in silicon accounting for phonon dispersion and polarization," *Journal of Heat Transfer*, vol. 126, pp. 946–955, December 2004.

[12] S. Mazumder and A. Majumdar, "Monte carlo study of phonon transport in solid thin films including dispersion and polarization," *Journal of Heat Transfer*, vol. 123, pp. 749–759, 2001.

[13] D. Lacroix, K. Joulain, and D. Lemonnier, "Monte carlo transient phonon transport in silicon and germanium at nanoscales," *Physical Review B*, vol. 72, no. 064305, 2005.

[14] Y. Chen, D. Li, J. R. Lukes, and A. Majumdar, "Monte carlo simulation of silicon nanowire thermal conductivity," *Journal of Heat Transfer*, vol. 127, pp. 1129–1136, 2005.

[15] J. Randrianalisoa and D. Baillis, "Monte carlo simulation of steady-state microscale phonon heat transport," *Journal of Heat Transfer*, vol. 130, July 2008.

[16] D. G. Cahill, W. K. Ford, G. D. Mahan, A. Majumdar, H. J. Maris, R. Merlin, and S. R. Phillpot, "Nanoscale thermal transport," *Journal of Applied Physics*, vol. 93, no. 2, 2003.

[17] J. Y. Murthy, S. V. J. Narumanchi, J. A. Pascual-Gutierrez, T. Wang, C. Ni, and S. R. Mathur, "Review of multiscale simulation in submicron heat transfer," *Int. Journal for Multiscale Computational Engineering*, vol. 3, no. 1, pp. 5–32, 2005.

[18] G. Chen, D. Borca-Tasciuc, and R. G. Yang, "Nanoscale heat transfer," in *Encyclopedia of Nanoscience and Nanotechnology.* American Scientific Publishers, 2004, vol. 7, pp. 429–459.

[19] S. G. Volz and G. Chen, "Molecular dynamics simulation of thermal conductivity of silicon nanowires," *Applied Physics Letters*, vol. 75, pp. 2056–2058, 1999.

[20] Y. Chen, D. Li, J. Yang, Y. Wu, J. R. Lukes, and A. Majumdar, "Molecular dynamics study of the lattice thermal conductivity of Kr/Ar superlattice nanowires," *Physica B*, vol. 349, pp. 270–280, 2004.

[21] X. Feng, Z. Li, and Z. Guo, "Molecular dynamics simulation of thermal conductivity of nanoscale thin silicon films," *Microscale thermophysical engineering*, vol. 7, pp. 153–161, 2003.

[22] Z. Zhong, X. Wang, and J. Xu, "Equilibrium molecular dynamics study of phonon thermal transport in nanomaterials," *Numerical Heat Transfer Part B: Fundamentals*, vol. 46, no. 5, pp. 429–446, 2004.

[23] K. Imamura, Y. Tanaka, N. Nishiguchi, S. Tamura, and H. J. Maris, "Lattice thermal conductivity in superlattices: Molecular dynamics calculations with a heat reservoir method," *Journal of Physics: Condensed Matter*, vol. 15, pp. 8679–8690, 2003.

[24] X. Huang and X. Huai, "Molecular dynamics simulation of thermal conductivity in si-ge nanocomposites," *Chinese Phyics Letters*, vol. 25, pp. 2973–2976, 2008.

[25] P. J. Hegedus and A. R. Abramson, "A molecular dynamics study of interfacial thermal transport in heterogeneous systems," *International Journal of Heat and Mass Transfer*, vol. 49, pp. 4921–4931, 2006.

[26] R. J. Stevens, "Thermal transport at room temperature solid-solid interfaces," Ph.D. dissertation, University of Virginia, 2005.

[27] P. Heino, "Dispersion and thermal resistivity in silicon nanofilms by molecular dynamics," *The European Physical Journal B*, vol. 60, pp. 171–179, 2007.

[28] A. S. Henry and G. Chen, "Spectral phonon transport properties of silicon based on molecular dynamics simulations and lattice dynamics," *Journal of Computational and Theoretical Nanoscience*, vol. 5, pp. –12, 2008.

[29] R. Eckhardt, "Stan Ulam, John von Neumann, and the monte carlo method," in *Los Alamos Science Special Issue*, 1987, pp. 131–143.

[30] H. Niederreiter, *Random Number Generation and Quasi-Monte Carlo Methods*. Philadelphia, Pennsylvania: Society For Industrial And Applied Mathematics, 1992.

[31] M. F. Modest, *Radiative Heat Transfer*, 2nd ed. Burlington, MA: Academic Press, 2003.

[32] C. Jacoboni and L. Reggiani, "The monte carlo method for the solution of charge transport in semiconductors with applications to covalent materials," *Reviews of Modern Physics*, vol. 55, no. 3, pp. 645–705, July 1983.

[33] R. B.Peterson, "Direct simulation of phonon-mediated heat transfer in a debye crystal," *Journal of Heat Transfer*, vol. 116, pp. 815–822, 1994.

[34] D. Song, "Phonon heat conduction in nano and micro-porous thin films," Ph.D. dissertation, University of California - Los Angeles, 2003.

[35] T. Klistner, J. E. VanCleve, E. F. Henry, and R. O. Pohl, "Phonon radiative heat transfer and surface scattering," *Physical Review B*, vol. 38, no. 11, pp. 7576–7594, 1988.

[36] R. Yang, "Nanoscale heat conduction with applications in nanoelectronics and thermoelectrics," Ph.D. dissertation, Massachusetts Institute of Technology, 2006.

[37] M. Jeng, R. Yang, and G. Chen, "Monte carlo simulation of thermoelectric properties in nanocomposites," in *Proceedings of the 24th International Conference on Thermoelectrics (IEEE)*, 2005.

[38] J. Randrianalisoa and D.Baillis, "Monte carlo simulation of cross-plane thermal conductivity of nanostructured porous silicon films," *Journal of Applied Physics*, vol. 103, 2008.

[39] O. Essner, P. Dollfus, S. Galdin-Retailleau, and J. Saint-Martin, "Improved monte carlo algorithm of phonon transport in semiconductor nanodevices," *Journal of Physics: Conference Series*, vol. 92, 2007.

[40] Ferrotec company website. [Online]. Available: http://www.ferrotec.com/technology/thermoelectric

[41] G. Slack, "New materials and performance limits for thermoelectric cooling," in *CRC Handbook of Thermoelectrics*. CRC Press, 1995, pp. 407–440.

[42] J. A. Pascual-Gutierrez, "On the theory of phonons: A journey from their origins to the intricate mechanisms of their transport," Ph.D. dissertation, Purdue University, 2010.

[43] R. Venkatasubramanian, E. Siivola, T. Colpitts, and B. O'Quinn, "Thin-film thermoelectric devices with high room-temperature figures of merit," *Nature*, vol. 413, pp. 597–602, 2001.

[44] T. C. Harman, P. J. Taylor, M. P. Walsh, and B. E. LaForge, "Quantum dot superlattice thermoelectric materials and devices," *Science*, vol. 297, pp. 2229–2232, 2002.

[45] X. B. Zhao, X. H. Ji, Y. H. Zhang, T. J. Zhu, J. P. Tu, and X. B. Zhang, "Bismuth telluride nanotubes and the effects on the thermoelectric properties of nanotube-containing nanocomposites," *Applied Physics Letters*, vol. 86, no. 062111, 2005.

[46] A. I. Boukai, Y. Bunimovich, J. Tahir-Kheli, J. Yu, W. A. G. III, and J. R. Heath, "Silicon nanowires as effiecient thermoelectric materials," *Nature*, vol. 451, pp. 168–171, 2008.

[47] T. Harris, H. Lee, D. Z. Wang, J. Y. Huang, Z. F. Ren, B. Klotz, R. Dowding, M. S. Dresselhaus, and G. Chen, "Thermal conductivity reduction of SiGe nanocomposites," in *Proceedings of the Materials Research Society Symposium*, vol. 793, 2004.

[48] A. K. Ghatak and L. S. Kothari, *An Introduction to Lattice Dynamics*. Addison-Wesley Publishing Company, 1972.

[49] J. S. Blakemore, *Solid State Physics*. Cambridge: Cambridge University Press, 1985.

[50] P. Y. Yu and M. Cardona, *Fundamentals of Semiconductors: Physics and Materials Properties*. Springer, 2001.

[51] C. Kittel, *Introduction to Solid State Physics*, 6th ed. New Jersey: John Wiley & Sons Inc., 1986.

[52] W. Weber, "Adiabatic bond charge model for the phonons in diamond, Si, Ge, and alpha -Sn," *Physical Review B*, vol. 15, pp. 4789–4803, 1977.

[53] G. P. Srivastava, *The Physics of Phonons*. CRC Press, 1990.

[54] G. Chen, "Phonon heat conduction in nanostructures," *International Journal of Thermal Sciences*, vol. 39, no. 4, pp. 471–480, April 2000.

[55] J. A. Pascual-Gutierrez, J. Y. Murthy, and R. Viskanta, "Thermal conductivity and phonon transport properties of silicon using perturbation theory and the environment-dependent interatomic potential," *Journal of Applied Physics*, vol. 106, p. 063532, 2009.

[56] H. Hamzeh and F. Aniel, "Monte carlo study of phonon dynamics in III-V compounds," *Journal of Applied Physics*, no. 109, p. 063511, 2011.

[57] P. Aynajian, *Electron-phonon interaction in conventional and unconventional superconductors*. Springer-Verlag, 2010.

[58] Y. J. Han and P. G. Klemens, "Anharmonic thermal resistivity of dielectric crystals at low temperatures," *Physical Review B*, vol. 48, no. 9, pp. 6033–6042, 1993.

[59] T. W. Brown III and E. Hensel, "Statistical phonon transport model of thermal transport in silicon," in *Proceedings of the Materials Research Society Symposium*, Boston, MA, USA, December 2009.